

Superconductivity and antiferromagnetism in the two-dimensional Hubbard model

Thèse

présentée à la Faculté des Sciences de l'Université de Fribourg (Suisse)
pour l'obtention du grade de

DOCTOR RERUM NATURALIUM

David Eichenberger

de

Beinwil am See (AG)

Thèse N° 1606
Imprimerie de l'université (UniPrint)
2008

Acceptée par la Faculté des Sciences de l'Université de Fribourg (Suisse) sur la proposition de:

- Prof. Dionys Baeriswyl, Université de Fribourg, Suisse (Directeur de thèse).
- Prof. Dmitri Ivanov, EPFL, Switzerland (Expert).
- Prof. Reinhard M. Noack, Philipps-Universität Marburg, Germany (Expert).
- Prof. Antoine Weis, Université de Fribourg, Suisse (Président du jury).

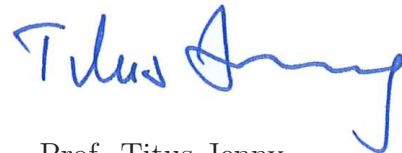
Fribourg, le 27 mai 2008,

Le Directeur de thèse:



Prof. Dionys Baeriswyl

Le Doyen:



Prof. Titus Jenny

Acknowledgements

I am deeply grateful to Dionys Baeriswyl, my PhD supervisor, for his valuable guidance and kind support throughout my work.

I have special thanks for all present and past members of the theoretical institut for sharing with me this nice period of my life. Vladimir and Bruce, thank you for your advices and all our motivating discussions. Bruno and Peter, it was simply wonderful to share the office with you. Xavier, I will miss our coffee break discussions.

I would like to thank my thesis examiners Dmitri Ivanov and Reinhard Noack.

Un grand merci à mes parents André et Michèle qui m'ont encouragé tout au long de mes études, ainsi qu'à toute ma famille.

Finalement, toutes mes pensées vont à ma femme, Caroline, que je remercie de tout mon coeur de m'avoir soutenu depuis le début, et à mon fils Noah, qui en me laissant dormir la nuit, m'a permis d'être au mieux de mes possibilités.

Abstract

Despite its apparent simplicity and even if it has been studied intensively in various contexts, the two-dimensional Hubbard model is not yet completely understood. In particular when it describes a system with an intermediate interaction, out of range for perturbative methods, its ground state is still not well known. The discovery in 1986 of a superconducting phase in the copper oxides (cuprates), which appears at rather high temperature, has further enhanced the interest for this model, as it may describe the amazing properties of these layered materials. Indeed, when the electronic density corresponds to a half-filled band, the Hubbard model is known to nicely account for the antiferromagnetic phase obtained experimentally for the cuprates and it is possible, as first proposed by P. W. Anderson, that it describes equally well the superconducting phase observed below a critical temperature, when the electronic density is moderately reduced by modifying the compound composition (doping). In this case, the superconductivity originates from purely electronic interactions, contrary to conventional superconductivity where the interaction between electrons and lattice vibrations (phonons) is involved. Unfortunately, very few stringent results are available in order to support this statement and this question is still largely debated. In this thesis, the variational method is used in order to scrutinize the possibility of a superconducting ground state for the repulsive Hubbard model. Although its reliability is based on the adequate choice of the variational wave function, this method is especially suited for treating intermediate interactions, which is the appropriate regime of the cuprates. The optimization of a refined wave function allows us to obtain a variational ground state which is much closer to the exact ground state than those obtained so far using less elaborate wave functions. Actually, the exact study of small systems indicates that the error of our calculation is too small to allow for a qualitatively different behavior. Our results show that an antiferromagnetic phase is dominant at half-filling, while a superconducting phase with a d -wave symmetry of the order parameter emerges at moderate doping. The key features of the copper oxides are therefore found in the variational ground state of the repulsive Hubbard model. Some amazing similarities are also observed at the quantitative level when the properties of this ground state are compared to the experimental data obtained for the cuprates.

Résumé

En dépit de son apparente simplicité et bien qu'il ait déjà été intensivement étudié dans des contextes très variés, le modèle de Hubbard bi-dimensionnel est encore très loin d'avoir livré tous ses mystères. En particulier lorsqu'il décrit une interaction moyenne à fortement répulsive, c'est-à-dire un régime mal adapté aux méthodes perturbatives, son état fondamental est encore méconnu. La découverte en 1986 d'une phase supraconductrice chez les oxydes de cuivre (cuprates), apparaissant à relativement haute température, a encore avivé l'intérêt pour ce modèle puisqu'il pourrait décrire les propriétés étonnantes de ces matériaux à structures planaires. Lorsque la densité électronique correspond à une bande de valence demi-remplie, le modèle de Hubbard est en effet connu pour rendre parfaitement compte de la phase antiferromagnétique obtenue expérimentalement chez les cuprates et il est probable qu'il en soit de même pour la phase supraconductrice observée au-dessous d'une température critique, lorsque la densité électronique est modérément réduite en modifiant la composition du matériau (dopage). Si tel est le cas, cela signifie que seules les interactions électroniques sont à l'origine de la supraconductivité, contrairement aux supraconducteurs conventionnels où l'interaction entre les électrons et les vibrations du réseau (phonons) est impliquée. Malheureusement il existe pour l'heure peu de résultats indiscutables venant étayer cette hypothèse et la question est encore largement débattue. Dans cette thèse, la méthode variationnelle est mise à profit pour tenter d'apporter une réponse claire concernant la possibilité d'un état fondamental supraconducteur pour le modèle de Hubbard répulsif. Bien que la fiabilité de ses résultats soit conditionnée par le choix d'une fonction variationnelle adéquate, cette méthode est tout spécialement adaptée au régime approprié pour les cuprates, c'est-à-dire à une interaction intermédiaire. L'optimisation d'une fonction variationnelle élaborée permet d'approcher de très près l'état fondamental exact, ce qui n'était pas le cas des fonctions variationnelles connues jusqu'ici. En fait, la considération de petits systèmes rend accessible une solution exacte, qui indique que l'erreur commise dans notre calcul est trop faible pour influencer qualitativement nos résultats. Ceux-ci montrent qu'une phase antiferromagnétique est favorable au demi-remplissage et qu'une phase supraconductrice émerge lorsque la densité électronique diminue, avec un paramètre d'ordre possédant une symétrie onde- d . Toutes les caractéristiques principales propres aux oxydes de cuivre sont donc retrouvées pour l'état fondamental variationnel du modèle de Hubbard répulsif. Des similitudes remarquables sont aussi observées au niveau quantitatif lorsque les propriétés de cet état fondamental sont comparées aux données expérimentales obtenues pour les cuprates.

Contents

1	Introduction	9
1.1	High- T_c cuprates	9
1.1.1	Generic phase diagram	12
1.2	The single-band Hubbard model	13
2	BCS approximation for nearest-neighbor attraction	17
2.1	Size effects	21
2.2	Phase diagram	23
3	Superconductivity from purely repulsive interaction	25
3.1	Kohn-Luttinger mechanism	25
3.2	Weak coupling: Renormalization Group	27
3.3	Large U limit: the t-J model	33
3.3.1	The variational method	34
3.3.2	Variational Monte Carlo (VMC)	37
3.3.3	Results	38
3.4	Intermediate value of the repulsion U	41
3.4.1	Quantum Monte Carlo	41
3.4.2	Cluster Dynamical Mean Field Theory	45
3.4.3	Variational Monte Carlo: The Gutzwiller ansatz	51
3.4.4	Improving the Gutzwiller ansatz	55
4	A refined variational wave function	60
4.1	The $1/r$ Hubbard chain	60
4.2	Small clusters	63
4.3	Antiferromagnetism	63
4.3.1	Monte Carlo simulation for $ \Psi_{GB}^{AF}\rangle$	65
4.3.2	Half-filled case	68
4.4	The superconducting instability	69
4.4.1	Monte Carlo simulation for $ \Psi_{GB}^{BCS}\rangle$	70
4.4.2	Size effects	72
4.4.3	The simple Hubbard model	76

4.4.4	Next-nearest-neighbor hopping	81
5	Relevance for high-T_c cuprates	86
5.1	Gap parameter	87
5.2	Condensation energy	88
5.3	Kinetic energy	89
5.4	Spin-spin correlations	92
6	Summary and conclusions	94
	Bibliography	97
A	Three-band Hamiltonian	100
B	The BCS ground state	102
C	Kadanoff-Wilson-Polchinski renormalization group	105
D	Canonical ensemble	109
D.1	One-body operators	110
D.2	Two-body operators	112
E	Grand canonical ensemble	113
E.1	One-body operators	115
E.2	Two-body operators	115
F	Integration of the fermionic degrees of freedom	118
G	Calculation of the one-body operators	120

Chapter 1

Introduction

1.1 High- T_c cuprates

The emergence of a superconducting phase in various Copper oxides (“cuprates”) when the hole concentration is increased has first been revealed by J. G. Bednorz and K. A. Müller in 1986 [1]. Due to the rather high critical temperature of the transition, these compounds have received attention of many researchers, both theorists and experimentalists. The insulating nature of the parent compound (when the system is not doped with holes) has quickly led to the claim that we face an unconventional mechanism for superconductivity. More than twenty years later, despite intensive research, no clear understanding of this mechanism has been reached. The aim of this thesis is to find out whether a simple model of strongly correlated electrons is able to produce a plausible mechanism for superconductivity in the high- T_c cuprates.

This category of materials includes a wide variety of compounds, sharing a similar particularity in their atomic structure: they all contain superconducting CuO_2 planes separated by insulating layers. The atomic structures of two different compounds are given in Figure 1.1. Experimentally, these materials display properties that are more or less isotropic in the plane (the a-b directions), but markedly different perpendicular to the planes (the c-direction). Therefore they are often referred to as “layered cuprates”.

It is now commonly accepted that the electronic and magnetic properties of the layered cuprates are determined by the electronic structure of the CuO_2 plane (Figure 1.2). The stoichiometry of the parent compound, such as La_2CuO_4 , indicates that the copper ion is in the valency Cu^{2+} , corresponding to a $3d^9$ configuration. It means that one electron is missing to fill the five d-orbitals. The levels of these d-orbitals are in principle degenerate, but in the cuprates the crystal field lifts the degeneracy. Therefore the orbital with the highest energy, the $d_{x^2-y^2}$ orbital, is only half-filled. The oxygen ion has a valency O^{2-} corresponding to filled p-orbitals. The p_z orbital and one of the in-plane orbitals (p_x or p_y depending on the location (see Figure 1.2)) are orthogonal to the $d_{x^2-y^2}$ orbital of the copper ion (the transfer integral is zero) and can be neglected. Therefore, the CuO_2 plane has three orbitals per unit cell and it is described by a model with three bands. A simple tight-binding model for

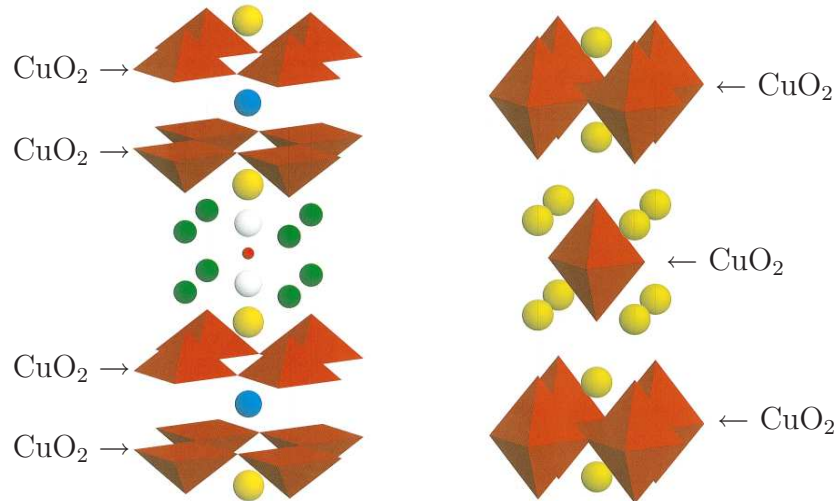


Figure 1.1: Atomic structures of $\text{Pb}_2\text{Sr}_2\text{YCu}_3\text{O}_8$ (left) and of La_2CuO_4 (right). The copper ions are surrounded by oxygen ions, forming either the red pyramids or the red octahedra. The CuO_2 planes are indicated.

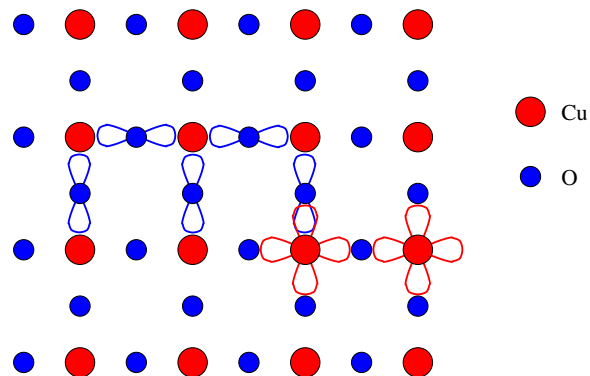


Figure 1.2: Atomic structure of a CuO_2 plane. This plane is the shared particularity of all high- T_c compounds. On each oxygen site, one p-orbital (p_x or p_y , in blue) has a finite transfer integral with the $d_{x^2-y^2}$ orbital of the copper site, in red.

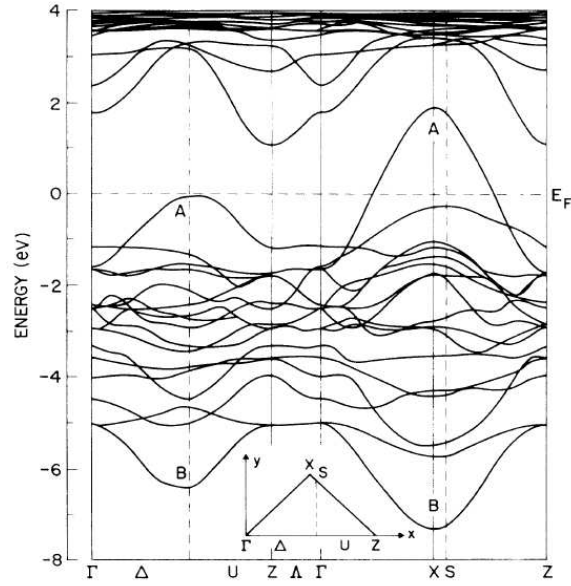


Figure 1.3: LDA Band structure of La_2CuO_4 in the body-centered-tetragonal phase, along the high-symmetry lines as indicated by the inset. The Λ segment corresponds to out-of-plane dispersion. From [2].

the square lattice with orbitals $d_{x^2-y^2}$, p_x and p_y and nearest-neighbor hopping t_{pd} is able to provide an accurate description of the important energy bands of a Local Density Approximation (LDA) for La_2CuO_4 [2]. The band structure obtained in this calculation is plotted in Figure 1.3.

The antibonding (A) and bonding (B) bands are hybridized Cu-O bands resulting from the overlap between p and d orbitals. The two-dimensional nature of these two bands, which are quite well reproduced by the tight-binding model, can be observed on the Λ segment of Figure 1.3, where almost no dispersion is found along the direction perpendicular to the x-y plane. The antibonding band is only half-filled and a metallic behavior is expected for the parent compound. However, it turns out that the cuprates are good insulators at half-filling and we have to conclude that correlations play an important role. As explained in Appendix A, the strong electronic correlations open a gap in the density of state and the consequence is that, according to the classification of Allen-Savatzky-Zaanen [3], the cuprates are charge-transfer insulators. In the hole-picture, the electronic configuration implies one hole per unit cell. The lowest available states for this hole are separated from the occupied states by a rather large charge-transfer gap $\Delta_{pd} = \epsilon_p - \epsilon_d$ (see Figure A.1) and therefore these states are unoccupied. It means that the holes are localized on the d-orbitals where they induce a local moment. At low energy only spin excitations are possible and as for the Mott insulators, a kinetic exchange process is expected to lead to antiferromagnetic

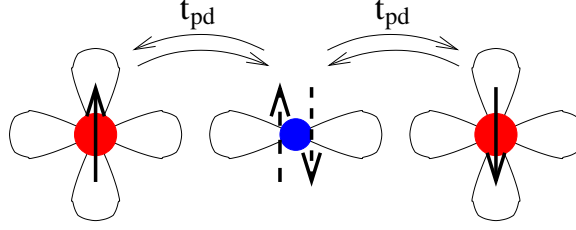


Figure 1.4: Superexchange process leading to antiferromagnetic ordering at half-filling. Due to the large charge-transfer gap the holes reside essentially on the copper ions. However, the virtual hopping to the oxygen ion allows the system to gain energy. Due to the Pauli principle, the moments induced by the holes on two neighboring copper atoms have to be opposite in order that both holes can meet on the oxygen site.

ordering of the moments (see Figure 1.4). For $\Delta_{pd} \rightarrow \infty$ the three-band model can be replaced by an effective one-band Heisenberg model with an exchange $J_{eff} \sim t_{pd}^4 / \Delta_{pd}^3$ [4], which describes quite well the antiferromagnetic ordering. Neutron scattering experiments show that indeed, an antiferromagnetic phase is found for the cuprates at half-filling (see Figure 1.5) [5],[6].

1.1.1 Generic phase diagram

The most striking properties of the cuprates are observed when the hole concentration of the CuO_2 plane is increased in these materials. In this case, one says that the cuprate is doped. For some cuprates the oxygen content is not stoichiometric and this means that it is possible to vary the number of holes in the plane by changing the oxygen concentration. In $\text{YBa}_2\text{Cu}_3\text{O}_{6+\delta}$ for instance, oxygen ions O^{2-} can be added away from the CuO_2 planes. Then charge neutrality implies that some electrons are removed from the plane. Another way to dope a cuprate is to partially substitute one element of the chemical formula by another one with a different valency. For the parent compound La_2CuO_4 given in Figure 1.1, the replacement of La^{2+} by Sr^{3+} adds one hole to the plane. Therefore the compound $\text{La}_{2-x}\text{Sr}_x\text{CuO}_4$ contains a concentration x of doped holes. Due to the large electronic repulsion in the d-orbitals, the additional holes reside on the p-orbitals of the oxygen ions (see Appendix A). The properties of the cuprates depend strongly on the doping parameter x , but this dependence is quite similar for all compounds and a generic phase diagram can be established (Figure 1.5). As already mentioned, the parent compound is an antiferromagnetic insulator. The antiferromagnetic order is quickly destroyed when holes are added to the system. The Néel temperature T_N vanishes at about $x = 0.04$. A superconducting dome appears between $x = 0.05$ and $x = 0.25$ with a maximum critical temperature T_c at $x = 0.15$. The temperature T^* indicates approximately the crossover between a pseudogap phase which behaves as a bad metal and a non-Fermi

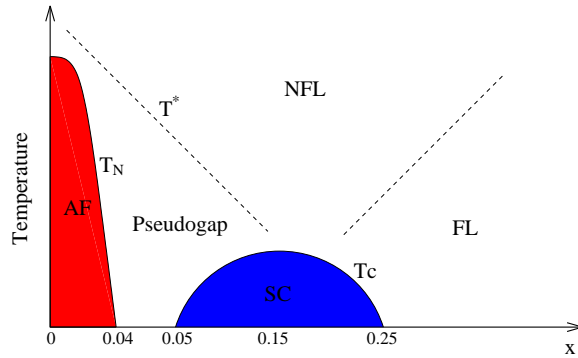


Figure 1.5: Generic phase diagram of the high- T_c cuprates.

liquid region (NFL) characterized by an unusual metallic behavior. When the hole concentration exceeds $x = 0.25$, a normal Fermi liquid phase (FL) is recovered.

The order parameter of the superconducting instability has a d-wave symmetry, as known from angle resolved photoemission spectroscopy (ARPES) [7],[8]. This technique provides a measure of the single-particle spectral function $A(\vec{k}, \omega)$. In the normal state, a broad peak due to Fermi liquid quasiparticles is observed in the energy distribution curves for various momenta (see left-hand side of Figure 1.6(a),(b) and (c)). Then the Fermi surface is located at the momentum where this peak crosses the zero binding energy line and disappears. Below the critical temperature, a narrow peak due to the superconducting quasiparticles appears at the Fermi surface. This peak is pushed to higher binding energy by the superconducting gap. The data on the right-hand side of Figure 1.6 show that this gap is not isotropic, but depends rather strongly on the momentum. By following the contour of the normal state Fermi surface, the superconducting gap is found to fit quite well the d-wave symmetry. Moreover, a small anisotropic pseudogap is already observed in the normal state for this compound (panel (a)).

1.2 The single-band Hubbard model

In Figure 1.6 left, the energy distribution curves (a)-(c) indicates clearly that only one band is present at the Fermi surface. This suggests that the electronic properties of the cuprates can be described properly by an effective one band model on a two-dimensional lattice. A simple model with one band including the strong electronic correlations and describing perfectly well the antiferromagnetic phase at half-filling is the one-band repulsive Hubbard model on a square lattice:

$$\hat{H} = t\hat{T} + U\hat{D} \quad (1.1)$$

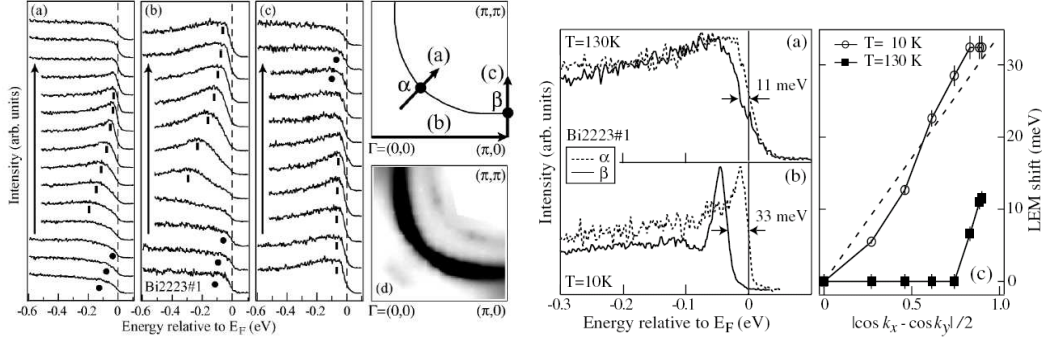


Figure 1.6: ARPES data for a $\text{Bi}_2\text{Sr}_2\text{Ca}_2\text{Cu}_3\text{O}_{10+\delta}$ compound near optimal doping ($T_c = 108$ K). Left-hand side: Measurement of the normal state Fermi surface ($T = 130$ K). The panel (a)-(c) show the measured intensity along the high-symmetry lines, as indicated in the sketched Brillouin zone. The panel (d) gives an intensity map of the ARPES spectra integrated within a narrow energy window at the Fermi energy. Right-hand side: (a)-(b): Measurement in the nodal (α) or antinodal (β) region (see the sketched Brillouin zone of the left-hand side) (a): The normal state pseudogap defined by the energy position of the leading-edge-midpoint (LEM). (b): The superconducting gap below the critical temperature ($T = 10$ K). (c): Position of the LEM along the normal state Fermi surface in the normal or superconducting state and comparison with the functional form of a d -wave gap (dashed line). From [7].

with

$$\hat{T} = - \sum_{\langle i,j \rangle, \sigma} (c_{i\sigma}^\dagger c_{j\sigma} + c_{j\sigma}^\dagger c_{i\sigma}) \quad \text{and} \quad \hat{D} = \sum_i n_{i\uparrow} n_{i\downarrow}. \quad (1.2)$$

Here $c_{i\sigma}^\dagger$ creates an electron at site i with spin σ , the summation is restricted to nearest-neighbor sites and $n_{i\sigma} = c_{i\sigma}^\dagger c_{i\sigma}$. In Eq. (1.1), the first term describes the energy gain for the delocalized electrons, whereas the second term accounts for the energy cost due to double occupation of sites (see Figure 1.7). In the context of the cuprates, this one band model should of course be understood as an effective model replacing the true microscopic model, which is the three-band Hubbard model. This effective model can be obtained by considering that an additional hole can resonate between the four oxygen sites surrounding a copper site, in order to gain energy by delocalization [9]. In the hole picture, the spin of this additional hole and the spin on the copper site form a spin singlet, called “Zhang-Rice singlet”, which can hop from one copper site to another. For $\Delta_{pd} \rightarrow \infty$, this process is equivalent to the hopping of a single hole between two copper sites, which is allowed only if it does not create a doubly occupied site. Actually, this hopping corresponds to a two-step process in term of the transfer parameter t_{pd} between p and d orbitals, with an effective parameter $t \sim \frac{t_{pd}^2}{\epsilon_d - \epsilon_p}$ [9]. Therefore the whole three-band model is reduced to a one-band t-J

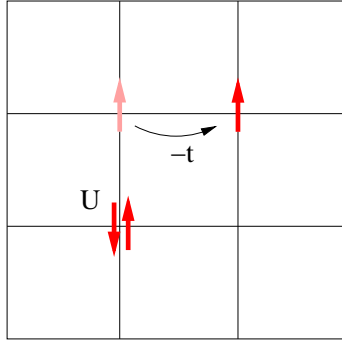


Figure 1.7: Effective one-band Hubbard model for the description of the cuprates. The hopping parameter t corresponds to delocalization of the electrons between nearest-neighbor sites on the $L \times L$ square lattice, whereas the Coulomb parameter U describes the energy cost for the double occupation of one site.

model when the spin interaction (Heisenberg term) is taken into account. But the t-J model is just the infinite U limit of the Hamiltonian (1.1) and therefore the one-band Hubbard model with effective parameters:

$$t \sim \frac{t_{pd}^2}{\epsilon_d - \epsilon_p} \quad \text{and} \quad U = \Delta_{pd} = \epsilon_d - \epsilon_p \quad (1.3)$$

is used when Δ_{pd} is large, but finite.

Typical values for the effective parameters can be obtained experimentally by measuring the magnetic excitations in the parent compounds using inelastic neutron scattering. For instance, the data for La_2CuO_4 [10] are well reproduced by considering a Heisenberg model that describes the spin excitations at low energy. First-, second-, and third-nearest neighbor magnetic exchange couplings, as well as a ring exchange coupling, are included in the Hamiltonian in order to get the right dispersion and intensity for the spin-wave scattering. A fit of the data allows us to obtain the values for all couplings. In fact this Heisenberg model is just the perturbative expansion in the kinetic term of the Hubbard model up to t^4 and the exchange couplings are directly related to the parameters U and t . From the extracted values of the exchange couplings, the values $t = 0.33$ eV and $U = 2.9$ eV are obtained for La_2CuO_4 . If the parameter t is chosen as energy unit, it gives $U = 8.8t$. The ARPES data (see Figure 1.6) show that in the cuprates the Fermi surface is hole-like although the density is smaller than 1. A parameter t' for the next-nearest-neighbor hopping appears therefore to be necessary to fit the shape of the Fermi surface. In fact, due to the van Hove singularities at momenta $(\pm\pi, 0)$ and $(0, \pm\pi)$ in the density of state, the parameter t' could play an important role in the cuprates as it brings the Fermi surface much closer to the singularities. Nevertheless, this study will focus mainly on the most fundamental Hubbard model (1.1), the effect of a t' parameter being

incorporated at the end.

At half-filling an antiferromagnetic instability occurs in the ground state of the repulsive Hubbard model. Now the question is to know whether a superconducting instability could appear when the density is reduced. In BCS theory a superconducting instability occurs if the coupling is negative. For a repulsive interaction, the BCS mean-field approximation applied to the on-site term gives:

$$\langle n_{i\uparrow}n_{i\downarrow} \rangle \approx \langle n_{i\uparrow} \rangle \langle n_{i\downarrow} \rangle + \langle c_{i\uparrow}^\dagger c_{i\downarrow} \rangle \langle c_{i\uparrow} c_{i\downarrow}^\dagger \rangle + \langle c_{i\uparrow}^\dagger c_{i\downarrow}^\dagger \rangle \langle c_{i\downarrow} c_{i\uparrow} \rangle \quad (1.4)$$

In the absence of antiferromagnetism, it can be written:

$$\langle n_{i\uparrow}n_{i\downarrow} \rangle \approx \frac{n^2}{4} + |\langle c_{i\uparrow}^\dagger c_{i\downarrow}^\dagger \rangle|^2 \quad (1.5)$$

where n is the average density. The second term of the right-hand side is always non-negative and vanishes if the ground state has not a broken symmetry. It means that in the best case, the on-site term is not unfavorable for a superconducting instability. This situation occurs when the wave function has a particular symmetry (like p-wave or d-wave) so that $\langle c_{i\uparrow}^\dagger c_{i\downarrow}^\dagger \rangle = 0$. We will explore two paths leading to a superconducting ground state:

- A small effective attraction between electrons on nearest-neighbor sites (of a non-specified origin) is added and treated at the mean-field level in the same way as the on-site interaction. Then the system has a superconducting instability for an appropriate symmetry of the order parameter.
- The model is not modified, but treated beyond mean-field theory. The strong electronic correlations may lead to an effective attraction and thus to (non s -wave) superconductivity.

The first path is followed in Chapter 2, while the remaining chapters are dedicated to the search for superconductivity in the repulsive Hubbard model.

Chapter 2

BCS approximation for nearest-neighbor attraction

Let us first look what happens at the mean-field level when an attractive nearest-neighbor term is added to the Hubbard Hamiltonian. The model is now given by

$$\hat{H} = t\hat{T} + U\hat{D} + V \sum_{\langle i,j \rangle} n_i n_j, \quad \text{with } U > 0 \text{ and } V < 0. \quad (2.1)$$

The BCS approximation consists in choosing the ground state of the BCS mean-field Hamiltonian as a trial state. As shown in Appendix B, this approximation leads to the following form for the variational energy of the model (2.1):

$$\begin{aligned} E(\Delta_{\vec{k}}) &= 2 \sum_{\vec{k}} \epsilon_{\vec{k}} v_{\vec{k}}^2 + \frac{U + 8V}{L^2} \cdot \frac{N^2}{4} + \frac{1}{L^2} \sum_{\vec{k}_1, \vec{k}_2, \sigma} W_{\sigma\sigma}(\vec{k}_2, \vec{k}_1) v_{\vec{k}_1}^2 u_{\vec{k}_2}^2 \\ &+ \frac{1}{L^2} \sum_{\vec{k}_1, \vec{k}_2, \sigma} W_{\sigma-\sigma}(\vec{k}_1, \vec{k}_2) u_{\vec{k}_1} v_{\vec{k}_1} u_{\vec{k}_2} v_{\vec{k}_2}, \end{aligned} \quad (2.2)$$

where $\epsilon_{\vec{k}} = -2t(\cos k_x + \cos k_y)$ is the tight-binding spectrum,

$$W_{\sigma\sigma'}(\vec{k}_1, \vec{k}_2) = \frac{U}{2} \delta_{\sigma, -\sigma'} + V \left[\cos(k_{1x} - k_{2x}) + \cos(k_{1y} - k_{2y}) \right] \quad (2.3)$$

is the coupling function and $N = \sum_{\vec{k}, \sigma} \langle c_{\vec{k}\sigma}^\dagger c_{\vec{k}\sigma} \rangle = 2 \sum_{\vec{k}} v_{\vec{k}}^2$ is the average particle number. The quantities $u_{\vec{k}}$ and $v_{\vec{k}}$ are related to the gap parameter $\Delta_{\vec{k}}$ by

$$u_{\vec{k}}^2 = 1 - v_{\vec{k}}^2 = \frac{1}{2} \left(1 + \frac{\xi_{\vec{k}}}{E_{\vec{k}}} \right), \quad (2.4)$$

where $\xi_{\vec{k}} = \epsilon_{\vec{k}} - \mu$ and $E_{\vec{k}} = \sqrt{\xi_{\vec{k}}^2 + \Delta_{\vec{k}}^2}$. In principle, any momentum dependence of the gap parameter $\Delta_{\vec{k}}$ should be allowed in minimizing this functional. However, the

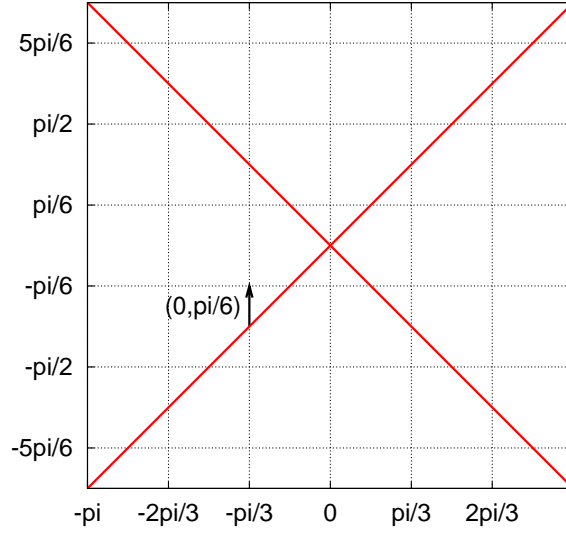


Figure 2.1: First Brillouin zone of the $L \times L$ square lattice with periodic-antiperiodic boundary conditions. This particular choice of boundary conditions allows us to shift the momenta by the vector $(0, \pi/L)$, in black on the figure, in order to avoid the diagonal momenta where the factors $u_{\vec{k}}$ and $v_{\vec{k}}$ are not defined when the chemical potential is such that $\xi_{\vec{k}} = 0$.

calculation is much easier if the symmetry of the gap parameter is imposed. In this study, three different symmetries have been considered:

$$\begin{aligned}
 \Delta_{\vec{k}} &= \Delta & s\text{-wave} \\
 \Delta_{\vec{k}} &= \Delta(\cos k_x + \cos k_y) & \text{extended } s\text{-wave} \\
 \Delta_{\vec{k}} &= \Delta(\cos k_x - \cos k_y) & d\text{-wave}
 \end{aligned}$$

Therefore only the variational parameter Δ has to be optimized. The energy (2.2) is computed numerically for a square lattice with periodic-antiperiodic boundary conditions. This choice of boundary conditions allows us to shift the \vec{k} points in the First Brillouin Zone (see Fig. 2.1) in order to avoid the diagonal momenta that can lead to an ill-defined BCS state for the d -wave symmetry when the density is such that $\xi_{\vec{k}^*} = 0$ for \vec{k}^* on the diagonal. Let us first study the pure Hubbard model ($V = 0$) on the square lattice (30×30). Figure 2.2 gives the kinetic, potential and total energies as a function of the gap parameter.

The opening of a gap at the Fermi surface is not favorable for the kinetic energy. For a small gap, this energy increases rather slowly in the extended s -wave symmetry, as compared to simple s -wave or d -wave. The results for the potential energy corroborate the expected behavior in the mean-field approximation. For $V = 0$, the whole

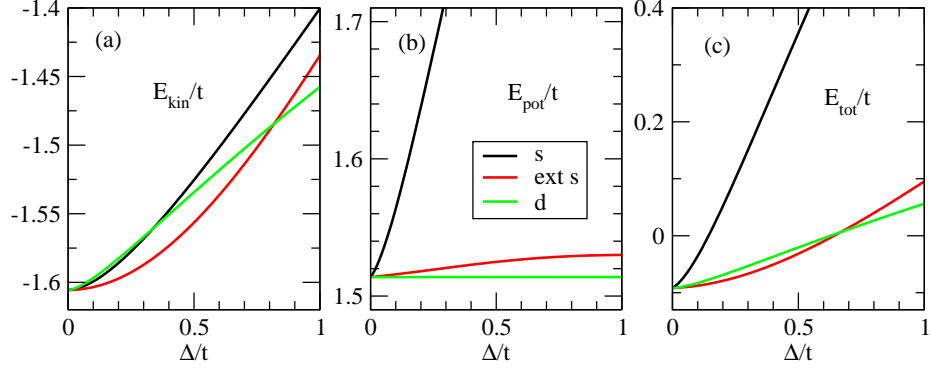


Figure 2.2: Kinetic, potential and total energies as functions of the gap parameter for a lattice size 30×30 , $U = 8t$, $V = 0$ and a density $n = 0.87$. Three different symmetries are considered.

gap dependence of the potential energy is in the last term of equation (2.2), which can be written

$$\frac{U}{L^2} \left(\sum_{\vec{k}} \frac{\Delta_{\vec{k}}}{2\sqrt{\xi_{\vec{k}}^2 + \Delta_{\vec{k}}^2}} \right)^2. \quad (2.5)$$

As this contribution is positive for $\Delta \neq 0$, the opening of a gap Δ cannot be favorable when $U > 0$. In the best situation, the gap symmetry is such as $\sum_{\vec{k}} \Delta_{\vec{k}}/E_{\vec{k}} = 0$ and then the potential energy does not depend on Δ . This is the case for d -wave symmetry. Figure 2.2(b) also shows that the extended s -wave symmetry, where electrons are paired on nearest-neighbor sites, is effective in avoiding the strong on-site repulsion, whereas the simple s -wave symmetry is strongly affected. The total energy indicates that no pairing occurs in the Hubbard model at mean-field level. Moreover, it can be noted that for $\Delta < \approx 0.67$ the extended s -wave is less unfavorable than the d -wave pairing.

Now let us see what happens when the nearest-neighbor attraction is switched on. The kinetic, potential and total energies are computed for a system size 30×30 and for a rather large attraction, $V = -t$. Results are given in Figure 2.3. Of course, the kinetic energy does not depend on the parameter V . For both d -wave and extended s -wave symmetry, the gap parameter describes a pairing of electrons located on nearest-neighbor sites of the lattice. It is therefore not surprising to observe a decrease of the potential energy when Δ is increased, due to the binding energy of the attractive term. However this effect is less pronounced for the extended s -wave. It results that for this latter symmetry, the gain in E_{pot} cannot compensate the kinetic energy and a gap is found in the ground state only for d -wave symmetry.

The density dependence of the optimal gap is given in Figure 2.4 for $U = 4t$ and different values of the attraction V . The gap is found to be maximum at half-filling, at least for large values of V , and decreases with increasing hole concentration. A small

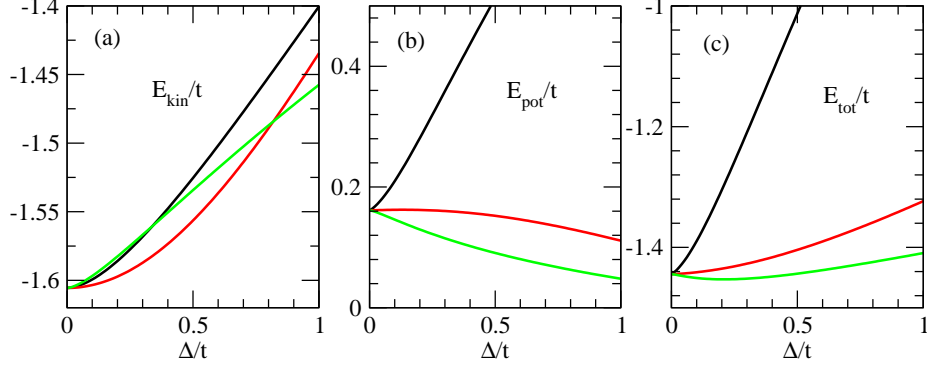


Figure 2.3: Kinetic, potential and total energies as functions of the gap parameter for a lattice size 30×30 , $U = 8t$, $V = -t$ and a density $n = 0.87$. The black, red and green curves correspond respectively to the s -wave, extended s -wave and d -wave symmetries.

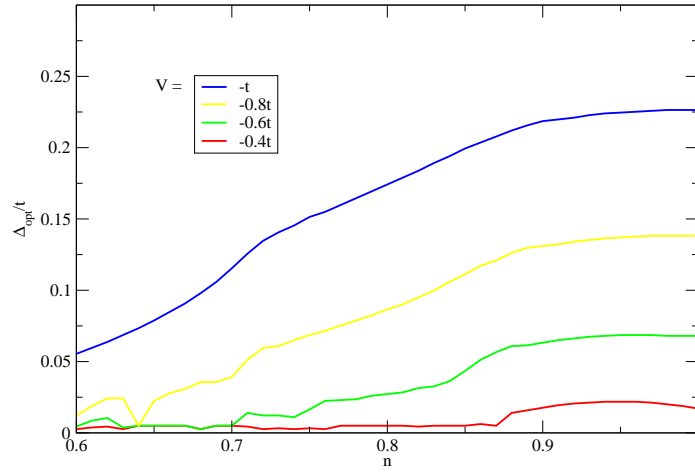


Figure 2.4: Optimal gap parameter (with d -wave symmetry) as a function of density for various strengths of the nearest-neighbor attraction. The lattice size is 30×30 and $U = 4t$. For $V > -0.3t$, a pairing instability is no longer favorable for any density.

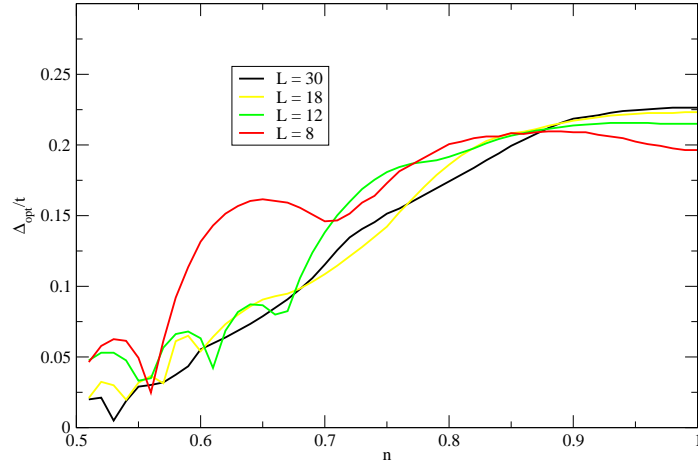


Figure 2.5: Size dependence of the optimal gap parameter as a function of density, for $U = 4t$ and $V = -t$. For small lattice sizes, the gap oscillates and has pronounced minima for some particular fillings corresponding to filled shells. This phenomenon occurs especially for small Δ_{opt} .

gap is still present for $V = -0.4t$ in the range $1 \geq n \gtrsim 0.87$. For this coupling the maximum gap is no longer at half-filling, but at a density of ~ 0.95 . For $V \geq -0.3t$ the opening of a pairing gap is not favorable at any density. It means that the critical attraction for the appearance of superconductivity is $V_{crit} \approx -0.3t$. We note that these results do not depend on the value of the on-site repulsion U .

2.1 Size effects

The system size used in this calculation is quite large (30×30). However, it is numerically much more demanding to go beyond the mean-field level, where such a system size cannot be reached. Therefore it is illustrative to estimate the size dependence for the BCS approximation of this simple model. Figure 2.5 shows the optimal gap as a function of density for different system sizes.

For small system sizes, the gap parameter oscillates around the value obtained for the 30×30 lattice. These oscillations are size effects encountered at particular fillings for these particular boundary conditions. They can be understood by considering two different situations. First let us assume that the density corresponds to complete filling of the highest occupied levels. It means that all momenta in the first Brillouin zone are away from the Fermi surface. For small system sizes the level spacing exceeds the gap parameter and we may assume $|\Delta_{\vec{k}}| \ll |\xi_{\vec{k}}|$. In this case the terms in the sum of (2.5) are given by

$$\frac{\Delta_{\vec{k}}}{2\sqrt{\xi_{\vec{k}}^2 + \Delta_{\vec{k}}^2}} \approx \frac{\Delta_{\vec{k}}}{2|\xi_{\vec{k}}|} \ll 1.$$

Therefore the sum (2.5) (and similarly the corresponding term proportional to V) is small. Now let us choose a density such as $\xi_{\vec{k}^*} = 0$ for some momenta \vec{k}^* (partial filling of the highest occupied levels). By symmetry, two or four \vec{k}^* are on the Fermi surface. Moreover, for these particular boundary conditions, these momenta belong either all to the part where the d -wave gap is positive or all to the part where it is negative (see Fig. 2.1). These points give a large contribution to the sum (2.5),

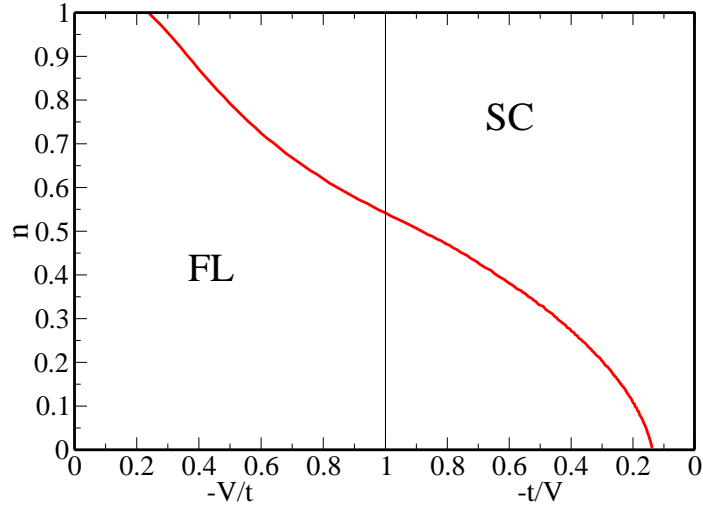
$$\sum_{\vec{k}^*} \frac{\Delta_{\vec{k}^*}}{2\sqrt{\xi_{\vec{k}^*}^2 + \Delta_{\vec{k}^*}^2}} \simeq \frac{1}{2} N_{\vec{k}^*} \text{sign}(\Delta_{\vec{k}^*})$$

where $N_{\vec{k}^*}$ is the number of momenta with $\xi_{\vec{k}^*} = 0$. The variational energy is therefore too large for small Δ and the optimal gap is overestimated. Figure 2.5 confirms that these size effects are especially large when both the optimal gap and the lattice size are small.

Anderson pointed out a long time ago that for finite systems, superconductivity should disappear when the system size becomes sufficiently small [11]. The reason is that the Fermi surface instability occurs essentially within a layer of width Δ around the Fermi energy (for s -wave symmetry), which should at least contain one occupied and one empty single-electron energy level for promoting a Cooper pair. More precisely, Anderson's argument states that superconductivity disappears as soon as the single-electron energy level spacing $\Delta\epsilon_{\vec{k}}$ (which increases when the system size is decreased) is equal to the bulk gap parameter Δ . For d -wave symmetry, the same argument may be applied to the antinodal region where the gap is maximal. Close to half-filling, we estimate the energy spacing at the Fermi surface using the relation:

$$\Delta\epsilon_{\vec{k}} = \left| \frac{\partial \epsilon_{\vec{k}}}{\partial k_y} \right|_{k_y = \frac{\pi}{L}} \cdot \Delta k_y \approx \left(\frac{2\pi}{L} \right)^2 t. \quad (2.6)$$

In our calculation, this energy spacing is equal to the bulk gap ($\approx 0.2t$ close to half-filling) for a lattice size 14×14 . It means that for our 8×8 lattice, Anderson's argument would imply a vanishing gap parameter ($\Delta\epsilon_{\vec{k}} \approx 0.6t > \Delta \approx 0.2t$). A somewhat different criterion states that superconductivity survives as long as the coherence length $\xi_c = \hbar v_F / \Delta \approx 2t / \Delta$ does not exceed the lattice size. This leads to a critical lattice size of 10×10 close to half-filling. However, there is no sharp transition between a superconducting regime and a normal state. Rigorous results for the reduced BCS Hamiltonian (*i.e.* beyond mean-field) in fact show a smooth crossover between superconducting and fluctuation-dominated regimes [12],[13]. These results

Figure 2.6: Phase diagram of the extended Hubbard model with $U = 8t$.

indicate that a lattice which is smaller, but close to the critical size given by Anderson's argument, like our 8×8 lattice, can already capture essential features of the bulk behavior.

2.2 Phase diagram

The BCS gap equation for the model (2.1) is given by:

$$\Delta_{\vec{k}} = \frac{1}{L^2} \sum_{\vec{k}'} W_{\vec{k}\vec{k}'} \frac{\Delta_{\vec{k}'}}{2\sqrt{\xi_{\vec{k}'}^2 + \Delta_{\vec{k}'}^2}} \quad (2.7)$$

with $W_{\vec{k}\vec{k}'} = \sum_{\sigma, \sigma'} W_{\sigma\sigma'}(\vec{k}, \vec{k}')$. A phase diagram for the superconducting transition can be obtained by solving numerically this equation in the thermodynamic limit with the condition $\Delta = 0$. This phase diagram is given in Figure 2.6. For a fixed value of the attractive parameter $|V| > 0.25t$, the system is in a superconducting phase at half-filling (here the possibility of an antiferromagnetic phase is not taken into account) and undergoes a transition towards a Fermi liquid upon hole doping. For $|V| \gtrsim 7t$, d -wave pairing is strong enough to survive at any density.

This simple calculation shows that a superconducting instability appears already at the mean-field level when a nearest-neighbor attraction is added to the Hubbard model. Despite the strong on-site Coulomb repulsion, pairing with unconventional angular momentum can occur. However, this attractive term is purely phenomenological and has no microscopic basis (for instance through band structure calculations). Its origin could be searched among the degrees of freedom that are usually not considered in ab initio band structure calculations, such as phonons. An effective attraction

then appears when these degrees of freedom are integrated out. Another possibility, which in our opinion is much more appealing, is an the attraction resulting from the response of the electrons to the electronic background itself. In other words, the superconducting instability could arise from correlation effects already present in the purely electronic model.

Chapter 3

Superconductivity from purely repulsive interaction

3.1 Kohn-Luttinger mechanism

W. Kohn and J. M. Luttinger have shown that a superconducting instability has to occur in weakly interacting Fermi systems at low enough temperature [14], provided that no other Fermi surface instability occurs at a higher temperature. This statement is true both for an attractive or a repulsive interaction. How can the electron pairing be understood in the repulsive case? Let us consider for a while a charged impurity in a normal metal. We know that the electron distribution is modified in the vicinity of the impurity in such way that the impurity potential is screened. Looking at the Fourier transform of the impurity distribution, a component with $q < 2k_F$ is screened by creating infinitesimal excitations of electrons at the Fermi surface (with $\Delta k = q$). Now, it is clear that the electrons are much less effective in screening the fast component ($q > 2k_F$), as such low-energy excitations do not exist (see Fig. 3.1). Actually the sharpness of the Fermi surface in a normal metal leads to a singularity in the dielectric function for $q = 2k_F$ and as a direct consequence, the effects of impurity potential do not vanish at large distances. Instead, the potential has an oscillatory tail in real space with attractive portions. In a pure Fermi system, the Coulomb interaction is screened in the same manner but now electrons play the role of impurities and of screening charges at the same time (in a homogeneous positively charged background). The study of the effective interaction allows one to show that the sharpness of the Fermi surface still leads to some attractive components and thus to pairing. This route to the superconductivity is called “Kohn-Luttinger mechanism”.

We look for a pairing instability and therefore restrict ourselves to the BCS vertex of the interaction, that is the scattering from one to another Cooper pair. In second order perturbation theory, the BCS vertex is composed of the bare potential and the

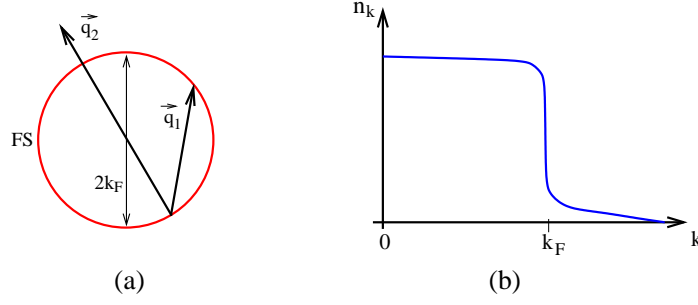


Figure 3.1: (a) A slow Fourier transform component of the impurity distribution with $|\vec{q}_1| < 2k_F$ can be screened by the particle-hole excitation with $\Delta\vec{k} = \vec{q}_1$, but not by a fast component with $|\vec{q}_2| > 2k_F$. (b) Schematic representation of the momentum density in a Fermi liquid.

five second order contributions given in Fig. 3.2.

The screening of the interaction between two particles by the fermionic background is obtained by particle-hole excitations at the Fermi surface, which is described by the zero sound “ZS” diagrams (the “BCS” diagram is related to particle-particle interaction). A logarithmic singularity is found in the contribution of these diagrams to the BCS vertex, when q approaches $2k_F$ (see [14],[15]):

$$\Gamma(q) \sim [(2k_F)^2 - q^2] \ln |(2k_F)^2 - q^2| + \Gamma_{reg}(q^2) \quad (3.1)$$

where $\Gamma_{reg}(q^2)$ is the regular part of this contribution.

At very small temperature, only scattering of electrons near the Fermi surface are important. Therefore \vec{k}_1, \vec{k}_2 are chosen on the Fermi surface and the BCS vertex can be parametrized by the angle θ between \vec{k}_1 and \vec{k}_2 : $\Gamma_{BCS}(\vec{k}_1, \vec{k}_2) = \Gamma_{BCS}(\cos \theta)$. Then Γ_{BCS} can be expanded in the basis of Legendre polynomials

$$\Gamma(\cos \theta) = \sum_l \Gamma_l (2l + 1) P_l(\cos \theta) \quad (3.2)$$

where

$$\Gamma_l = \int_0^\pi d(\cos \theta) P_l(\cos \theta) \Gamma(\cos \theta) . \quad (3.3)$$

For large l , the singular part of (3.1) behaves as [14],[15]:

$$\Gamma_{l,ZS'} = \int_0^\pi d(\cos \theta) P_l(\cos \theta) \Gamma_{ZS',sing}(\cos \theta) \sim \frac{(-1)}{l^4} . \quad (3.4)$$

The minus sign indicates that this term is attractive. On the other hand, all other contributions are analytic (in particular the bare vertex is assumed to be regular) and therefore their coefficients in the Legendre polynomials expansion have to fall

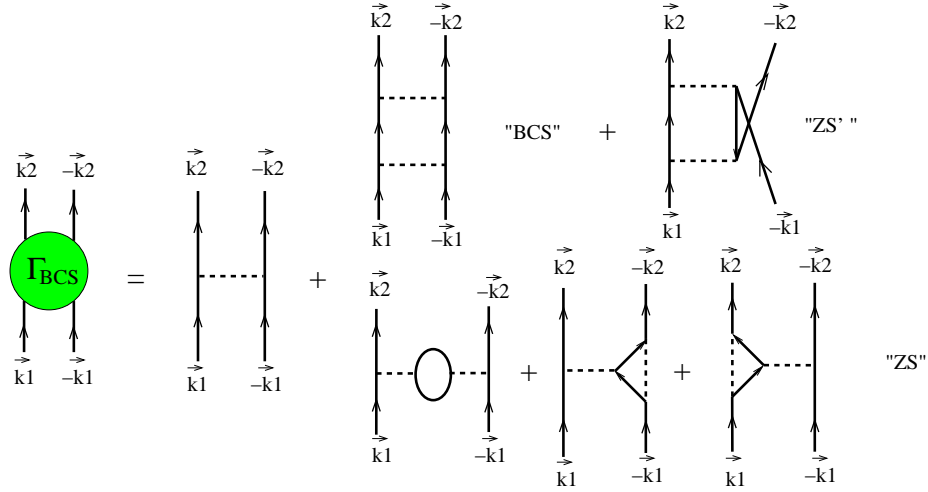


Figure 3.2: Diagrammatic representation of the BCS vertex in second order perturbation theory.

off exponentially in l : $\Gamma_{l,reg} \sim e^{-l}$, in order to ensure the convergence of the sum (3.2). It results that components with sufficiently large angular momentum l are dominated by the attractive interaction arising from the singularity. It means that for a particular symmetry of the pairing, a BCS-type gap equation has necessarily a solution. A Fermi liquid is therefore not stable at low temperature and unless another instability emerges at higher temperature, the system undergoes a superconducting transition.

The theorem of Kohn and Luttinger indicates that it makes sense to look for superconductivity in the two-dimensional Hubbard model. Before studying the intermediate coupling regime, which is the most relevant for the cuprates, let us consider both limits of weak and infinite coupling.

3.2 Weak coupling: Renormalization Group

The Renormalization Group is a theory that has been very successful in studying weakly interacting fermion systems [16]. This approach consists of reducing the phase space of the system by including the effect of the eliminated degrees of freedom in the renormalisation of some coupling constants or interaction vertices. It allows one to study how a non-interacting system evolves into a Fermi liquid when a weak interaction is taken into account and also how Fermi liquid theory breaks down when some instabilities emerge at low temperatures (a weakly interacting system is always a Fermi liquid at high enough temperatures). At low temperatures, the scattering processes leading to an instability involve only the low energy electrons (close to the

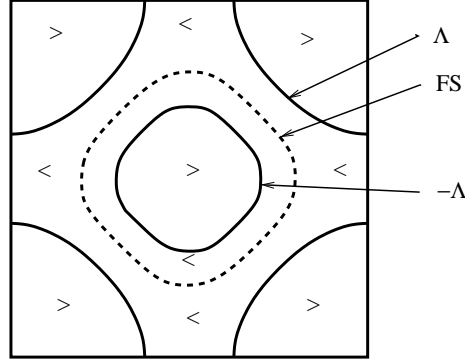


Figure 3.3: The first Brillouin zone is separated in two parts corresponding to the slow modes (<) in a shell $\pm\Lambda$ around the Fermi surface and the fast modes (>) that will be integrated out in the renormalization process.

Fermi surface). Therefore we can learn a lot about the nature of the instability by eliminating the high energy scattering events (called the fast modes) and by simultaneously modifying the couplings or vertices in such way that the physics remains unchanged. This is realized in the renormalization group by introducing an energy cutoff Λ as defined in Figure 3.3, which divides the first Brillouin zone into two parts: the slow modes (<) and the fast modes (>).

When the cutoff Λ is reduced, the flow of the interaction vertices can be obtained by fixing the condition that the partition function is invariant under this transformation. If a weak interaction leads to an instability at low (but finite) temperatures for some particular scattering processes, the corresponding vertices have to diverge in order to compensate the reduction of available scattering states due to the reduced cut-off. Usually the renormalized interactions depend on both momenta and energies involved in a process, even if the bare interaction does not. The renormalization procedure therefore allows us to extract the dominant instability of the system and also to estimate the critical temperature where this instability occurs.

For a weakly interacting fermion system on the square lattice, the Hamiltonian for a general form of the interaction is written in momentum space:

$$\hat{H} - \mu\hat{N} = \sum_{\vec{k}\sigma} \xi_{\vec{k}} c_{\vec{k}\sigma}^\dagger c_{\vec{k}\sigma} + \frac{1}{2} \sum_{\vec{k}_1\vec{k}_2\vec{k}_3\sigma} U_0(\vec{k}_1, \vec{k}_2, \vec{k}_3) c_{\vec{k}_1+\vec{k}_2-\vec{k}_3-\sigma}^\dagger c_{\vec{k}_2-\sigma} c_{\vec{k}_3\sigma}^\dagger c_{\vec{k}_1\sigma} \quad (3.5)$$

where $c_{\vec{k}\sigma}^\dagger$ creates an electron with momentum \vec{k} and spin σ , $\xi_{\vec{k}} = -2t(\cos k_x + \cos k_y) - \mu$ and t , U_0 , μ are the system parameters corresponding respectively to the transfer integral between nearest-neighbor sites of the lattice, the bare vertex and the chemical potential. Here we assume a spin-independent interaction and a system which is translationally invariant. The partition function is given by

$$Z = \int \mathcal{D}\bar{\Psi} \mathcal{D}\Psi e^{S\{\Psi\}} \quad (3.6)$$

where the functional integration is over Grassmann variables. The action is

$$\begin{aligned} S\{\Psi\} &= S_0\{\Psi\} + S_I\{\Psi\} = T \sum_{\omega_n, \vec{k}, \sigma} \bar{\Psi}_{\vec{k}\sigma} (i\omega_n - \xi_{\vec{k}}) \Psi_{\vec{k}\sigma} \\ &+ \frac{1}{2} \sum_{\sigma\sigma'} T^3 \sum_{\vec{K}_1, \vec{K}_2, \vec{K}_3} U_0(\vec{K}_1, \vec{K}_2, \vec{K}_3) \bar{\Psi}_{\vec{K}_3\sigma} \bar{\Psi}_{\vec{K}_1 + \vec{K}_2 - \vec{K}_3\sigma'} \Psi_{\vec{K}_2\sigma'} \Psi_{\vec{K}_1\sigma} \end{aligned}$$

where the energy-momentum vector is defined by $\vec{K} = (\omega_n, \vec{k})$.

To determine the effective action for the slow modes, the energy cutoff is introduced in the electronic variables which are written

$$\Psi_{\vec{K}\sigma} = \theta(|\xi_{\vec{k}}| - \Lambda) \Psi_{>, \vec{K}\sigma} + \theta(\Lambda - |\xi_{\vec{k}}|) \Psi_{<, \vec{K}\sigma} . \quad (3.7)$$

Now the slow modes $\Psi_{<, \vec{K}\sigma}$ are inside the shell $\pm\Lambda$ around the Fermi surface. Only the interactive part of the action mixes the slow modes and the fast modes and we can write

$$S\{\Psi_{<}, \Psi_{>}\} = S_0\{\Psi_{<}\} + S_0\{\Psi_{>}\} + S_I\{\Psi_{<}, \Psi_{>}\} . \quad (3.8)$$

Then

$$\begin{aligned} Z &= \int \mathcal{D}\bar{\Psi}_{<} \mathcal{D}\Psi_{<} \int \mathcal{D}\bar{\Psi}_{>} \mathcal{D}\Psi_{>} e^{S_0\{\Psi_{<}\}} e^{S_0\{\Psi_{>}\}} e^{S_I\{\Psi_{<}, \Psi_{>}\}} \\ &= \int \mathcal{D}\bar{\Psi}_{<} \mathcal{D}\Psi_{<} e^{S_0\{\Psi_{<}\}} \int \mathcal{D}\bar{\Psi}_{>} \mathcal{D}\Psi_{>} e^{S_0\{\Psi_{>}\}} e^{S_I\{\Psi_{<}, \Psi_{>}\}} \\ &\equiv \int \mathcal{D}\bar{\Psi}_{<} \mathcal{D}\Psi_{<} e^{S_\Lambda\{\Psi_{<}\}} \end{aligned} \quad (3.9)$$

where $S_\Lambda\{\Psi_{<}\}$ is the effective action, defined on the subspace of the slow modes. We have:

$$\begin{aligned} e^{S_\Lambda\{\Psi_{<}\}} &= e^{S_0\{\Psi_{<}\}} \int \mathcal{D}\bar{\Psi}_{>} \mathcal{D}\Psi_{>} e^{S_0\{\Psi_{>}\}} e^{S_I\{\Psi_{<}, \Psi_{>}\}} \\ &= e^{S_0\{\Psi_{<}\}} \frac{\int \mathcal{D}\bar{\Psi}_{>} \mathcal{D}\Psi_{>} e^{S_0\{\Psi_{>}\}} e^{S_I\{\Psi_{<}, \Psi_{>}\}}}{\int \mathcal{D}\bar{\Psi}_{>} \mathcal{D}\Psi_{>} e^{S_0\{\Psi_{>}\}}} \cdot \underbrace{\int \mathcal{D}\bar{\Psi}_{>} \mathcal{D}\Psi_{>} e^{S_0\{\Psi_{>}\}}}_{Z_{0>}} \\ &= e^{S_0\{\Psi_{<}\}} \langle e^{S_I\{\Psi_{<}, \Psi_{>}\}} \rangle_{0>} = e^{S_0\{\Psi_{<}\}} e^{(\langle S_I \rangle_{0>} + (\langle S_I^2 \rangle - \langle S_I \rangle^2)/2 + \dots)} . \end{aligned}$$

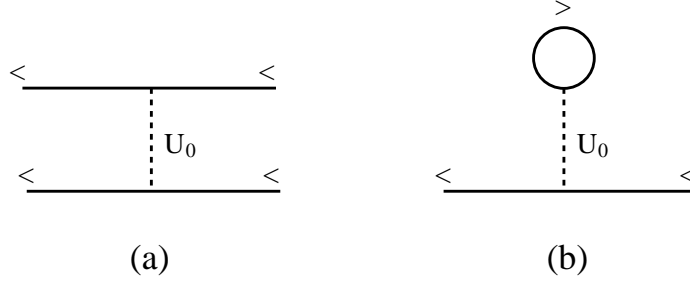


Figure 3.4: Diagrams corresponding to the lowest order cumulant in Equation 3.11.

The bracket $\langle \rangle_{0>}$ means the average with respect to the fast modes with action S_0 . The factor $Z_{0>}$ has been dropped as it is independent of the slow modes and can be taken into account by adding a constant term to the effective action. The cumulant expansion has been invoked to get the last equality. Now the effective action can be written

$$S_\Lambda\{\Psi_<\} = S_0\{\Psi_<\} + S_{I\Lambda} \quad (3.10)$$

where

$$S_{I\Lambda} = \langle S_I \rangle_{0>} + (\langle S_I^2 \rangle - \langle S_I \rangle^2)/2 + \dots \quad (3.11)$$

Therefore $S_{I\Lambda}$ is a series expansion in powers of the bare interaction U_0 . Using the linked cluster theorem, it can be represented by all connected diagrams obtained from S_I , with the slow modes as external legs (at least two, for the lowest order cumulant) and the fast modes as internal lines. The diagrams for the lowest order cumulant are given in Figure 3.4.

The effective two-particle, four-particle, ... vertices at a cutoff Λ are defined by:

$$S_\Lambda\{\Psi_<\} := \Gamma_{2\Lambda} \bar{\Psi}\Psi + \Gamma_{4\Lambda} \bar{\Psi}\bar{\Psi}\Psi\Psi + \Gamma_{6\Lambda} \bar{\Psi}\bar{\Psi}\bar{\Psi}\Psi\Psi\Psi + \dots \quad (3.12)$$

where the electron variables are now restricted to the shell $\pm\Lambda$ around the Fermi surface. The diagram (a) in Figure 3.4 renormalizes the four-particle vertex $\Gamma_{4\Lambda}$, while the diagram (b) renormalizes the two-particle vertex $\Gamma_{2\Lambda}$.

This diagrammatic representation allows us to derive a flow equation for the renormalization of each vertex. Various formulations are possible to get this flow equation. The main steps leading to this equation in the Kadanoff-Wilson-Polchinski formulation are given in appendix C. Another formulation can be found in [17].

In the case of the two-dimensional Hubbard model, the bare interaction does not depend on momenta $U_0(\vec{k}_1, \vec{k}_2, \vec{k}_3) = \text{constant} = U$. However, the effective interaction $U_l = \Gamma_{4\Lambda}$ will become more and more momentum-dependent during the renormalization process. The marginal part of the dependence of U_l (which leads to divergences)

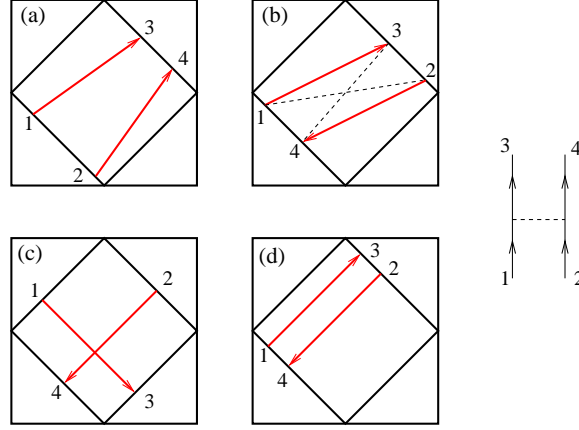


Figure 3.5: The marginal scattering processes involve momenta at the Fermi surface (given here at half-filling). (a) and (c) are umklapp processes, (b) is a typical process in the Cooper channel ($\vec{k}_1 + \vec{k}_2 = (0, 0)$) and (d) is a typical process in the nesting channel ($\vec{k}_3 - \vec{k}_1 = (\pi, \pi)$).

includes only the interactions between electrons at the Fermi surface. The momentum dependence perpendicular to the Fermi surface as well as the energy dependence are found to be irrelevant. The effective interactions are therefore restricted to momenta on the Fermi surface and are given by three angles of the particles (the fourth is obtained by momentum conservation) $U_l(\vec{K}_1, \vec{K}_2, \vec{K}_3) \rightarrow U_l(\theta_1, \theta_2, \theta_3)$. Some of these marginal interactions are shown in Figure 3.5. Momenta on the Fermi surface are discretized in order to compute the flow of the interactions numerically. The flow equation C.5 is solved by successive iterations for each coupling constant (in other words for each particular scattering process). It is important to note that all kind of scattering processes are taken into account on an equal footing in this calculation. The result for the flow of several coupling constants for a Coulomb parameter $U = 4t/3$ is given in Figure 3.6. We observe that some coupling constants diverge strongly to $+\infty$ when the cutoff is reduced. They correspond to scattering processes with a good nesting (momentum transfer $\approx (\pm\pi, \pm\pi)$), as in Figure 3.5(d). Another kind of coupling constants diverges to $-\infty$ after changing their sign. This is the typical behavior for scattering processes obeying the Cooper condition ($\vec{k}_{tot} = 0$) and without nesting, as in Figure 3.5(b). The renormalization procedure shows that an effective interaction that is attractive appears in the “BCS” channel. Finally, some coupling constants almost do not diverge, related to processes that are far from both nesting and Cooper conditions.

The flow of the interactions shows that both antiferromagnetic and superconducting instabilities can occur at very low temperature. In order to know which instability is dominant for a given chemical potential, the effective interaction for antiferromag-

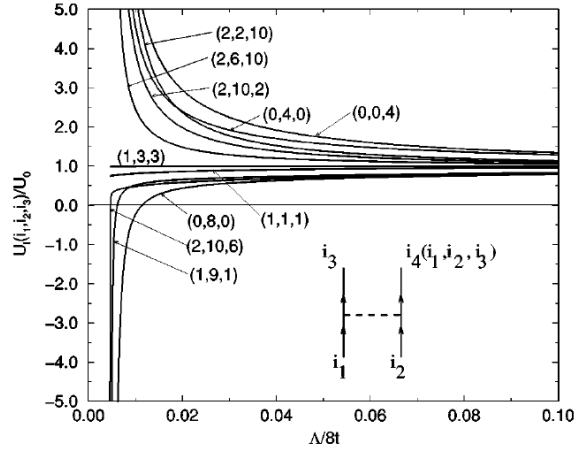


Figure 3.6: Flow of the coupling constant corresponding to typical scattering processes, during the renormalization procedure. The initial interaction is $U = 4t/3$ and the chemical potential is $\mu = -0.003$ corresponding to a slightly doped system. From [18].

netism and for superconductivity are defined by:

$$V_l^{AF}(\theta_1, \theta_2) = -U_l(\theta_2, \theta_1, \tilde{\theta}_1) \quad \text{with} \quad \vec{k}(\theta_1) - \vec{k}(\tilde{\theta}_1) = (\pi, \pi) \quad (3.13)$$

$$V_l^{SC}(\theta_1, \theta_2) = U_l(\theta_1, \theta_1 + \pi, \theta_2) \quad (3.14)$$

$V_l^{AF}(\theta_1, \theta_2)$ and $V_l^{SC}(\theta_1, \theta_2)$ describe antiferromagnetic and superconducting scattering processes, respectively. As the angles θ_1 and θ_2 are discretized, these effective interactions are matrices that can be straightforwardly diagonalized. The most attractive (most negative) eigenvalue is expected to give the most divergent contribution. Moreover, the symmetry of the related correlation function is given by the symmetry of the corresponding eigenvector. The most attractive eigenvalues for the effective antiferromagnetic and superconducting interactions are written respectively $V_{c,l}^{AF}$ and $V_{c,l}^{SC}$. Figure 3.7 shows the flow of $V_{c,l}^{AF}$ and $V_{c,l}^{SC}$ for different chemical potentials.

The most diverging eigenvector for the antiferromagnetic effective interaction is found to be in a s -wave channel (A_1 representation of the D_4 group), while the superconducting effective interaction diverges in the d -wave ($d_{x^2-y^2}$) channel corresponding to the B_1 representation. At half-filling, $V_{c,l}^{AF}$ diverges clearly faster than $V_{c,l}^{SC}$. When the system is doped, the divergence of $V_{c,l}^{AF}$ is softened and $V_{c,l}^{SC}$ becomes dominant (curve D).

The perturbative renormalization group shows therefore that an antiferromagnetic instability occurs at half-filling in the two-dimensional Hubbard model with weak repulsion U . When the density is moderately reduced, a d -wave superconducting instability becomes dominant.

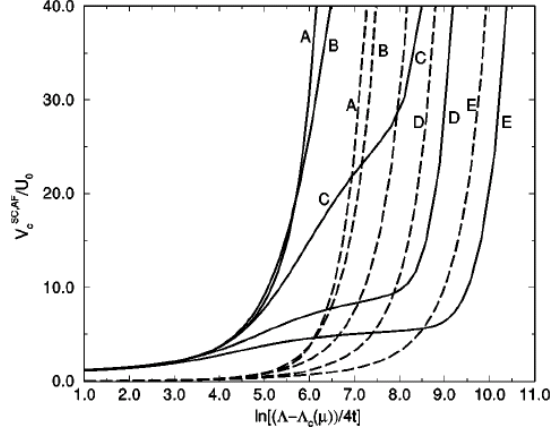


Figure 3.7: Flow of the most attractive eigenvalue (absolute value) for the antiferromagnetic (dashed line) or superconducting (continuous line) instability. The system is half-filled for the curves A and then more and more doped. The corresponding chemical potentials are $|\mu|/t \approx 0$ (A), 0.0027 (B), 0.0072 (C), 0.0196 (D) and 0.0324 (E). From [18].

3.3 Large U limit: the t-J model

If a pairing instability with a d -wave symmetry is found to be dominant at moderate doping in the case of a weak interaction, the obvious next question is what happens at the opposite limit of a strong interaction. Is it still favorable to break a symmetry in the ground state of the Hubbard model when $U \rightarrow \infty$? In this limit, a doubly occupied site has a prohibitively high energy and the system stays in the lower Hubbard band when $n \leq 1$. Then the Hubbard model (1.1) can be transformed into an effective Hamiltonian restricted to this subband and called the “t-J model”. This is realized by applying a canonical transformation suppressing all first order processes (of order t) which couple the lower and the upper Hubbard bands [19]. This Hamiltonian has the following form:

$$\begin{aligned}
 \hat{H}_{eff} &= \hat{T} + \hat{H}_{eff}^{(2)} + \hat{H}_{eff}^{(3)}, \text{ with:} \\
 \hat{T} &= -t \sum_{\langle i,j \rangle, \sigma} (a_{i\sigma}^\dagger a_{j\sigma} + a_{j\sigma}^\dagger a_{i\sigma}) \\
 \hat{H}_{eff}^{(2)} &= \frac{4t^2}{U} \sum_{\langle i,j \rangle} (\vec{S}_i \vec{S}_j - \frac{\hat{n}_i \hat{n}_j}{4}) \\
 \hat{H}_{eff}^{(3)} &= -\frac{t^2}{U} \sum_{i, \tau \neq \tau', \sigma} (a_{i+\tau, \sigma}^\dagger a_{i, -\sigma}^\dagger a_{i, -\sigma} a_{i+\tau', \sigma} + a_{i+\tau, -\sigma}^\dagger a_{i, \sigma}^\dagger a_{i, -\sigma} a_{i+\tau', \sigma})
 \end{aligned} \tag{3.15}$$

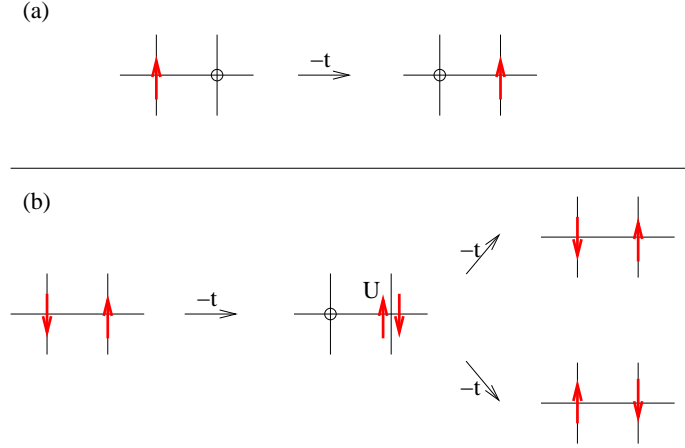


Figure 3.8: (a): Hopping corresponding to the first term of the effective Hamiltonian. (b): Virtual process of second order in the hopping parameter associated with the Heisenberg term.

where $a_{i,\sigma}^\dagger = (1 - n_{i,-\sigma})c_{i,\sigma}^\dagger$ creates an electron with spin σ on site i only when this site is not already occupied by an electron of opposite spin and \vec{S} is the usual spin operator. The first term is the kinetic energy of the holes, whereas the second term is the Heisenberg term describing the low-energy spin excitations. This second order term (of order t^2/U) is generated by the canonical transformation. The “virtual” process involved is the hopping of an electron to a nearest-neighbor site which is already occupied and the way back to the original site with or without spin flip, as shown in Figure 3.8. This process allows to gain some delocalization energy, but it can take place only when the nearest-neighbor site is occupied by an electron with opposite spin and therefore the Heisenberg term has an antiferromagnetic character. The third term corresponds to second order “3-site” processes (see Fig. 3.9). When the number of electrons per site n is equal to 1, only the antiferromagnetic Heisenberg term survives.

3.3.1 The variational method

The variational method relies on the variational principle, which states that if E_0 is the true ground state energy of the Hamiltonian \hat{H} , then for any state $|\Psi\rangle$ of the Hilbert space we have:

$$E(\Psi) := \frac{\langle \Psi | \hat{H} | \Psi \rangle}{\langle \Psi | \Psi \rangle} \geq E_0. \quad (3.16)$$

The variational method consists in choosing a family of states, labeled by some parameters, and in determining the best variational ground state by minimizing the

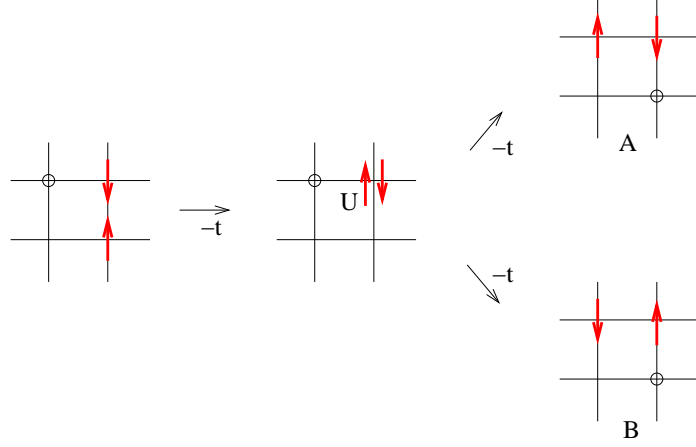


Figure 3.9: Virtual process of second order in the hopping parameter associated with the 3-site term of the effective Hamiltonian. The moves are of two types: second-neighbor hopping of a spin σ electron via an intermediate site which is singly occupied by a spin $-\sigma$ electron (A moves) or second-neighbor hopping with spin-flip, accompanied by flipping the spin at the intermediate site (B moves).

expectation value of energy with respect to these parameters. The result depends of course on the choice of parameters. In general, physical arguments have to be invoked to “guess” a reasonable ansatz.

Coming back to the issue of superconductivity in the t-J model, we may start with a BCS state, as in Appendix B. However, such a state admits doubly occupied sites, which have to be suppressed for $U \rightarrow \infty$. Therefore the Gutzwiller projector P_G , which removes double occupancy, is applied to the BCS state. The result is a “resonating-valence-bond” (RVB) state [20]:

$$\begin{aligned} |RVB\rangle &= P_G |BCS\rangle \\ &= P_G \prod_{\vec{k}} (u_{\vec{k}} + v_{\vec{k}} c_{\vec{k}\uparrow}^\dagger c_{-\vec{k}\downarrow}^\dagger) |0\rangle. \end{aligned} \quad (3.17)$$

This wave function does not have a well-defined number of particles. However, in the thermodynamic limit, the wave function is peaked around the average number of particles. Therefore, if the system is large enough it is totally equivalent to work with the $|RVB\rangle$ state or with its N-particle component $|\Psi^{(N)}\rangle$, which is defined as:

$$\begin{aligned} |\Psi^{(N)}\rangle &= P_N |RVB\rangle \\ &= P_G \left(\sum_{\vec{k}} a(\vec{k}) c_{\vec{k}\uparrow}^\dagger c_{-\vec{k}\downarrow}^\dagger \right)^{N/2} |0\rangle \end{aligned} \quad (3.18)$$

with

$$a(\vec{k}) = \frac{v_{\vec{k}}}{u_{\vec{k}}} = \frac{\Delta_{\vec{k}}}{\xi_{\vec{k}} + \sqrt{\xi_{\vec{k}}^2 + \Delta_{\vec{k}}^2}} . \quad (3.19)$$

This latter equality is readily obtained from the definition (B.9) of parameters $u_{\vec{k}}$ and $v_{\vec{k}}$. The Gutzwiller projector is easily written in real space:

$$P_G = \prod_i (1 - n_{i\uparrow} n_{i\downarrow}) . \quad (3.20)$$

Therefore we also write the state $|\Psi^{(N)}\rangle$ in real space, using the Fourier transform (see Appendix B)

$$c_{\vec{k}\sigma} = \frac{1}{L} \sum_{\vec{n}_i} e^{-i\vec{k}\cdot\vec{n}_i} c_{i\sigma} \quad (3.21)$$

in order to rewrite (3.18) as

$$\begin{aligned} |\Psi^{(N)}\rangle &= P_G \left[\sum_{\vec{k}} a(\vec{k}) \left(\frac{1}{L} \sum_{\vec{n}_i} e^{i\vec{k}\cdot\vec{n}_i} c_{i\uparrow}^\dagger \right) \left(\frac{1}{L} \sum_{\vec{n}_j} e^{-i\vec{k}\cdot\vec{n}_j} c_{j\downarrow}^\dagger \right) \right]^{N/2} |0\rangle \\ &= P_G \left[\sum_{\vec{n}_i, \vec{n}_j} a(\vec{n}_i - \vec{n}_j) c_{i\uparrow}^\dagger c_{j\downarrow}^\dagger \right]^{N/2} |0\rangle \end{aligned} \quad (3.22)$$

where the sum is over all lattice vectors and $a(\vec{n})$ is the Fourier transform of $a(\vec{k})$. It is useful to consider a simple case to see how this state can be written in the space of real configurations. In the case of 4 electrons on a 3×3 square lattice, (3.22) has the following form:

$$|\Psi^{(4)}\rangle = P_G \left[\sum_{\vec{n}_i, \vec{n}_j} a(\vec{n}_i - \vec{n}_j) c_{i\uparrow}^\dagger c_{j\downarrow}^\dagger \right]^2 |0\rangle \quad (3.23)$$

The effect of the Gutzwiller projector is to suppress configurations which contain both $c_{i\uparrow}^\dagger$ and $c_{i\downarrow}^\dagger$. A given configuration appears twice in this expansion. For instance, the configuration

$$|\uparrow: \vec{n}_2, \vec{n}_6 \downarrow: \vec{n}_5, \vec{n}_7\rangle = c_{2\uparrow}^\dagger c_{6\uparrow}^\dagger c_{5\downarrow}^\dagger c_{7\downarrow}^\dagger |0\rangle \quad (3.24)$$

is present in (3.23) with the coefficients

$$a(\vec{n}_2 - \vec{n}_5) a(\vec{n}_6 - \vec{n}_7) c_{2\uparrow}^\dagger c_{5\downarrow}^\dagger c_{6\uparrow}^\dagger c_{7\downarrow}^\dagger |0\rangle + a(\vec{n}_2 - \vec{n}_7) a(\vec{n}_6 - \vec{n}_5) c_{2\uparrow}^\dagger c_{7\downarrow}^\dagger c_{6\uparrow}^\dagger c_{5\downarrow}^\dagger |0\rangle .$$

If we commute the creation operators to obtain the order defined by (3.24), the coefficient of this configuration takes the form of a determinant:

$$\begin{aligned} & \left[-a(\vec{n}_2 - \vec{n}_5)a(\vec{n}_6 - \vec{n}_7) + a(\vec{n}_2 - \vec{n}_7)a(\vec{n}_6 - \vec{n}_5) \right] c_{2\uparrow}^\dagger c_{6\uparrow}^\dagger c_{5\downarrow}^\dagger c_{7\downarrow}^\dagger |0\rangle \\ = & - \begin{vmatrix} a(\vec{n}_2 - \vec{n}_5) & a(\vec{n}_2 - \vec{n}_7) \\ a(\vec{n}_6 - \vec{n}_5) & a(\vec{n}_6 - \vec{n}_7) \end{vmatrix} \left| \uparrow: \vec{n}_2, \vec{n}_6 \downarrow: \vec{n}_5, \vec{n}_7 \right\rangle. \end{aligned} \quad (3.25)$$

It is straightforward to generalize this argument to the case of N electrons and the wave function $|\Psi^{(N)}\rangle$ is now written

$$|\Psi^{(N)}\rangle = \sum_{\{\vec{n}_{i\uparrow}\}, \{\vec{n}_{j\downarrow}\}} \det[A(\{\vec{n}_{i\uparrow}\}, \{\vec{n}_{j\downarrow}\})] \left| \{\vec{n}_{i\uparrow}\}, \{\vec{n}_{j\downarrow}\} \right\rangle \quad (3.26)$$

where the sum is over all possible real space configurations and A is the $\frac{N}{2} \times \frac{N}{2}$ matrix with elements $a(\vec{n}_i - \vec{n}_j)$.

3.3.2 Variational Monte Carlo (VMC)

The variational Monte Carlo technique is an efficient way to compute numerically the variational energy of the system in the trial state $|\Psi^{(N)}\rangle$, given by

$$\langle \hat{H} \rangle = \frac{\langle \Psi^{(N)} | \hat{H} | \Psi^{(N)} \rangle}{\langle \Psi^{(N)} | \Psi^{(N)} \rangle}. \quad (3.27)$$

If $|\Psi^{(N)}\rangle$ is written in real space as (see (3.26))

$$|\Psi^{(N)}\rangle = \sum_{\nu} f_{\nu} |\nu\rangle \quad (3.28)$$

with ν a configuration $(\{\vec{n}_{i,\uparrow}\}, \{\vec{n}_{j,\downarrow}\})$ and $f_{\nu} = \det[A(\nu)]$, (3.27) becomes

$$\begin{aligned} \langle \hat{H} \rangle &= \sum_{\nu} \frac{\sum_{\mu} f_{\nu} f_{\mu} \langle \mu | \hat{H} | \nu \rangle}{\sum_{\alpha} f_{\alpha}^2} \\ &= \sum_{\nu} \frac{f_{\nu}^2}{\sum_{\alpha} f_{\alpha}^2} \sum_{\mu} \frac{f_{\mu}}{f_{\nu}} \langle \mu | \hat{H} | \nu \rangle \\ &= \sum_{\nu} P_{\nu} \sum_{\mu} \frac{f_{\mu}}{f_{\nu}} \langle \mu | \hat{H} | \nu \rangle. \end{aligned} \quad (3.29)$$

P_{ν} is the probability to find the configuration ν in state $|\Psi^{(N)}\rangle$ and the corresponding distribution is called P . The variational Monte Carlo simulation consists of two stages. First a random walk allows us to generate a set of configurations $\{\nu_i\}$ with

a distribution in agreement with P and then the energy of these configurations is averaged. Therefore the variational energy in state $|\Psi^{(N)}\rangle$ is:

$$\langle \hat{H} \rangle = \lim_{M \rightarrow \infty} \frac{1}{M} \sum_{i=1}^M \left[\sum_{\mu} \frac{f_{\mu}}{f_{\nu_i}} \langle \mu | \hat{H} | \nu_i \rangle \right]. \quad (3.30)$$

The Metropolis algorithm is used to generate a new configuration $|\nu_{i+1}\rangle$, starting from $|\nu_i\rangle$. First, a move is randomly chosen with a uniform probability among all possible moves. A trial configuration ν_t is so defined. $|\nu_t\rangle$ is accepted as new configuration with a probability $W_{\nu t}$, where:

$$W_{\nu t} = \frac{P_t}{P_{\nu}} = \left(\frac{f_t}{f_{\nu}} \right)^2 \quad (3.31)$$

This choice satisfies the “detailed balance” [21], which guarantees that the set of configurations is distributed according to P. A random number r is then chosen with uniform probability in $[0,1]$. If $r > W_{\nu t}$, the configuration does not change ($|\nu_{i+1}\rangle \equiv |\nu_i\rangle$) at this iteration. On the contrary, if $r < W_{\nu t}$, $|\nu_t\rangle$ becomes the new configuration ($|\nu_{i+1}\rangle \equiv |\nu_t\rangle$). The iteration $|\nu_i\rangle \rightarrow |\nu_{i+1}\rangle$ is called a Monte Carlo step.

In the case of the t-J model at moderate doping, the wave function has singly occupied sites and a few empty sites. Therefore, the possible moves are of two types: the flip of two opposite nearest-neighbor spins or the hopping of a spin into an empty site. In this way, all configurations can be generated and no doubly occupied sites are created. The key point in the random walk is the uniformity of the choice of the considered move. To ensure this uniformity, a site of the lattice is randomly chosen along with one of its nearest neighbours. If these sites are occupied by two opposite spins, then these spins are flipped. If one site is empty and the other occupied, the electron is moved to the empty site. In all other cases, the configuration does not change at this Monte Carlo step.

3.3.3 Results

As the quantity $a(\vec{k})$ defined in (3.19) is singular on the diagonal of the first Brillouin zone when $\xi_{\vec{k}} < 0$ and for a d -wave symmetry of the gap parameter, a suitable choice of boundary conditions (like the periodic-antiperiodic boundary conditions) should be used in order to avoid these momenta. An alternative way is to keep the periodic-periodic boundary conditions and to add a small extended s -wave contribution $\delta_{\vec{k}}$ to the d -wave gap parameter. In this case $\Delta_{\vec{k}} \neq 0$ on the diagonal. The pure d -wave behavior is then recovered by taking $\delta_{\vec{k}} \rightarrow 0$. The parameter U appearing in (3.15) must be large as the effective Hamiltonian is only valid in the limit $U \rightarrow \infty$. Here the value originally considered by Gros [22], $U = 16t$, is used.

The results of the Monte Carlo simulation for a 9×9 square lattice with 7 holes ($n \approx 0.91$) and periodic-periodic boundary conditions are given in Figure (3.10).

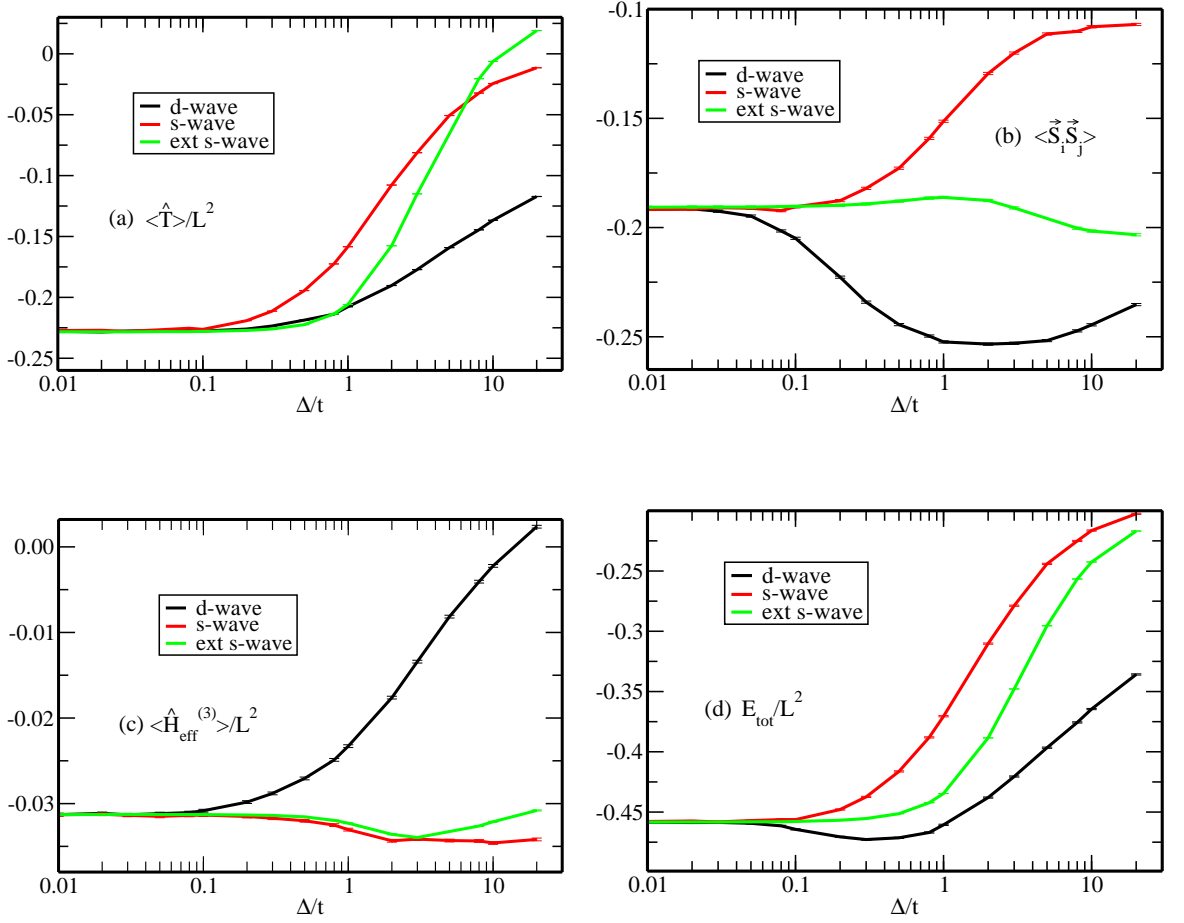


Figure 3.10: Results of the variational Monte Carlo simulation for the $|RVB\rangle$ trial state, for $U = 16t$ and periodic boundary conditions. The density is $n = 74/81 \approx 0.91$. (a): Kinetic energy per site (b): Nearest-neighbor spin-spin correlation (c): “3-site” energy per site (d) Total energy per site.

The total energy shown in part (d) increases monotonically with the gap parameter for both s -wave and extended s -wave symmetry. These symmetries are therefore not favorable to pairing. On the contrary, a finite gap of about $0.3t$ is found in the ground state when d -wave pairs are considered. The energy gain results from antiferromagnetic nearest-neighbor spin correlations, which are enhanced as the d -wave pairing increases (part (b)). The energy gain due to the exchange term of the effective Hamiltonian, is enough to compensate the increase of the kinetic energy (part (a)). Meanwhile, the “3-site” energy given in part (c) is about one order of magnitude smaller than both the kinetic and the Heisenberg terms. Therefore its contribution to the total energy is not relevant.

These VMC calculations have been generalized by Paramakanti [23], who added a next-nearest-neighbor hopping term to the model. Moreover he was able to extend

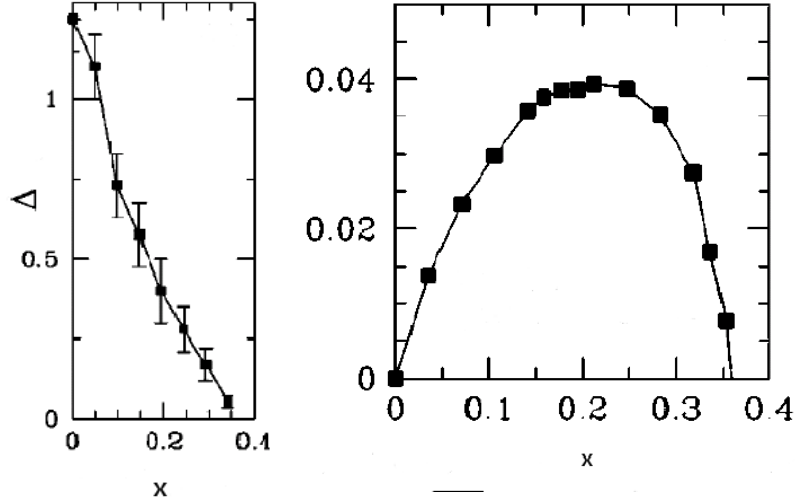


Figure 3.11: (a) Optimal gap parameter as a function of doping for $U = 12t$. (b) Superconducting order parameter. From [23].

the system size considerably. The effective Hamiltonian contains the same three terms as obtained in (3.15), but now the holes can hop to next-nearest-neighbor sites and the “3-site” term also includes next-nearest-neighbor hopping. A “tilted lattice” [23],[24] was used in his calculation in order to avoid the singularities on the diagonal momenta, leading to the rather unusual number of sites $15 \times 15 + 1$.

The main results of Paramekanti are shown in Fig. 3.11. The optimal gap has a maximum at half-filling, decreases almost linearly upon doping and vanishes for a hole concentration $x \approx 0.35$. This behavior leads to the interpretation of the gap parameter as an energy scale corresponding to an incoherent excitation associated with the opening of the pseudogap in the phase diagram of the cuprates (temperature T^*) [23]. In the BCS state, the gap is proportional to the order parameter for the superconducting transition. This is no longer the case after projection, and a finite gap does not mean necessarily a superconducting instability, but rather the presence of preformed pairs in the ground state. Whether these pairs have undergone a Bose-Einstein condensation to give rise to a coherent state is a question that must be raised. The superconducting order parameter Φ is defined by

$$\Phi = |\langle c_{i\sigma}^\dagger c_{i+\tau-\sigma}^\dagger \rangle|, \quad (3.32)$$

where $i + \tau$ is a nearest-neighbor site of i . A non-vanishing order parameter indicates that the fluctuating pairs are condensed and that the ground state is really in a superconducting phase. However, the variational wave function being projected

onto a fixed number of particles, Φ obviously vanishes in this calculation and the long range order has to be checked by computing the long distance behavior of the superconducting correlation function

$$F_{\alpha,\beta}(i-j) = \langle B_{i\alpha}^\dagger B_{j\beta} \rangle \quad (3.33)$$

where

$$B_{i\alpha}^\dagger = \frac{1}{2}(c_{i\uparrow}^\dagger c_{i+\tau_\alpha\downarrow}^\dagger - c_{i\downarrow}^\dagger c_{i+\tau_\alpha\uparrow}^\dagger) \quad (3.34)$$

creates a singlet pair on the nearest-neighbor sites $(i, i + \tau_\alpha)$. This function gives the probability to find a pair located on sites $(i, i + \tau_\alpha)$ when there is a pair on sites $(j, j + \tau_\beta)$. If the distance between i and j increases, the electrons in the vicinity of site i lose the influence of the pair on sites $(j, j + \tau_\beta)$ and the probability factorizes. It is straightforward to see that in the limit $|i - j| \rightarrow \infty$, $F_{\alpha,\beta}(i - j) = \Phi^2$. The advantage is that now $F_{\alpha,\beta}(i - j)$ can be computed for a wave function with a fixed number of particles. The result is given in the right panel of Figure 3.11 as a function of doping. The order parameter forms a dome that vanishes at half-filling and the ground state is indeed superconducting in the range $0 < x < 0.35$. The different doping dependences of the gap and the order parameter indicate that some preformed pairs are not condensed in the underdoped region. In [23], it is suggested that these uncondensed pairs are responsible for the unusual properties of the pseudogap phase.

3.4 Intermediate value of the repulsion U

In the previous sections, we have seen that in both limits $U/t \lesssim 1$ and $U \rightarrow \infty$ the ground state of the two-dimensional Hubbard model has a strong tendency towards a superconducting instability with d -wave symmetry of the order parameter, in a certain density range. However, the effective Coulomb parameter extracted from neutron scattering data [10] indicates that the high- T_c cuprates are not well described by one or the other of these limits. Indeed, the value of $U = 8.8t$ is much too high to be considered as a weak interaction, but on the other hand it is clearly too small to neglect the double occupancy. The cuprates are therefore located in the regime of intermediate coupling, which can be investigated by Monte Carlo calculations.

3.4.1 Quantum Monte Carlo

The knowledge of the partition function $Z = \text{Tr } e^{-\beta \hat{H}}$ of a system described in the grand canonical ensemble by the Hamiltonian \hat{H} allows us to compute the expectation value of an observable \hat{O} , which is given by:

$$\langle \hat{O} \rangle = \frac{1}{Z} \left(\text{Tr } \hat{O} e^{-\beta \hat{H}} \right) \quad (3.35)$$

where β is the inverse temperature $\beta = 1/k_B T$. Quantum Monte Carlo is a powerful technique where the parameter β is discretized in L “time steps” $\Delta\tau$, in order to compute the partition function and the expectation values numerically. For the Hubbard model $\hat{H} = t\hat{T} + U\hat{D}$, the exponential can be written:

$$e^{-\beta\hat{H}} = \left(e^{-\Delta\tau\hat{H}}\right)^L \approx \left(e^{-\Delta\tau t\hat{T}} e^{-\Delta\tau U\hat{D}}\right)^L. \quad (3.36)$$

As the operators \hat{T} and \hat{D} do not commute, the Trotter formula introduces an error of order $(\Delta\tau)^2$. This particular form allows us to make use of a Hubbard-Stratonovich transformation to decouple the operator \hat{D} , which is quartic in the fermionic operators. Such a transformation introduces an auxiliary field Φ and a summation over all possible configurations of this field has to be performed. The advantage is that all the exponentials are now quadratic in the fermionic operators and the fermionic degrees of freedom can be integrated out. A similar procedure for our variational calculation will be detailed in Section 4.3.1 and therefore we just mention here that the contribution to the partition function for a particular field configuration is reduced to a product of determinants, which is taken as a weight for the Monte Carlo simulation [25],[26]. The partition function is finally given by:

$$Z = \sum_{\{\Phi\}} \det\hat{O}_\uparrow \det\hat{O}_\downarrow \quad (3.37)$$

with

$$\hat{O}_\sigma = 1 + B_L^\sigma B_{L-1}^\sigma \cdots B_1^\sigma \quad (3.38)$$

and

$$B_l^\sigma = e^{-\Delta\tau t T} e^{V_l^\sigma} \quad (3.39)$$

T is the matrix representation of the hopping operator and V_l^σ is a matrix depending on the parameters of the problem and the field configuration at time step l .

Half-filled system

At half filling, the product $\det\hat{O}_\uparrow \det\hat{O}_\downarrow$ is positively defined due to the electron-hole symmetry and it therefore corresponds to the probability of a particular field configuration. A standard Monte Carlo simulation (see Section 3.3.3) allows us to carry out the remaining sum over the field configurations and to compute expectation values. Figure 3.12 gives some results computed by Hirsch [26]. The left panel shows the total energy as a function of temperature. Its extrapolation allows one to estimate the ground state energy, assuming a T^2 dependence at low temperatures. For $U = 8t$, the energy $-0.48(5)$ is obtained with a rather large uncertainty due to the extrapolation. At finite temperatures, long-range antiferromagnetic order cannot

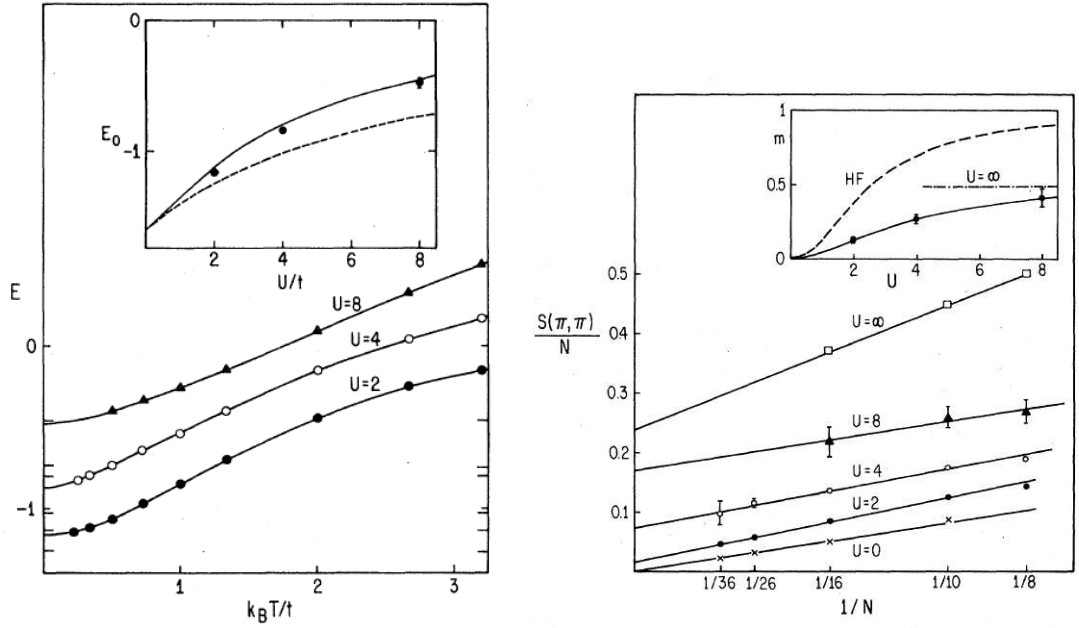


Figure 3.12: Monte Carlo results for the 2D Hubbard model at half filling. Left: Total energy per site as a function of temperature for various values of the repulsion parameter U and a lattice size 6×6 . Periodic-periodic boundary conditions are used. The inset gives the ground state energy obtained from the extrapolation of the energy, assuming a T^2 dependence at low temperatures. Right: Structure factor at (π, π) as a function of the inverse lattice size, for $\beta = 0.75\sqrt{N}$. The inset gives the staggered magnetization extracted from the value of $S(\pi, \pi)/N$ in the thermodynamic limit. From [26].

occur in two dimensions as it would break a continuous symmetry. Nevertheless, an estimate of the staggered magnetization M at zero temperature, defined by:

$$M = \frac{1}{N} \sum_i (-1)^{\vec{r}_i} \langle n_{i\uparrow} - n_{i\downarrow} \rangle \quad (3.40)$$

can be obtained from the magnetic structure factor:

$$S(\vec{q}) = \frac{1}{N} \sum_{i,j} e^{i\vec{q} \cdot (\vec{r}_i - \vec{r}_j)} \langle (n_{i\uparrow} - n_{i\downarrow})(n_{j\uparrow} - n_{j\downarrow}) \rangle \quad (3.41)$$

under the condition that the thermal coherence length is of the order of the linear lattice size. Indeed, at zero temperature the structure factor at (π, π) behaves as $S(\pi, \pi) \sim NM^2$. The right panel of Figure 3.12 shows the structure factor at (π, π) as a function of the inverse lattice size, as well as the extracted magnetization for various values of U . The linear dependence of $S(\pi, \pi)/N$ indicates that the temperature is low enough to mimic the zero temperature behavior. For $U = 8t$, the staggered magnetization is $M = 0.42(1)$. However, we note that this value should be taken as a lower bound for the zero temperature magnetization as calculations are realized at a finite temperature.

At half-filling, an antiferromagnetic ground state for the Hubbard model is therefore obtained from quantum Monte Carlo calculations.

Doped system

The situation is much more complicated when holes are introduced into the system. Indeed, the product $\det \hat{O}_\uparrow \det \hat{O}_\downarrow$ is no longer positively defined away from half filling and it turns out that a sign problem (see Section 4.4.2) occurs in the most interesting range of moderate doping, which becomes severe at low temperatures [27],[28]. Results for correlation functions or susceptibilities at low temperatures are therefore altered by this sign problem. Nevertheless, interesting results are found at rather high temperatures by considering the irreducible vertex in the singlet channel Γ_{Is} [29]. This vertex can be determined from the knowledge of the single-particle $G_\sigma(x_2, x_1) = -i \langle T c_\sigma(x_2) c_\sigma^\dagger(x_1) \rangle$ and two-particle $G_2(x_4, x_3, x_2, x_1) = -\langle T c_\uparrow(x_4) c_\downarrow(x_3) c_\downarrow^\dagger(x_2) c_\uparrow^\dagger(x_1) \rangle$ Green's functions, which can be computed in momentum-frequency space using quantum Monte Carlo simulations. In these formulae, T is the “imaginary time” ordering operator. The reducible particle-particle vertex Γ is first extracted from the relation between Γ and the Green's functions, and then the irreducible particle-particle vertex Γ_{Is} is obtained by solving the t-matrix equation. Figure 3.13 shows the momentum (left) and frequency (right) dependence of $\Gamma_{Is}(\vec{q}, \omega_n)$ for various temperatures.

$\Gamma_{Is}(\vec{q}, \omega_n)$ is largest for $\omega_n = 0$ and $\vec{q} = (\pi, \pi)$, and it is enhanced as the temperature is lowered. It is interesting to note that this behavior is similar, even at

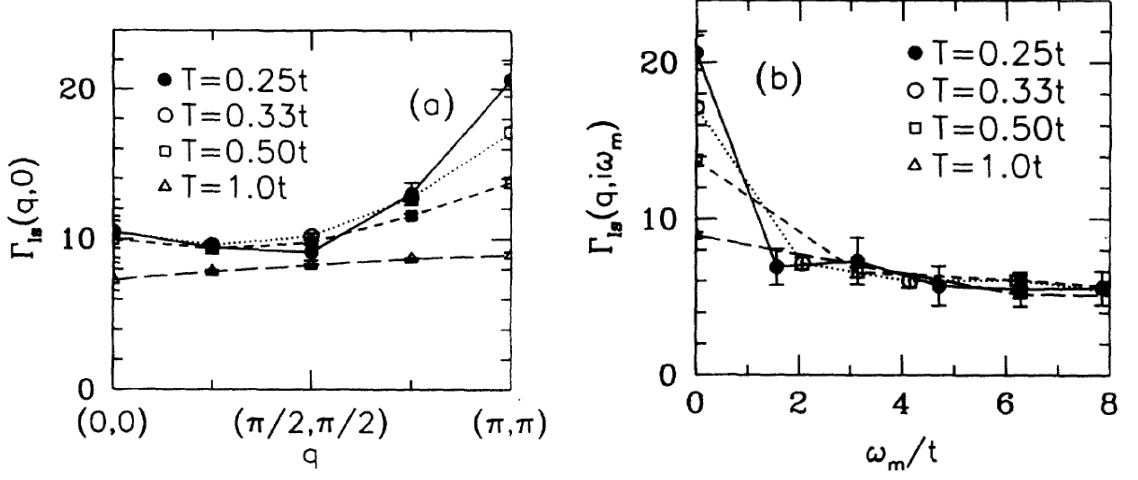


Figure 3.13: Irreducible vertex in the singlet channel for various temperatures. Left: as a function of the momentum transferred during the scattering, for an energy-transfer $\omega_m = 0$. Right: as a function of the energy-transfer for a momentum-transfer $\vec{q} = (\pi, \pi)$. The calculations are carried out for an 8×8 lattice with periodic boundary conditions, with density $n = 0.87$ and $U = 4t$. From [29].

a quantitative level, to that of a single-spin-fluctuation exchange interaction [29]. This indicates that the formation of Cooper pairs in the Hubbard model could originate from an effective interaction mediated by the exchange of antiferromagnetic spin fluctuations. The real space interaction can be computed by taking the Fourier transform of the irreducible interaction Γ_{Is} . Figure 3.14 gives a representation of this real space interaction. It is clear that the renormalized Coulomb repulsion is still strongly repulsive on-site, but an attractive interaction is found for the nearest-neighbor or third-neighbor sites. As predicted by the Kohn-Luttinger theorem, the system can take advantage of a particular symmetry of the pairing correlations (like the d-wave symmetry) to create Cooper pairs, and in so doing, to reduce its total energy.

3.4.2 Cluster Dynamical Mean Field Theory

For the doped system, an alternative to the finite lattice quantum Monte Carlo described in the previous section is to consider a small cluster embedded in a host environment representing the infinite lattice. The cluster degrees of freedom are taken into account explicitly, while the remaining degrees of freedom are treated at the (dynamical) mean field level. There are various ways to implement such a

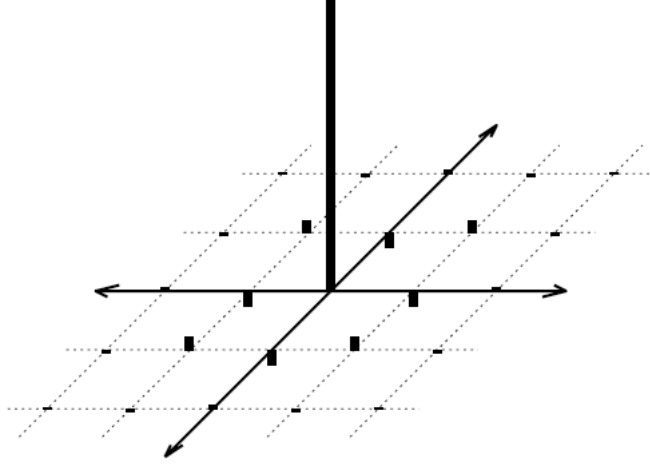


Figure 3.14: Graphical representation of the real space effective interaction deduced from the Fourier transform of the irreducible vertex in the singlet channel.

method. Here we restrict ourselves to the Dynamical Cluster Approximation. The infinite lattice is first divided into clusters of size $N_c \times N_c$. Correspondingly, the First Brillouin Zone is subdivided into $N_c \times N_c$ blocks, defined by the wave vector \vec{K} (see Fig. 3.15). The wave vectors \vec{k} inside a block corresponds to the cluster coordinates \vec{x} in real space. The hopping amplitude t and the self-energy Σ of the infinite lattice can then be split into intracluster and intercluster components:

$$\begin{aligned} t &= t_c + \delta t \\ \Sigma &= \Sigma_c + \delta \Sigma \end{aligned} \quad (3.42)$$

Hence t_c is the hopping between cluster sites and δt corresponds to hopping between sites in different clusters. The central approximation consists of neglecting $\delta \Sigma$. The self-energy is therefore truncated to the cluster degrees of freedom, $\Sigma \approx \Sigma_c$. In the Dynamical Cluster Approximation, the infinite lattice Green's function G is also restricted to the cluster by averaging the various contributions in each block of the First Brillouin Zone. This leads to the coarse-grained Green's function:

$$\begin{aligned} \bar{G}(\vec{K}, \omega) &= \frac{N_c}{N} \sum_{\vec{k}} G(\vec{K} + \vec{k}, \omega) \\ &= \frac{N_c}{N} \sum_{\vec{k}} [G_0^{-1}(\vec{K} + \vec{k}, \omega) - \Sigma_c(\vec{K}, \omega)]^{-1} \end{aligned} \quad (3.43)$$

with $G_0^{-1}(\vec{K} + \vec{k}, \omega) = i\omega - \epsilon_{\vec{K} + \vec{k}} + \mu$.

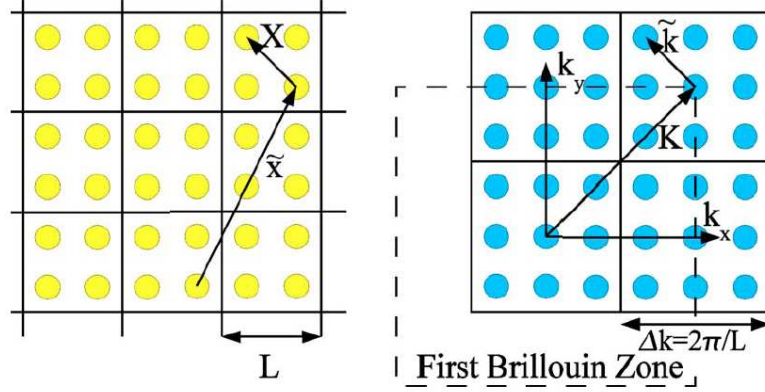


Figure 3.15: Left-hand side: The lattice is divided into clusters of size $N_c \times N_c$. The position of the clusters is given by the vector $\vec{\tilde{x}}$, whereas the vector \vec{X} gives the site positions in each cluster. Right-hand side: The First Brillouin Zone is subdivided into $N_c \times N_c$ cells numbered by the vector \vec{K} . The vector \vec{k} corresponds to the cluster positions.

As Σ_c is restricted to the cluster degrees of freedom, it can be seen as the self-energy of an effective cluster model, defined by the Hamiltonian:

$$\hat{H}_c = \hat{H}_{0c} + \hat{H}_{Ic}. \quad (3.44)$$

Only the fermionic operators of the cluster are represented by \hat{H}_{0c} and \hat{H}_{Ic} , which describe respectively a single-particle term including the hopping between the cluster and the host and a two-particle term related to the interaction of the original lattice model. The cluster Green's function G_c is written formally as a noninteracting part \mathcal{G} for \hat{H}_{0c} and a self energy correction Σ_c when \hat{H}_{Ic} is taken into account:

$$G_c = [\mathcal{G}^{-1} - \Sigma_c]^{-1}. \quad (3.45)$$

Now the effective cluster model is defined by identifying the cluster Green's function to the coarse-grained Green's function of the original model, $G_c \equiv \bar{G}$. By using a “Cluster Solver”, which allows one to obtain the cluster Green's function G_c from the knowledge of \mathcal{G} and of the interaction, the cluster self-energy can be computed iteratively. An initial guess for Σ_c is first used to compute the coarse-grained Green's function from Eq. (3.43). \mathcal{G} is then obtained from its definition (3.45) using $G_c = \bar{G}$. The “Cluster Solver” returns the Green's function for the effective cluster model and finally a new estimate of the cluster self-energy is calculated from (3.45). This procedure (see Fig. 3.16) is repeated until G_c has converged towards \bar{G} . The formalism has been generalized to two-particle correlation functions, in particular to magnetic and pairing susceptibilities [30],[31].

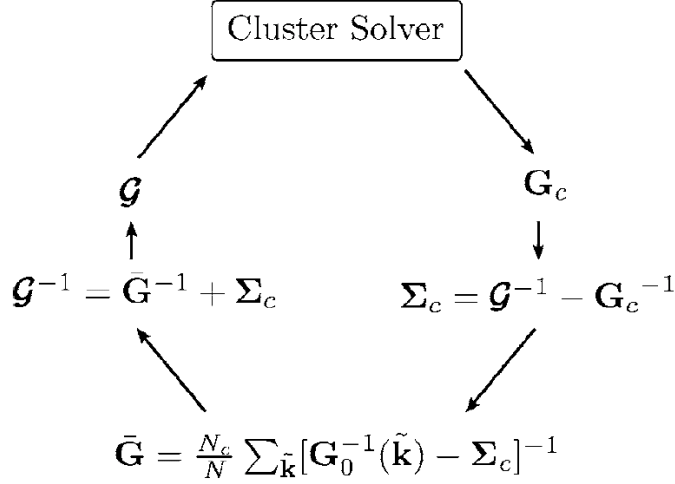


Figure 3.16: Iterative procedure of the Cluster Dynamical Mean Field Theory, leading to the value of the self-energy of the cluster embedded in the host environment (see the text).

The complexity of the problem has therefore been reduced to the diagonalization of the Hamiltonian (3.44), which describes the cluster degrees of freedom and their coupling with the host. This Hamiltonian can be seen as the extension of the single-impurity Anderson model to a cluster. Various techniques have been developed to solve this effective model, corresponding to different “Cluster Solvers”. One possibility is to use an adaptation (see [32],[31]) of the quantum Monte Carlo simulation described in the previous section. Figure 3.17 shows the inverse antiferromagnetic (left-hand side) and the pairing (right-hand side) susceptibilities as functions of the temperature, computed in the paramagnetic phase of the two-dimensional Hubbard model. At half-filling and for a 4×4 cluster, the inverse antiferromagnetic susceptibility vanishes at the temperature $T_N \approx 0.041$, indicating a transition to an antiferromagnetic state. When the hole concentration increases, the Néel temperature T_N decreases and the inverse susceptibility does not cross zero anymore when $\delta > 0.05$. Results for the usual Dynamical Mean Field Theory, where the cluster is reduced to a single site, show that the antiferromagnetism is strongly suppressed when non-local fluctuations are taken into account. This is in agreement with the Mermin-Wagner theorem which states that the Néel temperature has to vanish for a two-dimensional system in the thermodynamic limit. At the right-hand side of Fig. 3.17, a divergence of the pair field susceptibility is observed only for d -wave symmetry when $\delta = 0.05$. In this case, the superconducting transition occurs at $T_c \approx 0.021$. No sign of a pairing instability is found when the cluster is reduced to a single site (DMFT), proving the important role of the non-local correlations. The phase diagram obtained in this way for the two-dimensional Hubbard model is shown in Fig. 3.18. As the transitions are

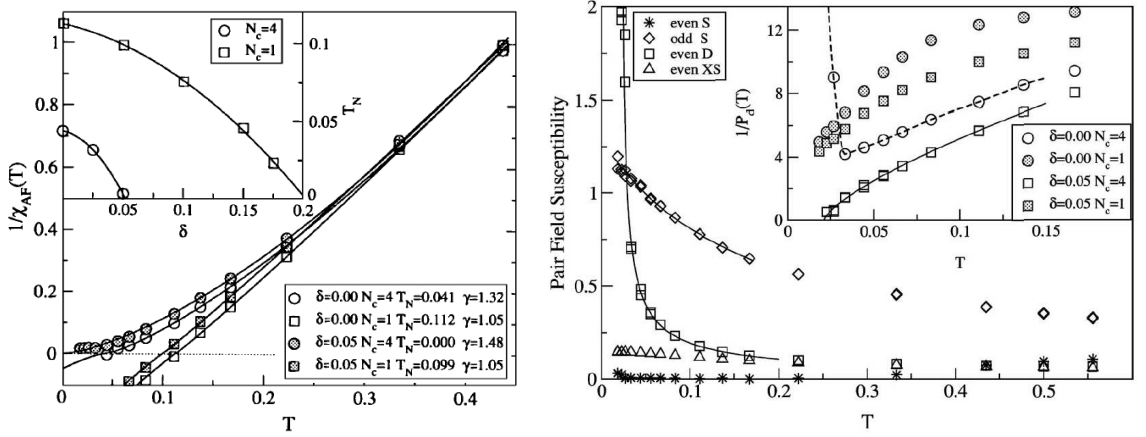


Figure 3.17: Left: Inverse antiferromagnetic susceptibility as a function of temperature for $U = 8t$, dopings $\delta = 0.00, 0.05$ and cluster sizes $N_c = 1, 4$. The lines are fits to $b(t - T_N)^\gamma$. Inset: Néel temperature as a function of doping for $N_c = 1, 4$. Right: Pair field susceptibility as a function of temperature for various symmetries, $U = 8t$, $\delta = 0.05$ and $N_c = 4$. Inset: Inverse pair field susceptibility for $\delta = 0.00, 0.05$ and $N_c = 1, 4$. From [33].

obtained independently from the divergence of the susceptibilities, the superposition of an antiferromagnetic and a superconducting phase does not imply the coexistence of these phases. A third line (T^*) in the phase diagram is associated with the opening of a pseudogap. The temperature T^* for the crossover is defined by the peak in the bulk ($\vec{k} = 0$) magnetic susceptibility. For a temperature $T < T^*$, a gap is observed in the single-particle density of states.

Finally, the Cluster Dynamical Mean Field Theory can be generalized to described the superconducting phase [34],[31]. Using the Nambu notation, the self-energy takes the form

$$\Sigma(\vec{k}, \omega) = \begin{pmatrix} \Sigma_\uparrow(\vec{k}, \omega) & \Sigma^{an}(\vec{k}, \omega) \\ \Sigma^{an}(\vec{k}, \omega) & -\Sigma_\downarrow(-\vec{k}, -\omega) \end{pmatrix} \quad (3.46)$$

where $\Sigma^{an}(\vec{k}, \omega)$ is the anomalous component of $\Sigma(\vec{k}, \omega)$. The corresponding Green's function is

$$G(\vec{k}, \omega) = \begin{pmatrix} G_\uparrow(\vec{k}, \omega) & F(\vec{k}, \omega) \\ F^\dagger(\vec{k}, \omega) & -G_\downarrow(-\vec{k}, -\omega) \end{pmatrix} \quad (3.47)$$

with $F(\vec{k}, 0) = \langle c_{\vec{k}\uparrow} c_{-\vec{k}\downarrow} \rangle$ the superconducting order parameter. The value of $F(\vec{k}, 0)$ as a function of doping obtained after the convergence of the CDMFT procedure is given in Fig. 3.19. The order parameter forms a dome with a maximal value occurring at the same doping as the maximum T_c .

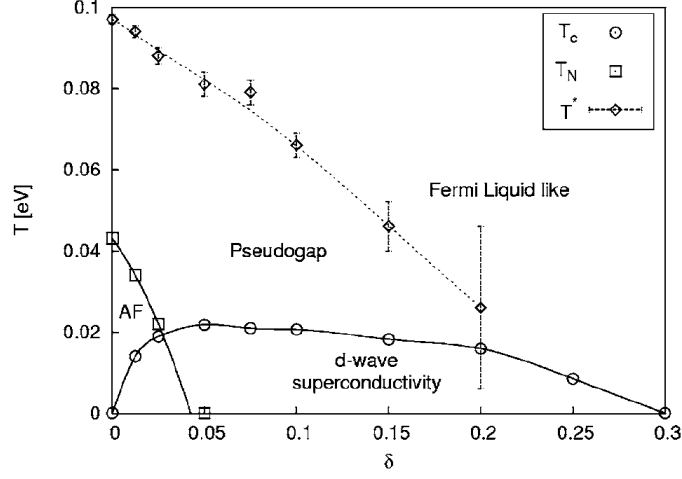


Figure 3.18: Phase diagram of the two-dimensional Hubbard model with $U = 8t$ obtained for a 4×4 cluster. From [33].

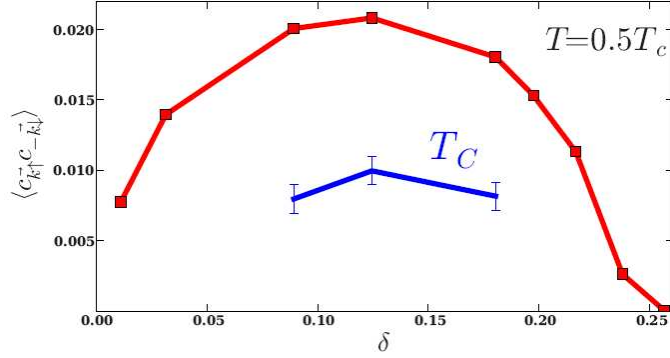


Figure 3.19: Superconducting order parameter of the two-dimensional Hubbard model with $U = 12t$ as a function of the doping, computed by Cluster Dynamical Mean Field Theory with a 2×2 cluster at a temperature corresponding to $0.5T_c$. The critical temperature is also shown for comparison. From [34].

3.4.3 Variational Monte Carlo: The Gutzwiller ansatz

The quantum Monte Carlo method is limited to rather high temperatures at finite doping due to the occurrence of the sign problem. An alternative approach is provided by variational calculations, which deal with ground state properties. The variational Monte Carlo method introduced in Section 3.3.1 for the reduced Hilbert space without double occupancy can be readily adapted to include configurations with doubly occupied sites. We consider a superconducting trial state with d -wave symmetry. In the wave function (3.17), the projector P_G is replaced by the Gutzwiller operator $e^{-g\hat{D}}$ which suppresses only partially the double occupancy. It is written:

$$|\Psi_G\rangle = e^{-g\hat{D}}|dBCS\rangle = e^{-g\sum_i n_{i\uparrow}n_{i\downarrow}}|dBCS\rangle. \quad (3.48)$$

The variational parameter g allows us to tune the double occupancy, the state (3.17) being recovered in the limit $g \rightarrow \infty$. The notation $|dBCS\rangle$ means that the BCS state has a gap parameter with d -wave symmetry. As for the t-J model, this state is projected onto a fixed number of particles, but now all configurations are kept. The operator \hat{D} is diagonal in real space and therefore just adds a weight to each configuration $\{\vec{n}_{i\uparrow}\}\{\vec{n}_{j\downarrow}\}$ depending on the number N_D of doubly occupied sites. Eq. (3.48) takes the form

$$|\Psi_G^{(N)}\rangle = \sum_{\{\vec{n}_{i\uparrow}\},\{\vec{n}_{j\downarrow}\}} e^{-gN_D(\{\vec{n}_{i\uparrow}\},\{\vec{n}_{j\downarrow}\})} \det[A(\{\vec{n}_{i\uparrow}\},\{\vec{n}_{j\downarrow}\})] |\{\vec{n}_{i\uparrow}\},\{\vec{n}_{j\downarrow}\}\rangle. \quad (3.49)$$

A Monte Carlo simulation can be performed to get the energy of the variational state $|\Psi_G^{(N)}\rangle$. The Metropolis algorithm described in Section 3.3.2 is first used to generate a set of configurations. The passage between subsequent configurations is carried out by moving a randomly chosen electron to a nearest-neighbor site which is also randomly selected. The variational energy is then computed by averaging the kinetic and potential energies of the Hubbard Hamiltonian over this set of configurations.

The projection of the variational wave function onto a fixed number of particles restricts the choice of the allowed densities. When the number of particles is such that the states at the Fermi surface are only partially filled, the variational ground state is highly degenerate and this leads to a problem of convergence in the Monte Carlo simulation. Therefore the density has to correspond to a last shell which is completely filled.

The total energy is given in Fig. 3.20 as a function of the gap parameter for different lattice sizes. Due to the periodic-antiperiodic boundary conditions, the half-filled system corresponds to a filled shell for all lattice sizes. For other densities the closed-shell condition may be satisfied for one lattice size, but not for another one. Thus the density $n = 0.8125$ corresponds to a closed shell for both 8×8 and 16×16 lattices, but not for a 12×12 lattice, where the slightly modified value of $n = 0.8056$

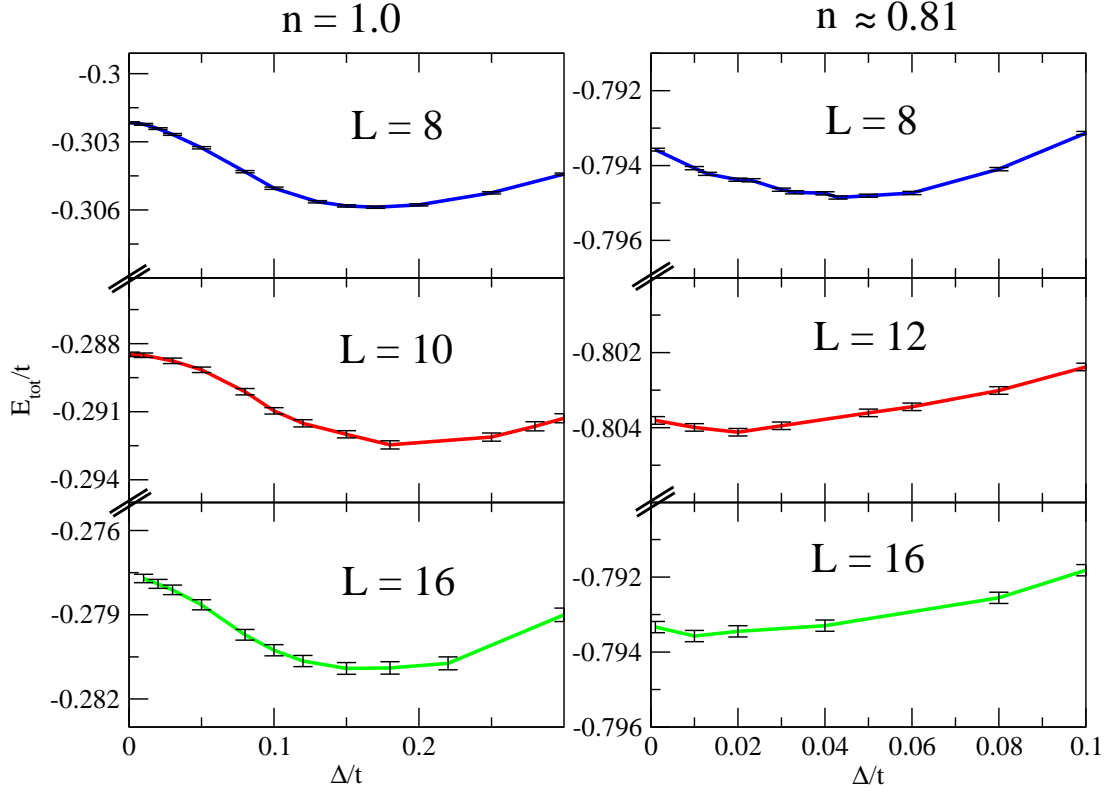


Figure 3.20: Variational energy as a function of the gap parameter for various lattice sizes, a repulsion $U = 8t$ and periodic-antiperiodic boundary conditions. The left part corresponds to a density $n = 1$, whereas the right part gives the behavior for $n \approx 0.81$.

can be used instead. Fig. 3.20 shows that the gap is more or less size independent for $n = 1$, but not for $n \approx 0.81$ where it decreases as the system size increases. Fig. 3.21 gives the extrapolation of the value of the optimal gap parameter in the thermodynamic limit. A value of $\Delta_{\infty} \approx 0.16t$ is found at half-filling, while the gap vanishes for $n \approx 0.81$.

In the definition of the BCS state, the chemical potential μ is used in principle to fix the average density of electrons. However, no constraint is imposed on this parameter when the BCS state is projected onto a fixed number of particles. Therefore μ is no longer a true chemical potential and it can either be fixed (like in Fig. 3.20), or used as a variational parameter to improve the ground state. However, it turns out that μ has almost no influence on the results for the gap parameter.

The optimal gap as a function of doping x is given in Fig. 3.22. The gap is maximal at half-filling and decreases monotonically when the doping x increases.

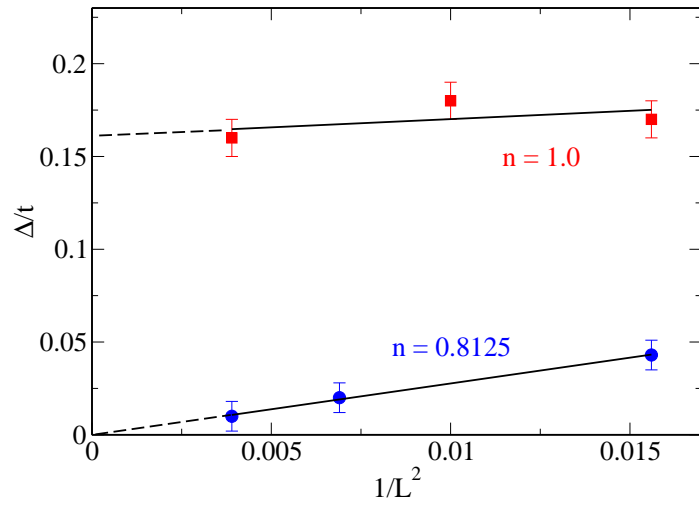


Figure 3.21: Extrapolation for the value of the gap parameter at the thermodynamic limit. The gap converges towards a finite value $\Delta \approx 0.16t$ at half-filling, whereas it vanishes for $n \approx 0.81$

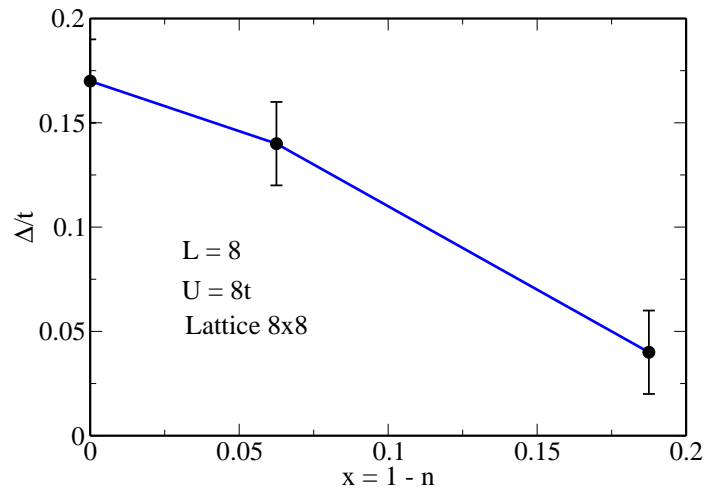


Figure 3.22: Optimal gap parameter as a function of the hole concentration x .

n	μ	g	E/t	$\langle \hat{D} \rangle / L^2$	$\langle \hat{D} \rangle / D_{FS}$
0.8125	-0.51(1)	1.16(2)	-0.795(1)	0.0444(1)	27
0.9375	-0.28(1)	1.31(2)	-0.510(1)	0.0639(1)	29
1.0	0.00(1)	1.38(2)	-0.306(1)	0.0808(1)	32

Table 3.1: “Chemical potential”, parameter g , total energy per site and number of doubly occupied sites (per site) for different densities on a 8×8 lattice with $U = 8t$. The last column gives the proportion of doubly occupied sites in the variational ground state with respect to the filled Fermi sea (in percent).

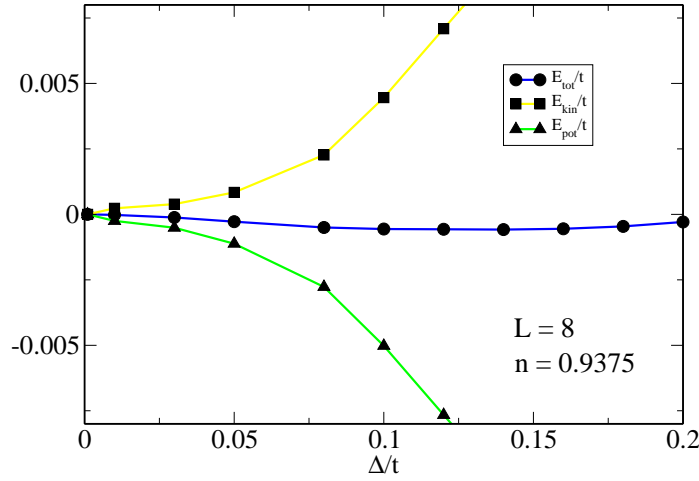


Figure 3.23: Total, kinetic and potential energies per site as functions of the gap parameter on an 8×8 lattice for the density $n = 0.9375$. For each curve $E(\Delta = 0)$ has been subtracted. The relative statistical error is smaller than the symbol size.

This dependence is very similar to the behavior of the gap parameter in the limit where $U \rightarrow \infty$ (see Section 3.3.3), even though the number of doubly occupied sites is far from being negligible for $U = 8t$. Indeed, the variational ground state has almost 30% of the double occupancy of the filled Fermi sea, as can be seen in Table 3.1.

In Fig. 3.23 the kinetic, potential and total energies are plotted as functions of the gap parameter for a density $n = 0.9375$ (60 electrons on 8×8 sites corresponding to a filled shell) and for $U = 8t$. The kinetic energy increases monotonically with the gap parameter, while the potential energy decreases. The total energy passes through a minimum at $\Delta \approx 0.14t$, which means that the ground state is stabilized by the formation of pairs. Here the behavior is not qualitatively different from the BCS behaviour (mean-field level) where the condensation energy $E_{cond} = E_{tot}(0) - E_{tot}(\Delta)$ is entirely due to a gain in the potential energy.

But how good is the Gutzwiller ansatz? The estimates for the energy of the antiferromagnetic ground state of the Hubbard model at half-filling obtained by variational Monte Carlo (see Section 4.3.2), quantum Monte Carlo [26] or other techniques [35] are in the range $-0.48t$ to $-0.52t$ for $U = 8t$. Therefore our value of $-0.306(1)t$ indicates that at least for $n = 1$ the Gutzwiller ansatz does not provide a good estimate of the ground state. Actually, improvements of the variational wave function will show that this remains true at finite doping.

3.4.4 Improving the Gutzwiller ansatz

There are in principle many options for improving the variational ansatz (3.48). Here we mention two modifications proposed by other groups and postpone our own version to Chapter 4.

Inclusion of antiferromagnetism

A first improvement has been proposed by Giamarchi and Lhuillier [36] who admitted the possibility of antiferromagnetic order. They used the wave function

$$|\Psi_{Gia}\rangle = e^{-g\hat{D}} P_N |\Psi_0\rangle = e^{-g\hat{D}} P_N \prod_{\vec{k}} (u_{\vec{k}} + v_{\vec{k}} d_{\vec{k}\uparrow}^\dagger d_{-\vec{k}\downarrow}^\dagger) |0\rangle \quad (3.50)$$

where the d^\dagger results from the Bogoliubov transformation (see Section 4.3):

$$\begin{aligned} d_{\vec{k}\sigma}^\dagger &= \alpha_{\vec{k}} c_{\vec{k}\sigma}^\dagger + \sigma \beta_{\vec{k}} c_{\vec{k}+\vec{K}\sigma}^\dagger, \\ d_{\vec{k}+\vec{K}\sigma}^\dagger &= -\sigma \beta_{\vec{k}} c_{\vec{k}\sigma}^\dagger + \alpha_{\vec{k}} c_{\vec{k}+\vec{K}\sigma}^\dagger. \end{aligned} \quad (3.51)$$

Here $\vec{K} = (\pi, \pi)$ is the perfect nesting vector and \vec{k} is restricted to half of the Brillouin zone where $\epsilon_{\vec{k}} < 0$. $\alpha_{\vec{k}}$ and $\beta_{\vec{k}}$ are chosen in such way that the new fermions d^\dagger diagonalize the antiferromagnetic mean-field Hamiltonian:

$$\alpha_{\vec{k}} = \frac{1}{\sqrt{2}} \left(1 - \frac{\epsilon_{\vec{k}}}{\sqrt{\epsilon_{\vec{k}}^2 + D^2}} \right)^{1/2} \quad \text{and} \quad \beta_{\vec{k}} = \frac{1}{\sqrt{2}} \left(1 + \frac{\epsilon_{\vec{k}}}{\sqrt{\epsilon_{\vec{k}}^2 + D^2}} \right)^{1/2} \quad (3.52)$$

where D is the antiferromagnetic gap parameter. In other words, superconductivity arises here from the pairing of two quasiparticles of the antiferromagnetic phase.

The optimal parameters resulting from the minimization of the variational energy computed by a Monte Carlo simulation are reported in Table 3.2. Clearly the presence of a strong antiferromagnetic instability at half-filling is unfavorable for pairing, which has a maximum for a density of $n \approx 0.94$. The size dependence (see Fig. 3.24) of

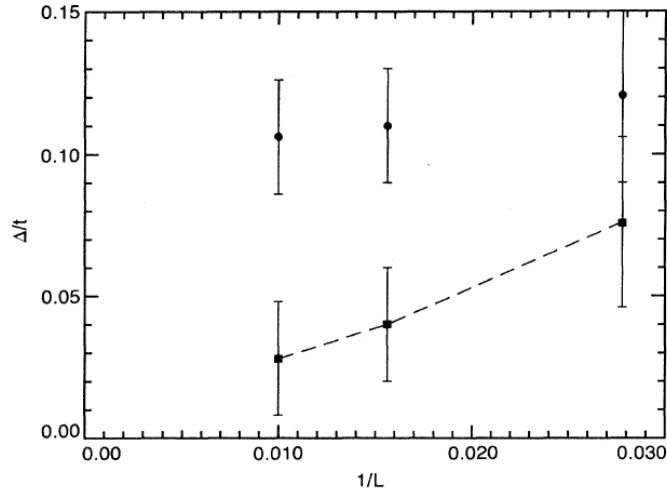


Figure 3.24: Extrapolation for the value of the superconducting gap parameter in the thermodynamic limit. Due to the antiferromagnetic instability, the gap is very small for $n = 1$ (squares). On the contrary, for $n \approx 0.9$ (circles) the gap is rather large. From [36].

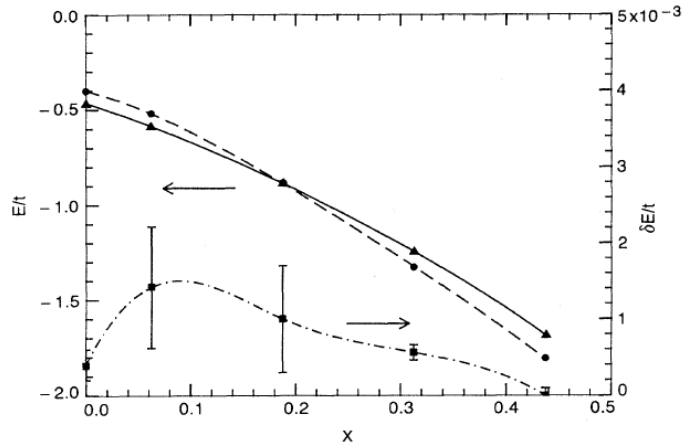


Figure 3.25: Total energy per particle as a function of the doping for an 8×8 lattice at $U = 10t$ (circles) and corresponding condensation energy (squares). The dashed line shows the total energy per particle for the $t - J$ model at $J = 0.4t$. From [36].

n	μ	g	D	Δ
1.0	-0.00(2)	0.80(3)	1.55(4)	0.04(2)
0.9375	-0.19(3)	1.08(3)	0.80(5)	0.11(2)
0.8125	-0.55(6)	1.39(12)	0.05(3)	0.05(2)
0.6875	-0.69(5)	1.24(7)	0.00(3)	0.02(1)
0.5625	-0.87(9)	1.08(6)	0.00(3)	0.00(3)

Table 3.2: Optimal parameters obtained for different densities with the wave function $|\Psi_{Gia}\rangle$ on an 8×8 lattice with $U = 10t$. The boundary conditions are periodic in one direction and antiperiodic in the other direction. From [36].

the parameter Δ shows that the pairing is strong at moderate doping but almost disappears at half-filling. This is exactly the opposite of what has been found with the (simple) Gutzwiller ansatz. The energy of the variational ground state is given in Fig. 3.25 as a function of the density. The comparison of this energy with the variational energy obtained with the Gutzwiller ansatz (see Table 3.3) shows that, as expected, antiferromagnetism is favored at and close to half-filling. However the antiferromagnetic order disappears rapidly with doping and therefore the energy is almost unchanged for $n \lesssim 0.8$.

Addition of correlations between empty and doubly occupied sites

Another way to improve the trial state is to consider, besides the Gutzwiller operator, a second operator adding correlations between empty and doubly occupied sites. The wave function investigated by Yokoyama and coworkers [37] is

$$|\Psi_Y\rangle = P_Q P_G P_N |\Psi_0\rangle \quad (3.53)$$

where

$$P_Q = \prod_i (1 - \nu Q_i) \quad \text{with} \quad Q_i = d_i \prod_{\tau} (1 - e_{i+\tau}) . \quad (3.54)$$

Here $d_i = n_{i\uparrow}n_{i\downarrow}$, $e_i = (1 - n_{i\uparrow})(1 - n_{i\downarrow})$ and τ is a nearest-neighbor site of the site i . $|\Psi_0\rangle$ is a mean-field ground state with either a d -wave superconducting or an antiferromagnetic gap parameter. The effect of the operator P_Q is sketched in Figure 3.26. Such a choice is motivated by the large U expansion described in Section 3.3.3. In the limit $U \rightarrow \infty$, a configuration like that in Figure 3.26(c) appears as a virtual state (or intermediate state) of fourth order in the large U expansion and is therefore expected to be less favorable than a virtual configuration of second order (Figure 3.26(b)). For a finite U , this effect is translated to a “binding” energy occurring between the holes and the doubly occupied sites, taken into account by including the operator P_Q .

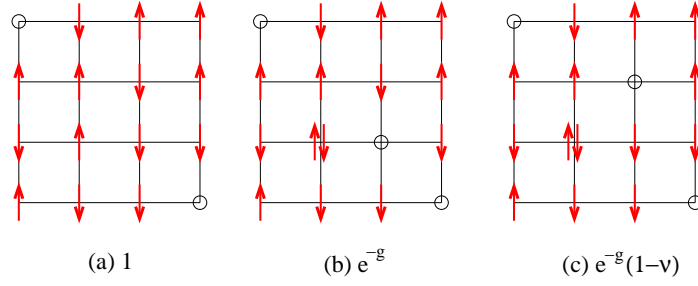


Figure 3.26: Effects of the different projectors in the wave function (3.53). (a) A configuration without doubly occupied site has a relative weight 1 introduced by the projectors. (b) A configuration with a doubly occupied site which is nearest neighbor of at least one empty site is only penalised by the factor e^{-g} . (c) A configuration with a doubly occupied site which does not have an empty site as nearest neighbour is considered as arising from higher order terms in the large U expansion and is penalised by $e^{-g}(1 - \nu)$.

n	Ψ_{Gia}	Ψ_Y
1.0	62(1)	45(1)
0.9600	-	15(1)
0.9375	19(3)	-
0.8800	-	4(1)
0.8125	1(1)	-
0.8000	-	2(1)

Table 3.3: Improvements obtained with the wave functions Ψ_{Gia} and Ψ_Y with respect to the Gutzwiller ansatz (in percent of the Gutzwiller energy). For Ψ_Y a state with a superconducting order parameter has been chosen.

Again, a Monte Carlo simulation allows one to compute the variational energy. The optimisation of the parameters g , ν , Δ and μ gives the ground state energy reported in Fig. 3.27(left) as a function of the parameter U/t , for normal, antiferromagnetic and superconducting states. In Fig. 3.27(right), the condensation energy is plotted as a function of U/t for various densities.

Qualitatively, the results obtained with the wave function $|\Psi_Y\rangle$ for a pairing instability and $U = 8t$ do not change much when compared with the Gutzwiller ansatz results. More accurately, a pairing is found to be favorable for densities in the range $1 \geq n \geq 0.8$. However for a lattice 10×10 at a density $n = 0.8$, the pairing is already very weak, as pointed out by the tiny condensation energy (Figure 3.27(right)), and it is questionable whether the gap will persist in the thermodynamic limit.

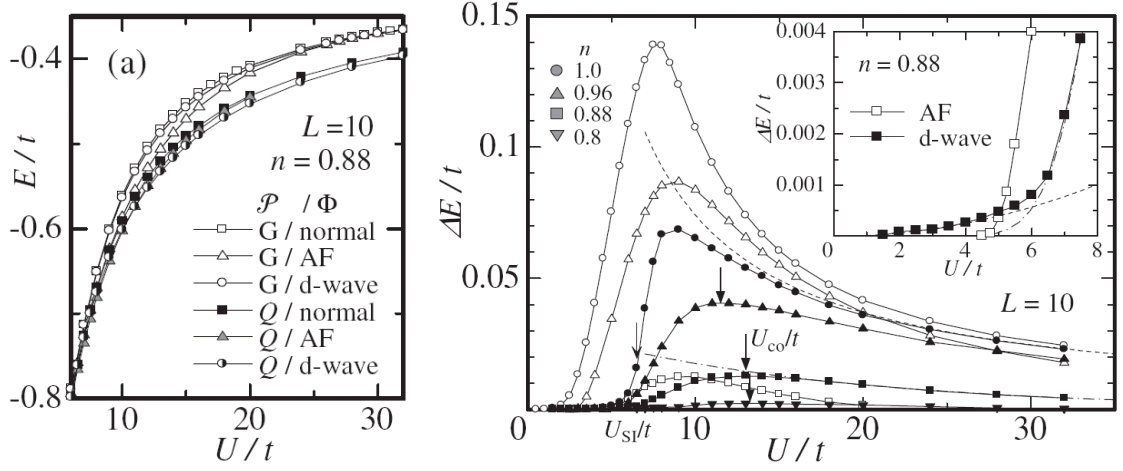


Figure 3.27: Left: Total energy per site as a function of the repulsion U , on a 10×10 square lattice and for $n = 0.88$. Results are given for the Gutzwiller ansatz (G) and for the wave function (3.53) (Q) in the normal, antiferromagnetic and superconducting states. Right: Condensation energy as a function of the repulsion U for antiferromagnetic (open symbols) and superconducting states (closed symbols) and for various densities. From [37].

Table 3.3 summarizes the improvements obtained with the wave functions Ψ_{Gia} and Ψ_Y as compared to the (simple) Gutzwiller ansatz. As already discussed, Ψ_{Gia} leads to a large energy gain at half-filling. Remarkably the second projector of Ψ_Y is nearly as effective as antiferromagnetism although Ψ_Y describes a superconducting instability. With an antiferromagnetic order parameter, Ψ_Y reduces the ground state energy by 64% and is therefore better than Ψ_{Gia} at half-filling. However, a superconducting order parameter becomes favorable when the density is reduced (for $U \lesssim 5t$ and $U \gtrsim 12t$ when $n = 0.88$ and for all values of U when $n \lesssim 0.8$). These variational results underline the importance both of the right choice of symmetry breaking and of additional correlations. We will see in the next chapter that there is still room for improvement.

Chapter 4

A refined variational wave function

The Gutzwiller ansatz only optimizes the Coulomb term of the Hubbard model, without taking care of the kinetic term. However the exchange processes, which could stabilize further the ground state, are driven by this latter term and it seems important to take advantage of the large degeneracy of the states with a small number of doubly occupied sites to favor the states with a low kinetic energy. An alternative way to improve the variational ground state is therefore to consider the refined wave function:

$$|\Psi_{GB}\rangle = e^{-h\hat{T}} e^{-g\hat{D}} |\Psi_0\rangle . \quad (4.1)$$

Here $|\Psi_0\rangle$ is a mean-field ground state with either a (d -wave) superconducting or an antiferromagnetic order parameter. The operator $e^{-g\hat{D}}$ partially suppresses double occupancy for $g > 0$, while $e^{-h\hat{T}}$ promotes both hole motion and kinetic exchange. In the limit $h \rightarrow 0$ we recover the Gutzwiller ansatz (3.48). For $g \rightarrow \infty$ and $h \ll 1$ this variational problem is equivalent to that of the t - J Hamiltonian with respect to a fully Gutzwiller-projected mean-field state, described in section 3.3.

4.1 The 1/r Hubbard chain

In general, the wave function (4.1) is very hard to use and calculations have to be performed numerically. An exception is the 1/r Hubbard chain defined by the Hamiltonian

$$\hat{H} = \hat{T} + \hat{V} = \sum_{\substack{m,n=1 \\ m \neq n}}^L t_{m,n} c_{m\sigma}^\dagger c_{n\sigma} + U \sum_{m=1}^L \left(\hat{n}_{m\uparrow} - \frac{1}{2} \right) \left(\hat{n}_{m\downarrow} - \frac{1}{2} \right) , \quad (4.2)$$

with hopping integrals

$$t_{m,n} = \frac{i\pi t}{L} \frac{(-1)^{m-n}}{\sin \left[\frac{\pi(m-n)}{L} \right]} . \quad (4.3)$$

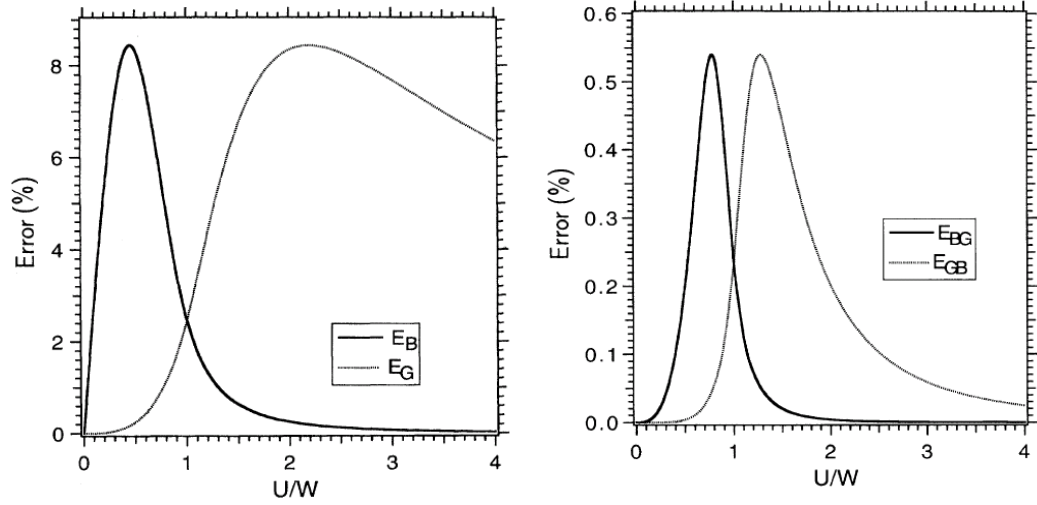


Figure 4.1: Errors in percent between the variational and the exact ground state energies. Left: The Gutzwiller ansatz and its insulating counterpart. Right: The refined wave functions $|\Psi_{GB}\rangle$ and $|\Psi_{BG}\rangle$. From [38].

This model has been introduced by Gebhard and Ruckenstein [39], who were able to calculate the exact ground state energy. They also showed that a Mott metal-insulator transition occurs at half-filling as a function of U , at a critical point $U = W = 2\pi t$. The Mott transition has been studied variationally for this model by Dzierzawa *et al.* [38], who used Eq. (4.1) (with $|\Psi_0\rangle = |FS\rangle$) together with a second trial state

$$|\Psi_{BG}\rangle = e^{-g\hat{D}}e^{-h\hat{T}}|\Psi_\infty\rangle. \quad (4.4)$$

Here $|\Psi_\infty\rangle$ is the exact ground state of the model for $U \rightarrow \infty$, which can be obtained as $\lim_{g \rightarrow \infty} e^{-g\hat{D}}|\Psi_0\rangle$ in the present case. It can be shown that $|\Psi_{GB}\rangle$ has a finite Drude weight and is therefore metallic, whereas $|\Psi_{BG}\rangle$ is insulating (vanishing Drude weight) [40]. It means that the Mott transition occurs at the repulsion U for which the variational energies for both wave functions are equal. Fig. 4.1 shows the difference between variational and exact ground state energies, for the wave functions (4.1) and (4.4), as well as for the Gutzwiller ansatz $|\Psi_G\rangle = e^{-g\hat{D}}|\Psi_0\rangle$ and its insulating partner $|\Psi_B\rangle = e^{-h\hat{T}}|\Psi_\infty\rangle$. The wave functions $|\Psi_G\rangle$ and $|\Psi_{GB}\rangle$, describing delocalized states, are especially appropriate for $U/W < 1$, whereas the functions $|\Psi_B\rangle$ and $|\Psi_{BG}\rangle$, describing localized states, should be used for $U/W > 1$. Thus the Mott transition occurs both for the pair $(|\Psi_G\rangle, |\Psi_B\rangle)$ and for the pair $(|\Psi_{GB}\rangle, |\Psi_{BG}\rangle)$ at $U = W$, in agreement with the exact result. Moreover, it is interesting to note that the refinement of the wave functions leads to a reduction of the variational error (the energy difference between the approximate and exact ground states) by one order of magnitude in this simple one-dimensional model.

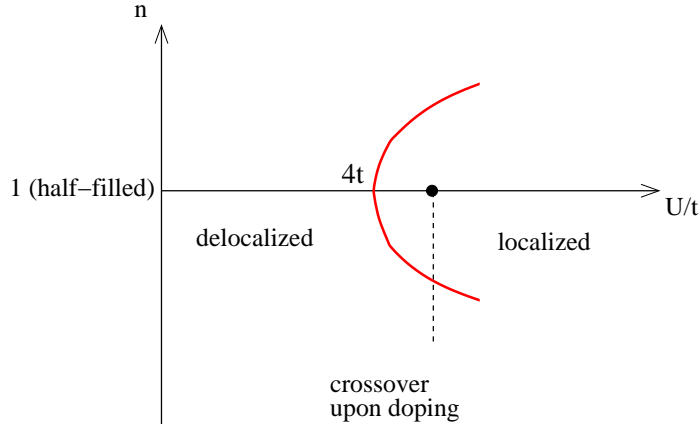


Figure 4.2: Crossover in the 2D Hubbard model. At half-filling, the value $U_{cr} \approx 4t$ can be estimated from variational calculation [41] or quantum Monte Carlo simulation [42]. When the system is doped, the crossover region is not yet accurately known, but a shape such as the red curve seems reasonable. Indeed, for $n \rightarrow 0$ the probability of double occupancy is weak, the electron motion is almost free and the critical U for the crossover is expected to diverge. It follows that a system in the localized regime at half-filling may crossover to the delocalized regime upon doping.

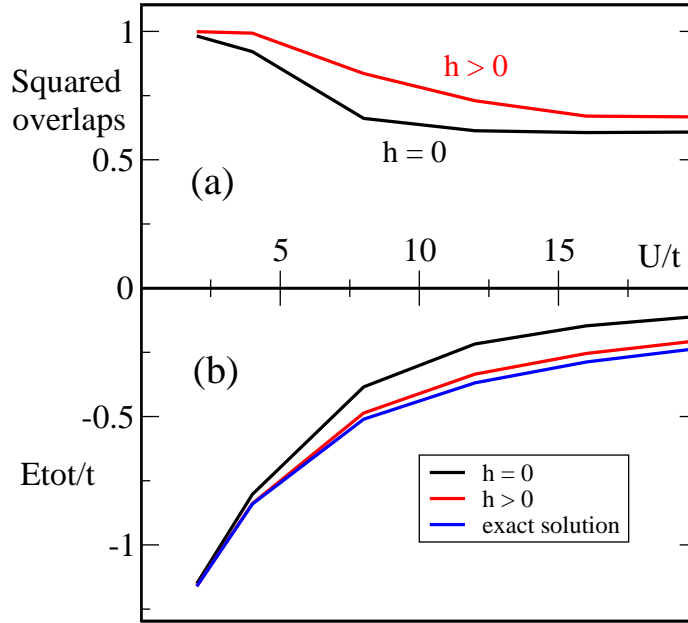


Figure 4.3: (a) Squared overlaps between the exact ground state for a small 2D cluster at half-filling and the variational ground state (projected Fermi sea) with $h = 0$ or $h > 0$ (optimized). (b) Comparison between the variational energy in both cases $h = 0$ or $h > 0$ and the exact energy. From [43].

Let us come back to the case of our two-dimensional Hubbard model. The value of the Coulomb repulsion $U = 8t$ used in our description of the high-Tc cuprates is exactly equal to the bandwidth of the square lattice, hence the result of the 1D model extended to the plane suggests that both wave functions $|\Psi_{GB}\rangle$ and $|\Psi_{BG}\rangle$ are reasonable. However, more than the ratio U/W , the character of the state (localized or delocalized) is important to decide what wave function should be used. For the 2D Hubbard model, this character is expected to depend on the hole concentration. Actually, a crossover between a localized and a delocalized regime may occur upon doping in this model, as depicted in Fig. 4.2.

Our system (with $U = 8t$) is located in the localized regime at half-filling and therefore a localized wave function should be used in this case. The refined wave function (4.1) is more appropriate to study the moderate doping case corresponding to overdoped cuprates, where the system is expected to be in the delocalized regime. Nevertheless, due the large degeneracy of the ground state $|\Psi_\infty\rangle$ in the infinite U limit, a localized wave function such as $|\Psi_{BG}\rangle = e^{-g\hat{D}}e^{-h\hat{T}}|\Psi_\infty\rangle$ would be very hard to study. For this reason, the wave function (4.1) is also used to investigate the weakly doped system.

4.2 Small clusters

For a small two-dimensional cluster, the true ground state can be obtained by exact diagonalization and serve as a crucial test for our ansatz. Such a comparison between the exact ground state and the variational wave function (4.1) (with $|\Psi_0\rangle = |FS\rangle$) has been made by Otsuka [43] for the simple Hubbard model with 10 electrons on a two-dimensional 10 site cluster. The results both for the energy difference and for the squared overlap of exact and variational ground states are shown in Fig. 4.3. The kinetic projector allows one to reduce substantially the total energy, as indicated by the comparison with the case $h = 0$. For $U = 8t$, the error is even reduced by one order of magnitude. At the same time the squared overlap is found to increase considerably, especially for intermediate values of U . The improvement is about 18% with respect to the Gutzwiller ansatz for $U = 8t$. The kinetic projector modifies the variational ground state, for instance by enhancing the spin correlations, and we can expect a significant improvement of relevant physical quantities (like the correlation functions) when derived from this ground state.

4.3 Antiferromagnetism

At or near half-filling, the antiferromagnetic instability is expected to be dominant, according to both renormalization group calculations for small U [18],[17] and quantum Monte Carlo calculations for intermediate U [26],[27]. The instability for

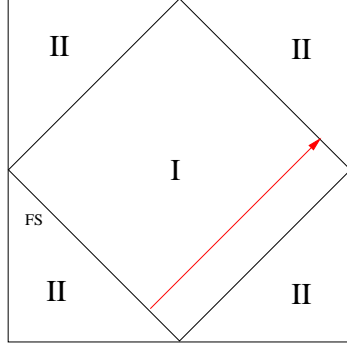


Figure 4.4: Fermi surface for a half-filled system with nearest-neighbor hopping. The First Brillouin Zone can be separated into a part I (antiferromagnetic zone) and a part II. The nesting vector (π, π) is also shown.

small U arises from the nesting of the Fermi surface for the vector $\vec{Q} = (\pi, \pm\pi)$. An appropriate choice for the state $|\Psi_0\rangle$ at half-filling is therefore the ground state of the antiferromagnetic mean-field Hamiltonian. This Hamiltonian is defined by

$$\begin{aligned}
 \hat{H}_{AF} &= \hat{H}_0 - \Delta_{AF} \sum_{i\sigma} (-1)^i \sigma c_{i\sigma}^\dagger c_{i\sigma} \\
 &= \hat{H}_0 - \Delta_{AF} \frac{1}{L} \sum_{\vec{k}, \vec{k}'\sigma} \sigma c_{\vec{k}\sigma}^\dagger c_{\vec{k}'\sigma} \sum_{\vec{r}_i} e^{i\vec{Q}\vec{r}_i} e^{i(-\vec{k}+\vec{k}')\vec{r}_i} \\
 &= \hat{H}_0 - \Delta_{AF} \sum_{\vec{k}\sigma} \sigma c_{\vec{k}\sigma}^\dagger c_{\vec{k}+\vec{Q}\sigma} .
 \end{aligned} \tag{4.5}$$

The First Brillouin Zone can be separated into a part I where $\epsilon_{\vec{k}} \leq 0$ and a part II where $\epsilon_{\vec{k}} > 0$, as shown in Figure 4.4. A momentum \vec{k}' in the part II can be written $\vec{k}' = \vec{k} + \vec{Q} \pmod{\vec{K}}$ with \vec{k} in part I and \vec{K} a vector of the reciprocal lattice. It allows us to write the mean-field Hamiltonian as:

$$\hat{H}_{AF} = \sum_{\substack{\vec{k} \in I \\ \sigma}} \epsilon_{\vec{k}} (c_{\vec{k}\sigma}^\dagger c_{\vec{k}\sigma} - c_{\vec{k}+\vec{Q}\sigma}^\dagger c_{\vec{k}+\vec{Q}\sigma}) - \Delta_{AF} \sum_{\substack{\vec{k} \in I \\ \sigma}} \sigma (c_{\vec{k}\sigma}^\dagger c_{\vec{k}+\vec{Q}\sigma} + c_{\vec{k}+\vec{Q}\sigma}^\dagger c_{\vec{k}\sigma}) \tag{4.6}$$

where the relation $\epsilon_{\vec{k}+\vec{Q}} = -\epsilon_{\vec{k}}$ has been used. The Bogoliubov transformation

$$\begin{aligned}
 c_{\vec{k}\sigma} &= u_{\vec{k}} \alpha_{\vec{k}\sigma} - \sigma v_{\vec{k}} \alpha_{\vec{k}+\vec{Q}\sigma} \\
 c_{\vec{k}+\vec{Q}\sigma} &= \sigma v_{\vec{k}} \alpha_{\vec{k}\sigma} + u_{\vec{k}} \alpha_{\vec{k}+\vec{Q}\sigma}
 \end{aligned} \tag{4.7}$$

diagonalizes this Hamiltonian. We obtain

$$\hat{H}_{AF} = \sum_{\substack{\vec{k} \in I \\ \sigma}} E_{\vec{k}} (\alpha_{\vec{k}\sigma}^\dagger \alpha_{\vec{k}\sigma} - \alpha_{\vec{k}+\vec{Q}\sigma}^\dagger \alpha_{\vec{k}+\vec{Q}\sigma}) \tag{4.8}$$

with $E_{\vec{k}} = \text{sign}(\epsilon_{\vec{k}}) \sqrt{\epsilon_{\vec{k}}^2 + \Delta_{AF}^2}$, if

$$u_{\vec{k}} = \sqrt{\frac{|E_{\vec{k}}| + |\epsilon_{\vec{k}}|}{2|E_{\vec{k}}|}}, \quad v_{\vec{k}} = \text{sign}(\epsilon_{\vec{k}}) \sqrt{1 - u_{\vec{k}}^2}. \quad (4.9)$$

At half-filling the ground state is a spin density-wave (SDW) given by

$$|SDW\rangle = \prod_{\substack{\vec{k} \in I \\ \epsilon_{\vec{k}} < \epsilon_F}} \alpha_{\vec{k}\uparrow}^\dagger \alpha_{\vec{k}\downarrow}^\dagger |0\rangle. \quad (4.10)$$

The refined wave function for the antiferromagnetic instability is therefore

$$|\Psi_{GB}^{AF}\rangle = e^{-h\hat{T}} e^{-g\hat{D}} |SDW\rangle. \quad (4.11)$$

4.3.1 Monte Carlo simulation for $|\Psi_{GB}^{AF}\rangle$

The state $|SDW\rangle$ is easily defined in momentum space where the operator \hat{D} is not diagonal. A discrete Hubbard-Stratonovich transformation [44] is applied to decouple the terms $n_{i\uparrow}n_{i\downarrow}$ in the operator $e^{-g\hat{D}}$ by introducing an Ising spin τ_i at each site:

$$\begin{aligned} e^{-g\hat{D}} &= e^{-g \sum_i n_{i\uparrow} n_{i\downarrow}} \\ &= \prod_i \frac{1}{2} \sum_{\tau=-1}^1 e^{[2a\tau(n_{i\uparrow} - n_{i\downarrow}) - \frac{1}{2}g(n_{i\uparrow} + n_{i\downarrow})]} \quad , \quad a = \text{arctg} \sqrt{\text{th} \frac{g}{4}} \\ &= \frac{1}{2} Tr_{\{\tau_i\}} e^{\sum_i (2a\tau_i - \frac{1}{2}g)n_{i\uparrow}} e^{\sum_i (-2a\tau_i - \frac{1}{2}g)n_{i\downarrow}}, \end{aligned} \quad (4.12)$$

where τ_i takes the value 1 and -1. All operators have to be written in momentum space, in particular:

$$\begin{aligned} n_{i\sigma} &= c_{i\sigma}^\dagger c_{i\sigma} = \frac{1}{L^2} \sum_{\vec{k}, \vec{k}'} e^{i(-\vec{k} + \vec{k}') \cdot \vec{n}_i} c_{\vec{k}\sigma}^\dagger c_{\vec{k}'\sigma} \\ &= \frac{1}{L^2} \sum_{\vec{k}, \vec{k}' \in I} \left[e^{i(-\vec{k} + \vec{k}') \cdot \vec{n}_i} c_{\vec{k}\sigma}^\dagger c_{\vec{k}'\sigma} + e^{i(-\vec{k} + \vec{k}' + \vec{Q}) \cdot \vec{n}_i} c_{\vec{k}\sigma}^\dagger c_{\vec{k}' + \vec{Q}\sigma} \right. \\ &\quad \left. + e^{i(-\vec{k} - \vec{Q} + \vec{k}') \cdot \vec{n}_i} c_{\vec{k} + \vec{Q}\sigma}^\dagger c_{\vec{k}'\sigma} + e^{i(-\vec{k} + \vec{k}') \cdot \vec{n}_i} c_{\vec{k} + \vec{Q}\sigma}^\dagger c_{\vec{k}' + \vec{Q}\sigma} \right]. \end{aligned} \quad (4.13)$$

The Bogoliubov transformation (4.7) leads to

$$\begin{aligned}
n_{i\sigma} = & \frac{1}{L^2} \sum_{\vec{k}, \vec{k}' \in I} e^{i(-\vec{k}+\vec{k}') \cdot \vec{n}_i} \left[(u_{\vec{k}} u_{\vec{k}'} + \sigma u_{\vec{k}} v_{\vec{k}'} e^{i\vec{Q} \cdot \vec{n}_i} + \sigma v_{\vec{k}} u_{\vec{k}'} e^{-i\vec{Q} \cdot \vec{n}_i} + v_{\vec{k}} v_{\vec{k}'}) \alpha_{\vec{k}\sigma}^\dagger \alpha_{\vec{k}'\sigma} \right. \\
& + (-\sigma u_{\vec{k}} v_{\vec{k}'} + u_{\vec{k}} u_{\vec{k}'} e^{i\vec{Q} \cdot \vec{n}_i} - v_{\vec{k}} v_{\vec{k}'} e^{-i\vec{Q} \cdot \vec{n}_i} + \sigma v_{\vec{k}} u_{\vec{k}'}) \alpha_{\vec{k}\sigma}^\dagger \alpha_{\vec{k}'+\vec{Q}\sigma} \\
& + (-\sigma v_{\vec{k}} u_{\vec{k}'} - v_{\vec{k}} v_{\vec{k}'} e^{i\vec{Q} \cdot \vec{n}_i} + u_{\vec{k}} u_{\vec{k}'} e^{-i\vec{Q} \cdot \vec{n}_i} + \sigma u_{\vec{k}} v_{\vec{k}'}) \alpha_{\vec{k}+\vec{Q}\sigma}^\dagger \alpha_{\vec{k}'\sigma} \\
& \left. + (v_{\vec{k}} v_{\vec{k}'} - \sigma v_{\vec{k}} u_{\vec{k}'} e^{i\vec{Q} \cdot \vec{n}_i} - \sigma u_{\vec{k}} v_{\vec{k}'} e^{-i\vec{Q} \cdot \vec{n}_i} + u_{\vec{k}} u_{\vec{k}'}) \alpha_{\vec{k}+\vec{Q}\sigma}^\dagger \alpha_{\vec{k}'+\vec{Q}\sigma} \right] , \quad (4.14)
\end{aligned}$$

and therefore we obtain

$$\sum_i (\sigma 2a\tau_i - \frac{1}{2}g) n_{i\sigma} = \sum_{\vec{k}, \vec{k}'} \beta_{\vec{k}\sigma}^\dagger W_{\vec{k}\vec{k}'}^\sigma(\{\tau_i\}) \beta_{\vec{k}'\sigma} , \quad (4.15)$$

where the operators β are defined as

$$(\beta_{\vec{k}_1\sigma}, \dots, \beta_{\vec{k}_M\sigma}, \beta_{\vec{k}_{M+1}\sigma}, \dots, \beta_{\vec{k}_{2M}\sigma}) = (\alpha_{\vec{k}_1\sigma}, \dots, \alpha_{\vec{k}_M\sigma}, \alpha_{\vec{k}_1+\vec{Q}\sigma}, \dots, \alpha_{\vec{k}_M+\vec{Q}\sigma}) ,$$

$M = \frac{L^2}{2}$ being the number of momenta included in part I of the First Brillouin Zone. Each time the notation β is used instead of α for the quasiparticles, it means that the subscript of \vec{k} ranges from 1 to $2M$. Therefore $W_{\vec{k}\vec{k}'}$ is a (Hermitian) $2M \times 2M$ matrix. Eventually, we get for the Gutzwiller operator:

$$e^{-g\hat{D}} = \frac{1}{2} Tr_{\{\tau_i\}} e^{\sum_{\vec{k}, \vec{k}'} \beta_{\vec{k}\uparrow}^\dagger W_{\vec{k}\vec{k}'}^\uparrow(\{\tau_i\}) \beta_{\vec{k}'\uparrow}} \cdot e^{\sum_{\vec{k}, \vec{k}'} \beta_{\vec{k}\downarrow}^\dagger W_{\vec{k}\vec{k}'}^\downarrow(\{\tau_i\}) \beta_{\vec{k}'\downarrow}} . \quad (4.16)$$

Correspondingly, we write the kinetic operator as

$$\begin{aligned}
t\hat{T} &= \sum_{\vec{k}\sigma} \epsilon_{\vec{k}} c_{\vec{k}\sigma}^\dagger c_{\vec{k}\sigma} \\
&= \sum_{\vec{k} \in I, \sigma} \epsilon_{\vec{k}} (c_{\vec{k}\sigma}^\dagger c_{\vec{k}\sigma} - c_{\vec{k}+\vec{Q}\sigma}^\dagger c_{\vec{k}+\vec{Q}\sigma}) \\
&= \sum_{\vec{k} \in I, \sigma} \epsilon_{\vec{k}} \left[(u_{\vec{k}}^2 - v_{\vec{k}}^2) \alpha_{\vec{k}\sigma}^\dagger \alpha_{\vec{k}\sigma} - 2\sigma u_{\vec{k}} v_{\vec{k}} (\alpha_{\vec{k}\sigma}^\dagger \alpha_{\vec{k}+\vec{Q}\sigma} + \alpha_{\vec{k}+\vec{Q}\sigma}^\dagger \alpha_{\vec{k}\sigma}) \right. \\
&\quad \left. - (u_{\vec{k}}^2 - v_{\vec{k}}^2) \alpha_{\vec{k}+\vec{Q}\sigma}^\dagger \alpha_{\vec{k}+\vec{Q}\sigma} \right] \\
&= t \sum_{\vec{k}, \vec{k}', \sigma} \beta_{\vec{k}\sigma}^\dagger T_{\vec{k}\vec{k}'}^\sigma \beta_{\vec{k}'\sigma} . \quad (4.17)
\end{aligned}$$

Finally our ansatz (4.1) with an antiferromagnetic reference state is

$$\begin{aligned}
e^{-h\hat{T}}e^{-g\hat{D}}|SDW\rangle &= \frac{1}{2}Tr_{\{\tau_i\}} \left[e^{\sum_{\vec{k},\vec{k}'} \beta_{\vec{k}\uparrow}^\dagger T_{\vec{k}\vec{k}'}^\dagger \beta_{\vec{k}'\uparrow}} \cdot e^{\sum_{\vec{k},\vec{k}'} \beta_{\vec{k}\uparrow}^\dagger W_{\vec{k}\vec{k}'}^\dagger (\{\tau_i\}) \beta_{\vec{k}'\uparrow}} \right. \\
&\quad \cdot e^{\sum_{\vec{k},\vec{k}'} \beta_{\vec{k}\downarrow}^\dagger T_{\vec{k}\vec{k}'}^\dagger \beta_{\vec{k}'\downarrow}} \cdot e^{\sum_{\vec{k},\vec{k}'} \beta_{\vec{k}\downarrow}^\dagger W_{\vec{k}\vec{k}'}^\dagger (\{\tau_i\}) \beta_{\vec{k}'\downarrow}} \left. \right] |SDW\rangle \\
&= \frac{1}{2}Tr_{\{\tau_i\}} \left[E^\dagger(\{\tau_i\}) E^\downarrow(\{\tau_i\}) \right] \prod_{\substack{\vec{k} \in I \\ \epsilon_{\vec{k}} < \epsilon_F}} \alpha_{\vec{k}\uparrow}^\dagger \alpha_{\vec{k}\downarrow}^\dagger |0\rangle \quad (4.18)
\end{aligned}$$

with

$$E^\sigma(\{\tau_i\}) = e^{\sum_{\vec{k},\vec{k}'} \beta_{\vec{k}\sigma}^\dagger T_{\vec{k}\vec{k}'}^\sigma \beta_{\vec{k}'\sigma}} \cdot e^{\sum_{\vec{k},\vec{k}'} \beta_{\vec{k}\sigma}^\dagger W_{\vec{k}\vec{k}'}^\sigma (\{\tau_i\}) \beta_{\vec{k}'\sigma}}. \quad (4.19)$$

Now the variational energy can be computed from the knowledge of the single-particle Green's functions, given by (see Appendix D)

$$\begin{aligned}
G_{\vec{q}_i, \vec{q}_j}^\sigma &:= \langle \beta_{\vec{q}_i, \sigma}^\dagger \beta_{\vec{q}_j, \sigma} \rangle = \frac{\langle \Psi_{GB}^{AF} | \beta_{\vec{q}_i, \sigma}^\dagger \beta_{\vec{q}_j, \sigma} | \Psi_{GB}^{AF} \rangle}{\langle \Psi_{GB}^{AF} | \Psi_{GB}^{AF} \rangle} \\
&= \frac{Tr_{\{\tau_i, \tau_{i'}\}} \left[|\tilde{B}^{-\sigma}| |\tilde{B}^\sigma| \cdot |\tilde{E}_{\vec{q}_j}^\sigma (\tilde{B}^\sigma)^{-1} \tilde{E}_{\vec{q}_i}^{\dagger\sigma}| \right]}{Tr_{\{\tau_i, \tau_{i'}\}} \left[|\tilde{B}^{-\sigma}| |\tilde{B}^\sigma| \right]} \quad (4.20)
\end{aligned}$$

where $B^\sigma \equiv B^\sigma(\{\tau_i\}, \{\tau_{i'}\}) = E^{\dagger\sigma}(\{\tau_{i'}\}) \cdot E^\sigma(\{\tau_i\})$, \tilde{B}^σ is the first $\frac{N}{2} \times \frac{N}{2}$ sub-matrix of B^σ (with respect to the single-particle states $|\vec{k}\rangle$) and $\tilde{E}_{\vec{q}_j}^\sigma$ means the first $N/2$ elements of row j of E^σ , while $\tilde{E}_{\vec{q}_i}^{\dagger\sigma}$ means the first $N/2$ elements of column i of $E^{\dagger\sigma}$.

The trace has to be performed over a large number of Ising spin configurations. Practically, it is realized using a Monte Carlo simulation, as defined in Section 3.3.2. The Green's functions are written

$$G_{\vec{q}_i, \vec{q}_j}^\sigma = Tr_{\{\tau_i, \tau_{i'}\}} \left[P(\tau_i, \tau_{i'}) |\tilde{E}_{\vec{q}_j}^\sigma (\tilde{B}^\sigma)^{-1} \tilde{E}_{\vec{q}_i}^{\dagger\sigma}| \right] \quad (4.21)$$

where

$$P(\tau_i, \tau_{i'}) = \frac{|\tilde{B}^{-\sigma}| |\tilde{B}^\sigma|}{Tr_{\{\tau_i, \tau_{i'}\}} \left[|\tilde{B}^{-\sigma}| |\tilde{B}^\sigma| \right]}. \quad (4.22)$$

$P(\tau_i, \tau_{i'})$ is a weight which can be taken as the probability of a particular Ising spin configuration. The corresponding distribution is defined as P . A set of M configurations with a distribution in agreement with P can be generated using the Metropolis algorithm, and then the Green's functions are obtained as the average over these configurations:

$$G_{\vec{q}_i, \vec{q}_j}^\sigma = \lim_{M \rightarrow \infty} \frac{1}{M} \sum_{l=1}^M |\tilde{E}_{\vec{q}_j}^\sigma (\tilde{B}^\sigma)^{-1} \tilde{E}_{\vec{q}_i}^{\dagger\sigma}|_l. \quad (4.23)$$

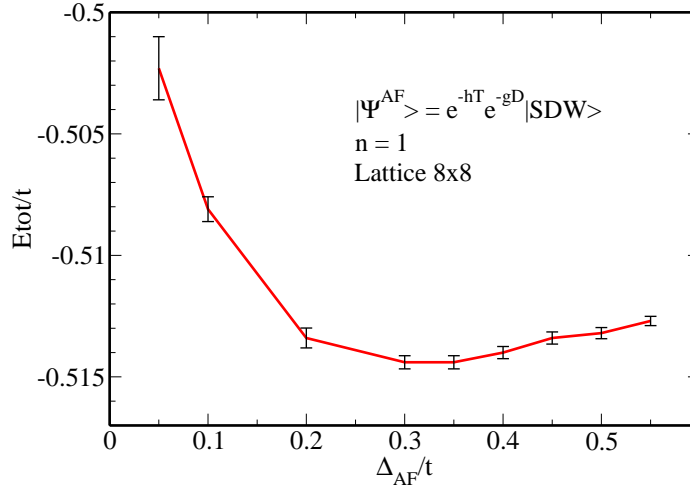


Figure 4.5: Variational energy as a function of the antiferromagnetic gap parameter for an 8×8 lattice and $U = 8t$. Along the curve, both variational parameters g and h are already optimized.

4.3.2 Half-filled case

We discuss here the case of an average site occupation $n = 1$. The variational energy for an 8×8 lattice as a function of the gap parameter is given in Fig. 4.5. The opening of an antiferromagnetic gap allows to lower substantially the total energy of the system. In order to know whether a true long-range order is present in the ground state, we compute the antiferromagnetic order parameter, the staggered magnetization, defined by

$$M = \frac{1}{L^2} \sum_i (-1)^i \langle n_{i\uparrow} - n_{i\downarrow} \rangle. \quad (4.24)$$

In Table 4.1 the variational parameter Δ_{AF} , the staggered magnetization as well as the total energy of the ground state are compared with the unrestricted Hartree-Fock approximation ($g = h = 0$), the Gutzwiller wave function ($g > 0, h = 0$) [45], a quantum Monte Carlo simulation [26] and a Projector Operator technique [35]. The gap parameter Δ_{AF} is very large for $g = h = 0$ and decreases dramatically if g and h are optimized, due to the spin fluctuations that are introduced by the Gutzwiller projector and then enhanced by the kinetic projector. We note that the gap parameter cannot be identified with an excitation gap, which in fact should vanish if a continuous symmetry is broken.

As expected, the ground state energy is seen to vary appreciably as the parameters g and h are turned on and to be comparable to that found with other techniques. On the other hand, the order parameter is still rather large, at least in comparison

	g	h	Δ_{AF}	M	E/t
VMC	0	0	3.6(1)	0.89(1)	-0.466(1)
VMC	0.69	0	1.3	0.86(1)	-0.493(3)
VMC	3.1(1)	0.101(3)	0.32(2)	0.77(1)	-0.514(1)
QMC	-	-	-	0.42(1)	-0.48(5)
PO	-	-	-	-	-0.521(1)

Table 4.1: Variational results (VMC) for the 2D Hubbard model at half-filling (8×8 lattice, $U = 8t$), compared to quantum Monte Carlo simulations (QMC) and a Projector Operator approach (PO). The VMC data include the unrestricted Hartree-Fock approximation, the Gutzwiller ansatz and the refined wave function.

to the accepted value of $M = 0.614(1)$ for the 2D Heisenberg model ($U \rightarrow \infty$) [46], an upper bound for the Hubbard model. It means that the spin fluctuations are still not fully included, even in our refined wave function.

In order to extract some information about superconducting correlations in the presence of antiferromagnetic long-range order, we have calculated the correlation function $F_{ij} = \langle C_i^\dagger C_j \rangle$, where

$$C_i^\dagger = \sum_{j_i} \sigma_{j_i} (c_{i\uparrow}^\dagger c_{j_i\downarrow}^\dagger - c_{i\downarrow}^\dagger c_{j_i\uparrow}^\dagger) . \quad (4.25)$$

The sites j_i are the four nearest neighbors of site i and $\sigma_{j_i} = +1(-1)$ in x -(y -) direction. Thus C_i^\dagger creates a singlet pair with d -wave symmetry centred at site i . F_{ij} is found to decrease rapidly with increasing distance, as expected for a gapped system. For on-site correlations we find $F_{ii} = 0.0637(1)$ for $h \neq 0$ and $F_{ii} = 0.0592(1)$ for $h = 0$, while the results for nearest-neighbor correlations are $F_{ij} = 0.0171(1)$ for $h \neq 0$ and $F_{ij} = 0.0155(1)$ for $h = 0$. The superconducting correlations are therefore slightly enhanced by the parameter h .

4.4 The superconducting instability

At moderate doping, renormalization group calculations have shown that the dominant instability for a weak interaction corresponds to a d -wave pairing of the electrons (see Section 3.2 and [18],[17]). The mean-field state $|BCS\rangle$ obtained in Chapter 2 is therefore a natural choice for the reference state $|\psi_0\rangle$ in the refined wave function (4.1), which is written:

$$|\Psi_{GB}^{BCS}\rangle = e^{-h\hat{T}} e^{-g\hat{D}} |dBCS\rangle . \quad (4.26)$$

4.4.1 Monte Carlo simulation for $|\Psi_{GB}^{BCS}\rangle$

As already mentioned, the state $|dBCS\rangle$ has not a fixed number of particles. At first sight, the best way to compute the variational energy for a given density is therefore to project the wave function onto a fixed number of particles, as it has been done in Sections 3.3.3 or 3.4.3, and to work in a “canonical ensemble”. However, we will see that this method is not appropriate for the refined wave function. Alternatively, all particle number contributions are kept and the parameter μ is used to fix the average density. It means that in this case the calculations are carried out in a “grand canonical ensemble”.

The canonical ensemble

In the canonical ensemble, the calculation proceeds as for the antiferromagnetic wave function (Section 4.3.1 and Appendix D). To see this, the $|BCS\rangle$ state is projected onto a fixed number of particles N , in momentum space:

$$\begin{aligned}
 P_N|BCS\rangle &= P_N \left[\prod_{\vec{k}} (u_{\vec{k}} + v_{\vec{k}} c_{\vec{k}\uparrow}^\dagger c_{-\vec{k}\downarrow}^\dagger) |0\rangle \right] \\
 &= P_N \left[(u_{\vec{k}_1} + v_{\vec{k}_1} c_{\vec{k}_1\uparrow}^\dagger c_{-\vec{k}_1\downarrow}^\dagger) (u_{\vec{k}_2} + v_{\vec{k}_2} c_{\vec{k}_2\uparrow}^\dagger c_{-\vec{k}_2\downarrow}^\dagger) \cdots (u_{\vec{k}_{L^2}} + v_{\vec{k}_{L^2}} c_{\vec{k}_{L^2}\uparrow}^\dagger c_{-\vec{k}_{L^2}\downarrow}^\dagger) |0\rangle \right] \\
 &= \text{Tr}_{\{\vec{k}_i\}} \left[\underbrace{(u_{\vec{k}_{L^2}} \cdots u_{\vec{k}_{\frac{N}{2}+1}} v_{\vec{k}_{\frac{N}{2}}} \cdots v_{\vec{k}_1})}_{W(\{\vec{k}_i\})} \prod_{\substack{\vec{k}_{in} \\ n \in [1, \frac{N}{2}]}} c_{\vec{k}_{in}\uparrow}^\dagger c_{-\vec{k}_{in}\downarrow}^\dagger |0\rangle \right] \quad (4.27)
 \end{aligned}$$

Each momentum configuration corresponds to $N/2$ pairs defined by the momenta \vec{k}_{in} and has a weight $W(\{\vec{k}_i\})$. The trace means the sum over all possible configurations. By comparing this state with the antiferromagnetic mean-field ground state (4.10), it is easy to realize that the single-particle Green’s function for the particles (instead of the Bogoliubov quasiparticles) has the same form as in (4.20) after the Hubbard-Stratonovich transformation. The only difference is that now the weight $W(\{\vec{k}_i\})$ is added as a factor to the weight $|\tilde{B}^{-\sigma}| |\tilde{B}^\sigma|$ of the Ising spin configuration and the trace is performed on both Ising spin and momentum configurations.

The grand canonical ensemble

Things are slightly more complicated in the grand canonical ensemble. First the $|BCS\rangle$ state is described in term of the quasiparticle operators of the Bogoliubov transformation (B.5):

$$|BCS\rangle = \prod_{\vec{k}} \gamma_{\vec{k}\uparrow} \gamma_{-\vec{k}\downarrow} |0\rangle, \quad (4.28)$$

where $|0\rangle$ is the vacuum of particles, $c_{\vec{k}\sigma}|0\rangle = 0$. The operator $(n_{i\uparrow} - n_{i\downarrow})$ occurring in the Hubbard-Stratonovich transformation (4.12) is then given by

$$\begin{aligned} (n_{i\uparrow} - n_{i\downarrow}) &= \frac{1}{L^2} \sum_{\vec{k}, \vec{k}'} e^{i(\vec{k}-\vec{k}')\cdot\vec{n}_i} \left[u_{\vec{k}} u_{\vec{k}'} (\gamma_{\vec{k}\uparrow}^\dagger \gamma_{\vec{k}'\uparrow} - \gamma_{\vec{k}\downarrow}^\dagger \gamma_{\vec{k}'\downarrow}) \right. \\ &\quad + v_{\vec{k}} u_{\vec{k}'} (\gamma_{-\vec{k}\downarrow} \gamma_{\vec{k}'\uparrow} + \gamma_{-\vec{k}\uparrow} \gamma_{\vec{k}'\downarrow}) + u_{\vec{k}} v_{\vec{k}'} (\gamma_{\vec{k}\uparrow}^\dagger \gamma_{-\vec{k}'\downarrow}^\dagger + \gamma_{\vec{k}\downarrow}^\dagger \gamma_{-\vec{k}'\uparrow}^\dagger) \\ &\quad \left. + v_{\vec{k}} v_{\vec{k}'} (\gamma_{-\vec{k}\downarrow} \gamma_{-\vec{k}'\downarrow}^\dagger - \gamma_{-\vec{k}\uparrow} \gamma_{-\vec{k}'\uparrow}^\dagger) \right]. \end{aligned} \quad (4.29)$$

Contrary to the antiferromagnetic case the number of quasiparticles is not conserved. A particle-hole transformation for the spin up quasiparticles solves this problem. We introduce:

$$\begin{cases} \gamma_{\vec{k}\uparrow}^\dagger = \beta_{-\vec{k}} & \text{and} \\ \gamma_{\vec{k}\uparrow} = \beta_{-\vec{k}}^\dagger \end{cases} \quad \begin{cases} \gamma_{-\vec{k}\downarrow}^\dagger = \gamma_{-\vec{k}}^\dagger \\ \gamma_{-\vec{k}\downarrow} = \gamma_{-\vec{k}} \end{cases} \quad (4.30)$$

This canonical transformation gives a new definition of the vacuum. By writing

$$|\tilde{0}\rangle = \prod_{\vec{k}} \gamma_{\vec{k}} |0\rangle, \quad (4.31)$$

we have

$$\beta_{\vec{k}} |\tilde{0}\rangle = \gamma_{\vec{k}} |\tilde{0}\rangle = 0. \quad (4.32)$$

Thus $|\tilde{0}\rangle$ is the vacuum of β and γ quasiparticles. In this description, the $|BCS\rangle$ state is given by

$$|BCS\rangle = \prod_{\vec{k}} \beta_{\vec{k}}^\dagger |\tilde{0}\rangle. \quad (4.33)$$

Using the transformation (A.2), it is clear that the operator $(n_{i\uparrow} - n_{i\downarrow})$ conserves now the total number of quasiparticles. However it contains mixed terms of the form “ $\alpha^\dagger\beta$ ” or “ $\beta^\dagger\alpha$ ”. Therefore the expectation values cannot be factorized, in contrast to the antiferromagnetic ground state for which spin up and spin down components can be averaged independently. Practically, it means that we have to deal with $(2L^2) \times (2L^2)$ matrices. Using the notation

$$(\alpha_{\vec{k}_1}, \alpha_{\vec{k}_2}, \dots, \alpha_{\vec{k}_N}, \alpha_{\vec{k}_{N+1}}, \dots, \alpha_{\vec{k}_{2N}}) = (\beta_{\vec{k}_1}, \dots, \beta_{\vec{k}_N}, \gamma_{\vec{k}_1}, \dots, \gamma_{\vec{k}_N}) \quad (4.34)$$

and following the procedure outlined in Section 4.3.1, the single-particle Green's functions are obtained (details are given in Appendix E):

$$\begin{aligned} G_{\vec{q}_i, \vec{q}_j} &= \langle \alpha_{\vec{q}_i}^\dagger \alpha_{\vec{q}_j} \rangle = \frac{\langle \Psi_{GB}^{BCS} | \alpha_{\vec{q}_i}^\dagger \alpha_{\vec{q}_j} | \Psi_{GB}^{BCS} \rangle}{\langle \Psi_{GB}^{BCS} | \Psi_{GB}^{BCS} \rangle} \\ &= \frac{\text{Tr}_{\{\tau_i, \tau_{i'}\}} \left[C(\{\tau_i\}) C(\{\tau_{i'}\}) |\tilde{B}| \cdot |\tilde{E}_{\vec{q}_j}(\tilde{B})^{-1} \tilde{E}_{\vec{q}_i}^\dagger| \right]}{\text{Tr}_{\{\tau_i, \tau_{i'}\}} \left[C(\{\tau_i\}) C(\{\tau_{i'}\}) |\tilde{B}| \right]} \end{aligned} \quad (4.35)$$

where

$$\begin{aligned} B &\equiv B(\{\tau_i\}, \{\tau_{i'}\}) = E^\dagger(\{\tau_i\}) \cdot E(\{\tau_i\}) \\ C(\{\tau_i\}) &= e^{\sum_i 2a\tau_i} \\ \tilde{B} &\text{ is the first } L^2 \times L^2 \text{ sub-matrix of } B \end{aligned} \quad (4.36)$$

Due to the mixing of γ and β , the two-body operators cannot be factorized. However for a fixed configuration of the Ising spins $|\tau_i\rangle$, $|\tau_{i'}\rangle$, the mean value for quartic operators can be obtained from the mean value of quadratic operators using (see the proof in Appendix E):

$$\begin{aligned} \frac{\langle \tau_{i'} | \alpha_{\vec{q}_s}^\dagger \alpha_{\vec{q}_p} \alpha_{\vec{q}_q}^\dagger \alpha_{\vec{q}_r} | \tau_i \rangle}{|\tilde{B}|} &= \frac{\delta_{\vec{q}_p \vec{q}_q} \langle \tau_{i'} | \alpha_{\vec{q}_s}^\dagger \alpha_{\vec{q}_r} | \tau_i \rangle}{|\tilde{B}|} \\ &+ \frac{\langle \tau_{i'} | \alpha_{\vec{q}_q}^\dagger \alpha_{\vec{q}_r} | \tau_i \rangle}{|\tilde{B}|} \frac{\langle \tau_{i'} | \alpha_{\vec{q}_s}^\dagger \alpha_{\vec{q}_p} | \tau_i \rangle}{|\tilde{B}|} - \frac{\langle \tau_{i'} | \alpha_{\vec{q}_q}^\dagger \alpha_{\vec{q}_p} | \tau_i \rangle}{|\tilde{B}|} \frac{\langle \tau_{i'} | \alpha_{\vec{q}_s}^\dagger \alpha_{\vec{q}_r} | \tau_i \rangle}{|\tilde{B}|} \end{aligned} \quad (4.37)$$

This relation can be compared to Wick's theorem. It allows us to compute easily the expectation value of the double occupancy operator.

As in the antiferromagnetic case, the trace over the Ising spin configurations appearing in (4.35) or the trace over Ising spin plus momentum configurations in the canonical ensemble can be performed by a Monte Carlo simulation. The moves of the random walk of the Metropolis algorithm consist just of flipping a randomly chosen spin and for the canonical ensemble, independently, of changing the momentum $(\vec{k}_{i_n}, -\vec{k}_{i_n})$ of a randomly chosen pair by a momentum not yet attributed (randomly chosen).

4.4.2 Size effects

Figure 4.6 shows the variational energy obtained by the Monte Carlo simulation as a function of the parameter Δ , for a density $n = 0.8125$ and both for the canonical (blue curves) or for the grand canonical ensemble (red curves).

Let us first note that the energy for the refined wave function (4.6(b)) is located much below the energy of the Gutzwiller ansatz. The reduction of about 7% at $\Delta = 0$ can be compared with the values of 1% and 2% obtained respectively by the wave functions $|\Psi_{Gia}\rangle$ (see 3.50) or $|\Psi_Y\rangle$ (see 3.53) at comparable doping. It proves that contrary to these wave functions, the refined wave function allows a significative improvement also away from half-filling.

Now a striking feature of Figure (4.6), which occurs in both cases $h = 0$ and $h > 0$, is the clear disagreement between the results obtained in the canonical and in the grand canonical ensembles. Indeed, the gap vanishes in the ground state in this latter case, whereas for the canonical ensemble the opening of a finite gap is favored.

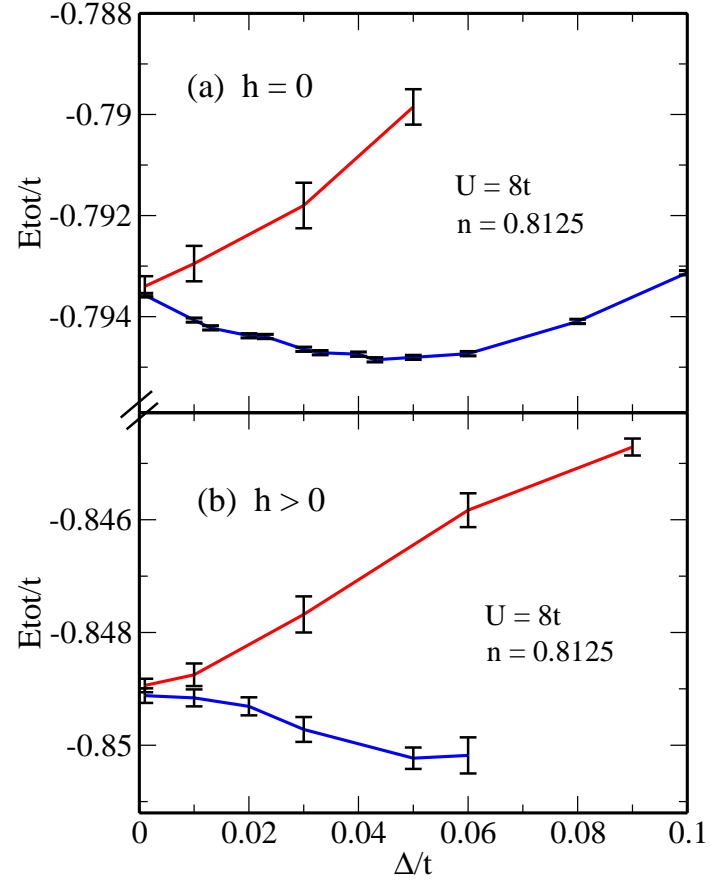


Figure 4.6: Total energy per site as a function of the gap parameter in both cases $h = 0$ (part (a)) and $h > 0$ (part (b)). The red curves give the results of the calculation in the grand canonical ensemble, while the blue curves correspond to the canonical ensemble.

The wave functions projected or not projected onto a fixed number of particles should give the same results in the thermodynamic limit. Therefore rather large size effects are present at this doping.

For a density $n \approx 0.81$, it is already known from the size dependence study of Section 3.4.3 that the gap does not persist in the thermodynamic limit for the Gutzwiller ansatz. Unfortunately, such a size dependence cannot be studied for the canonical ensemble in the case $h > 0$ where a sign problem occurs and worsens as the lattice size is increased. This numerical difficulty is analogous to the sign problem encountered in quantum Monte Carlo simulations, and is due to the fact that the weight of a particular configuration is not positively defined. The weight being taken as the probability of the configuration in the simulation, it should of course be positive. Otherwise the relative sign between different contributions is not respected, leading to an error in the calculated average. This problem can be solved by choosing a new weight, positively defined, namely the absolute value of the true weight. It is written:

$$\begin{aligned}
 \langle \hat{O} \rangle_W &= \frac{\text{Tr}_{\{U\}} [W(U) \hat{O}(U)]}{\text{Tr}_{\{U\}} [W(U)]} = \frac{\text{Tr}_{\{U\}} [|W(U)| \frac{W(U)}{|W(U)|} \hat{O}(U)]}{\text{Tr}_{\{U\}} [|W(U)| \frac{W(U)}{|W(U)|}]} \\
 &= \frac{\text{Tr}_{\{U\}} [|W(U)| \frac{W(U)}{|W(U)|} \hat{O}(U)]}{\text{Tr}_{\{U\}} [|W(U)|]} \cdot \frac{\text{Tr}_{\{U\}} [|W(U)|]}{\text{Tr}_{\{U\}} [|W(U)| \frac{W(U)}{|W(U)|}]} \\
 &= \frac{\langle \hat{O} \cdot \text{sign} W \rangle_{|W|}}{\langle \text{sign} W \rangle_{|W|}} .
 \end{aligned} \tag{4.38}$$

The expectation value of the observable \hat{O} is given as an average computed with respect to $|W|$ divided by the mean value of the sign of W . Obviously, this procedure does not work when the mean value of the sign is zero. Moreover, a small mean value already leads to a dramatic slowing down of the convergence rate. It turns out that the weight for the Ising spin configurations (the product of determinants $|\tilde{B}^{-\sigma}| |\tilde{B}^{\sigma}|$ for the canonical ensemble or the determinant $|\tilde{B}|$ for the grand canonical ensemble) has a mean value very close to one and does not lead to any sign problem. On the contrary, the factor $W(\{\vec{k}_i\})$, corresponding to the weight for the momentum configurations, has an average sign which tends rapidly to zero as the gap parameter or the lattice size is increased, as illustrated in Fig. 4.7.

The size dependence can be studied in the grand canonical ensemble, since the latter does not suffer from the sign problem. However, the optimization of the variational parameters is already very time consuming for a 8×8 lattice and it becomes completely impracticable for larger system sizes unless an appropriate method is used. The optimization method [47],[48] consists first of creating a fixed set of configurations for the Monte Carlo simulation, which are obtained for some particular values

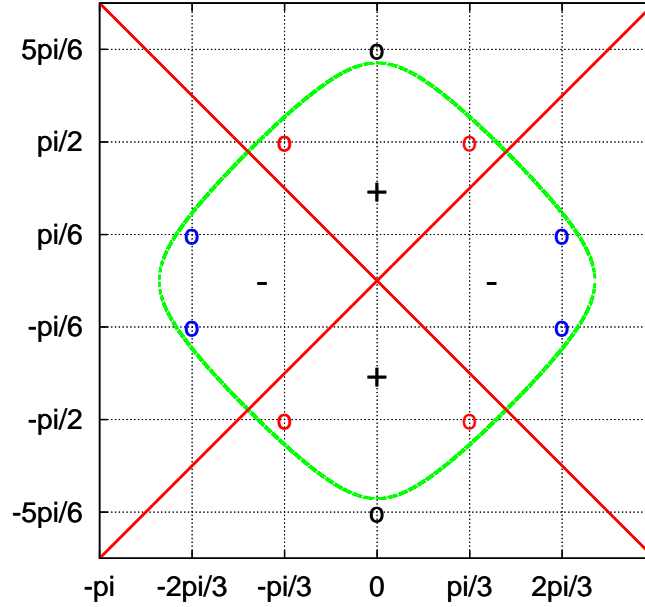


Figure 4.7: Typical first Brillouin zone for a square lattice with periodic-antiperiodic boundary conditions. The diagonal lines separate parts of the zone with different signs of the d -wave gap parameter. The weight $W(\{\vec{k}_i\})$, corresponding to a particular momentum configuration, is just the product of factors $u_{\vec{k}_i}$ for $(\vec{k}_i, -\vec{k}_i)$ unoccupied, times the product of factors $v_{\vec{k}_j}$ for $(\vec{k}_j, -\vec{k}_j)$ occupied. The sign of $v_{\vec{k}_j}$ has exactly the same dependence on the momentum as the sign of the gap parameter. If $\Delta = 0$, $v_{\vec{k}_j}$ vanishes for $\epsilon_{\vec{k}_j} > \epsilon_F$ and $W(\{\vec{k}_i\})$ is not zero only for the configuration corresponding to the Fermi sea. For a small Δ some other configurations acquire a finite weight. These configurations differ from the Fermi sea only for momenta close to the Fermi surface. For instance, a configuration where one of the momenta denoted by blue circles is empty while one of those with black circles is occupied has a non-negligible probability to occur. However, the asymmetry due to the boundary conditions implies that all the most probable configurations have the same sign. If the gap increases, some other momenta have a non-negligible probability to be empty (for instance those with red circles) and some configurations with both signs have a large weight. In this case the mean value of the sign is close to zero, leading to a sign problem. When the lattice size increases, the asymmetry is reduced and the sign problem occurs already for small Δ .

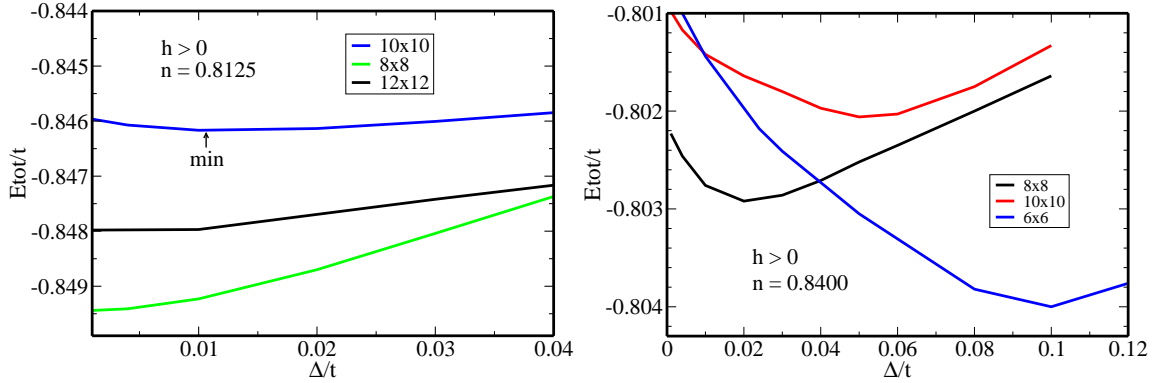


Figure 4.8: Variational energy for different lattice sizes and densities $n = 0.8125$ (left) and $n = 0.84$ (right). Calculations are performed in the grand canonical ensemble.

of the variational parameters. Then this set of configurations is used to compute the variational energy for various other choices of the variational parameters. The advantage is that now the statistical error is largely reduced from one simulation to another, which allows us to decrease the length (and the time) of the simulation. Once the minimum is found, checks are realized to ensure that the variational ground state is reached. Fig. 4.8 gives the size dependence of the total energy as a function of the gap parameter for two different densities.

The left-hand side shows that a vanishing gap parameter seems to be a robust feature of the ground state at $n = 0.8125$, although the presence of a very small gap in the thermodynamic limit cannot be excluded. The non-monotonic behavior indicates that results are still sensitive to the particular distribution of momenta in the First Brillouin Zone. For $n = 0.84$ (right-hand side), a finite gap occurs in the ground state for all studied lattice sizes. However the non-monotonic size effects are very pronounced here. It can be explained by the proximity of the superconducting transition. Indeed, if Δ is small the correlation length is quite large and the lattice size has more impact on the results. Deep inside the superconducting phase, the size effects are supposed to become less important. In Fig. 4.9 the optimal gap as a function of the inverse of the lattice size is plotted for different densities and indeed, the size effects are reduced when the gap increases. However, even for the larger gap a lattice size 6×6 seems not to be large enough to mimic the thermodynamic limit. On the contrary, a lattice size 8×8 appears to give a reliable estimate of this limit.

4.4.3 The simple Hubbard model

We now discuss in more detail the effect of hole doping and, in particular, the possibility of d -wave superconductivity. The optimization procedure being very time consuming, we have focused on the minimum size required to obtain reliable results.

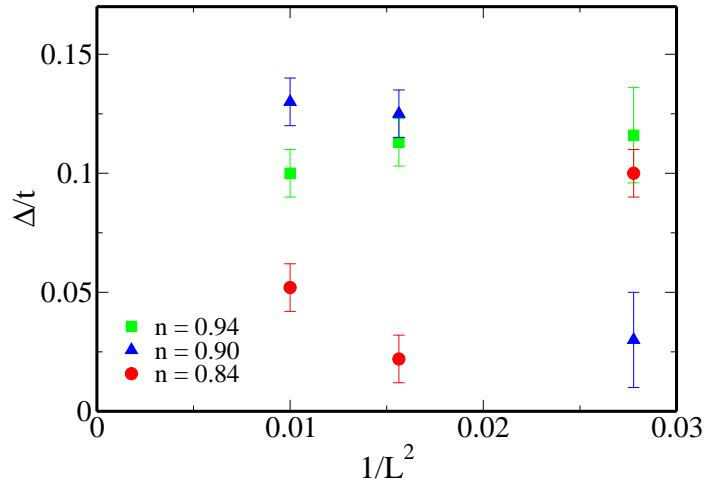


Figure 4.9: Size dependence of the optimal gap parameter for different densities.

n	μ	g	h	E/t
0.8125	-0.4418(1)	3.0(1)	0.099(2)	-0.849(1)
0.8400	-0.3972(3)	3.2(1)	0.103(2)	-0.802(1)
0.9000	0.357(1)	3.4(1)	0.106(2)	-0.697(1)
0.9375	0.620(1)	3.7(1)	0.110(2)	-0.627(1)
0.9600	0.692(1)	4.1(2)	0.115(3)	-0.583(1)
0.9700	0.743(1)	4.3(2)	0.116(3)	-0.564(1)

Table 4.2: “Chemical potential”, parameters g and h and total energy per site for different densities on an 8×8 lattice.

This is the 8×8 lattice size, as concluded both from the results of last section and from the mean-field calculation of Chapter 2. Moreover, the grand canonical ensemble has been chosen for the calculations in order to avoid the sign problem.

The ground state energy and the parameters g, h, μ are given in Table 4.2 for various densities. The chemical potential μ varies strongly with doping and increases so much for $n \rightarrow 1$ that the optimization becomes very difficult. The Gutzwiller parameter g also increases rather strongly for $n \rightarrow 1$, which indicates that the system is “more localized” at half-filling than away from half-filling [49]. In contrast, the kinetic parameter h does not vary appreciably.

A linear regression of the ground state energy as a function of the density is shown in Fig. 4.10. It allows us to get a good estimate of the energy at half-filling $E/t = -0.512(5)$, which corresponds to a decrease of about 66% with respect to the Gutzwiller variational ground state (see Table 3.1). The refined wave function

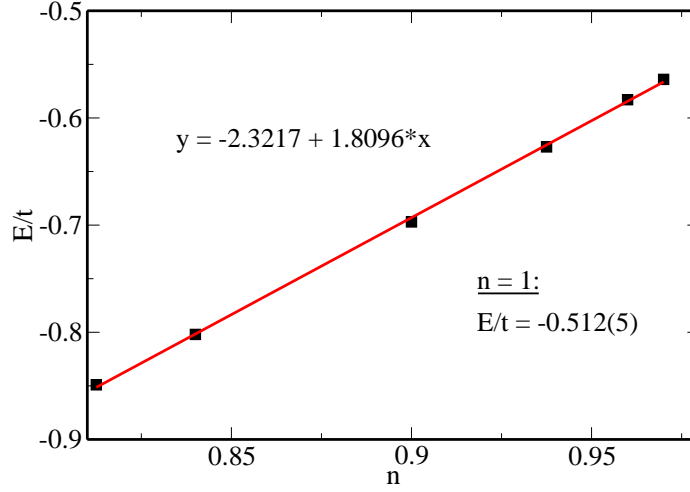


Figure 4.10: The linear regression (red curve) of the ground state energy as a function of the density allows to extract a good estimate of the ground state energy at half-filling.

is therefore also superior to the wave functions $|\Psi_{Gia}\rangle$ and $|\Psi_Y\rangle$ near half-filling, where the improvement is about 62% and 45% of the Gutzwiller energy, respectively. This is rather impressive if we remember that $|\Psi_{GB}^{BCS}\rangle$ allows only a superconducting instability, while $|\Psi_{Gia}\rangle$ includes antiferromagnetism as well.

The optimal gap parameter Δ and the superconducting order parameter $\Phi = |\langle c_{i\uparrow}^\dagger c_{j\downarrow}^\dagger \rangle|$ are given in Fig. 4.11 as functions of doping. Both quantities have a maximum around $x = 0.1$ and tend to zero around $x = 0.18$. The limiting behavior for $x \rightarrow 0$ has not been established firmly, due to computational problems already mentioned, but our results are consistent with $\Delta \rightarrow 0$, $\Phi \rightarrow 0$. The gap does not show the monotonic behavior obtained with the Gutzwiller ansatz, both for finite U and for $U \rightarrow \infty$. In particular, the identification of the gap parameter with an energy scale corresponding to an incoherent excitation (which manifests itself by the temperature T^* on the phase diagram of the cuprates (see Fig. 1.5)) is no longer substantiated.

The condensation energy, $E_{cond} = E(0) - E(\Delta)$ where Δ is the optimal gap parameter, is depicted in Figure 4.12. It vanishes for $x > 0.18$ and increases monotonically with decreasing x , even beyond the hole concentration where both Δ and Φ pass through a maximum. The limiting behaviour for $x \rightarrow 0$ is again unknown, but for $x = 0$ it is seen that antiferromagnetism prevails. The comparison with the Gutzwiller wave function (inset) indicates that the addition of the parameter h strongly enhances the condensation energy. It is worthwhile to add that according to calculations for small clusters (see Section 4.2 and [43]) the difference $\Delta E = E_{var} - E_0$ between the variational energy E_{var} and the exact ground state energy E_0 is of the same order for $h > 0$ as the condensation energy E_{cond} ($\Delta E \approx 0.007t$, $E_{cond} \approx 0.005t$ at $n = 0.9$), in contrast to the case $h = 0$ where $\Delta E \gg E_{cond}$ ($\Delta E \approx 0.08t$, $E_{cond} \approx 0.001t$). In that

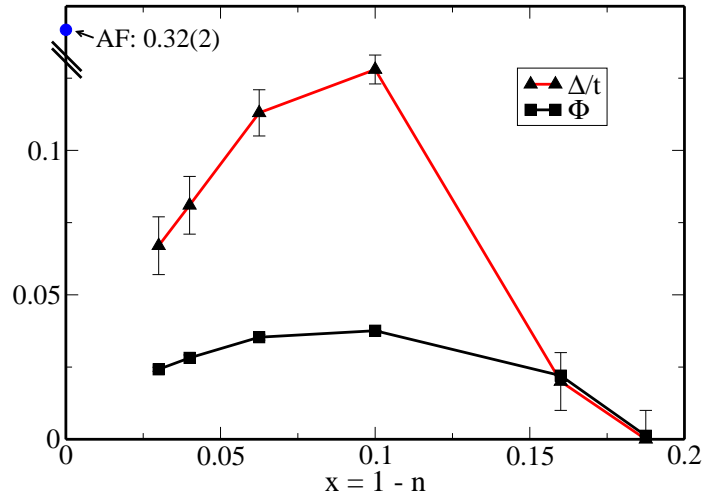


Figure 4.11: Gap and order parameter as functions of doping for an 8×8 lattice. The mark at half-filling is the antiferromagnetic gap. Error bars indicate statistical uncertainties.

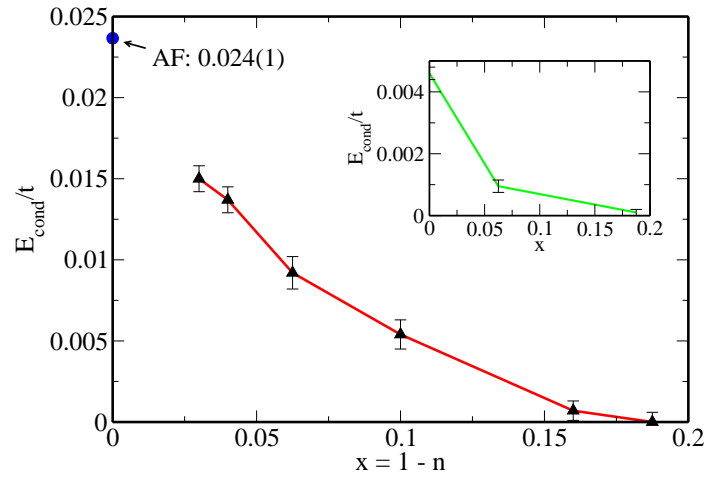


Figure 4.12: Condensation energy per site. The inset shows the condensation energy for the Gutzwiller wave function. The comparison with the condensation energy for the antiferromagnetic state at $x = 0$ (blue dot) indicates that the system gains more energy from antiferromagnetism than from superconductivity at half-filling.

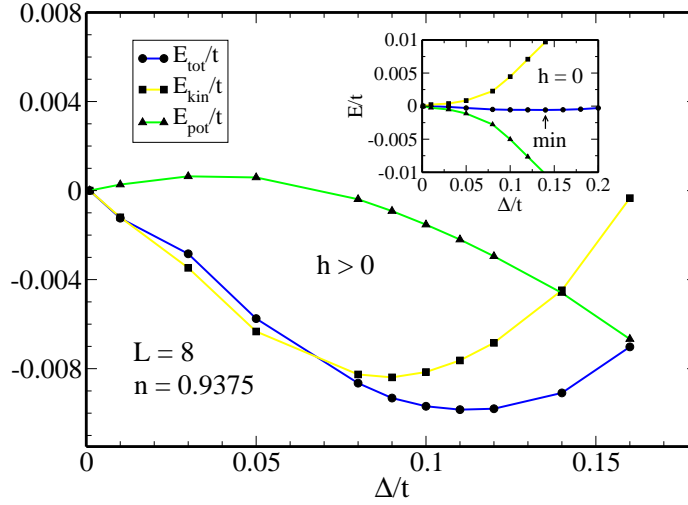


Figure 4.13: Total (circles), kinetic (squares) and potential (triangles) energies per site as functions of the gap parameter on an 8×8 lattice, for the density $n = 0.9375$. For each curve $E(\Delta = 0)$ has been subtracted. The relative error is smaller than the symbol size. The corresponding results for the Gutzwiller wave function are given in the inset.

sense, our refined wave function is close enough to the exact ground state to allow one to draw reliable conclusions about the occurrence of superconductivity.

In Fig. 4.13 the kinetic and the potential energies are plotted separately for a density $n = 0.9375$ as functions of the gap parameter. It turns out that the maximum energy gain (the condensation energy) at $\Delta = 0.11t$ is to a large extent ($> 75\%$) due to a decrease in the kinetic energy, in contrast to the BCS behavior where the condensation energy is entirely due to the potential energy. Our findings are also qualitatively different from those obtained with a Gutzwiller wave function for which the kinetic energy increases monotonically with the gap parameter (inset). The magnetic structure factor

$$S(\vec{q}) = \frac{1}{L^2} \sum_{i,j} e^{i\vec{q} \cdot (\vec{r}_i - \vec{r}_j)} \langle (n_{i\uparrow} - n_{i\downarrow})(n_{j\uparrow} - n_{j\downarrow}) \rangle \quad (4.39)$$

within the superconducting phase can also be computed. Fig. 4.14 shows this function for several densities along three different lines in the Brillouin zone. The structure factor is peaked at (π, π) , indicating antiferromagnetic correlations. The peak decreases with increasing hole concentration. The comparison with results for $h = 0$ (inset) shows that the antiferromagnetic correlations are strongly enhanced by the parameter h . These correlations could explain the decrease of the gap parameter when approaching $x = 0$. Indeed, the antiferromagnetic ordering seems not to be favorable for pairing, as shown by calculations with the wave function $|\Psi_{Gia}\rangle$ (see [36])

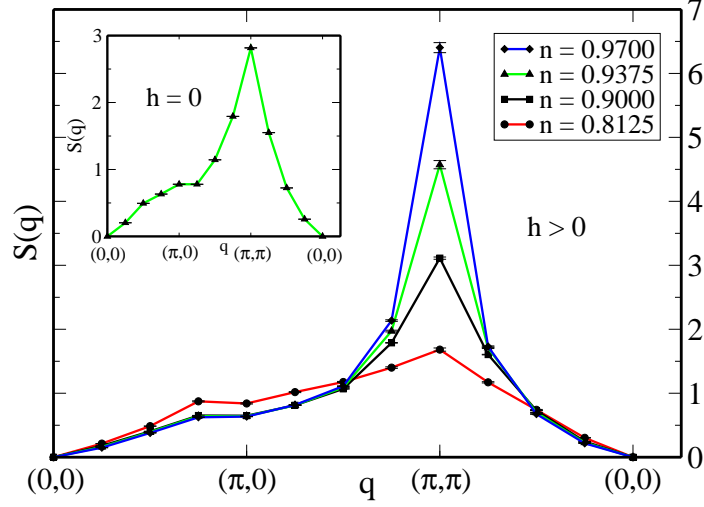


Figure 4.14: Magnetic structure factor as a function of the wave vector for different densities and an 8×8 lattice. The inset shows the magnetic structure factor for the Gutzwiller wave function at $n = 0.9375$.

and Section 3.4.4). Our results indicate that enhanced antiferromagnetic correlations are enough to prevent the formation of pairs.

4.4.4 Next-nearest-neighbor hopping

As already mentioned, the shape of the Fermi surface observed by photoemission spectroscopy does not agree with that of a tight-binding model with only nearest-neighbor hopping. Indeed, the experimental Fermi surface of cuprates at optimal doping is hole-like (see Fig. 1.6), whereas the nearest-neighbor hopping leads to an electron-like Fermi surface if the density is smaller than 1 (see Fig. 4.15). If the two-dimensional Hubbard Hamiltonian is used as an effective model for the cuprates, a t' parameter for the next-nearest-neighbor hopping should therefore be taken into account for a quantitative description, as shown in Fig. 4.15. Such a parameter can have a strong influence as the Fermi surface crosses the van Hove singularities that occurs in the density of states of the square lattice at momenta $(0, \pm\pi)$ or $(\pm\pi, 0)$ at a finite doping.

All the calculations for our refined wave function are realized in the momentum space and therefore the next-nearest-neighbor hopping can be easily included by modifying the single-particle dispersion,

$$\epsilon_{\vec{k}} = -2t(\cos k_x + \cos k_y) - 4t' \cos k_x \cos k_y. \quad (4.40)$$

A value $t' = -0.3t$, consistent with the ARPES data, is used in this study. The

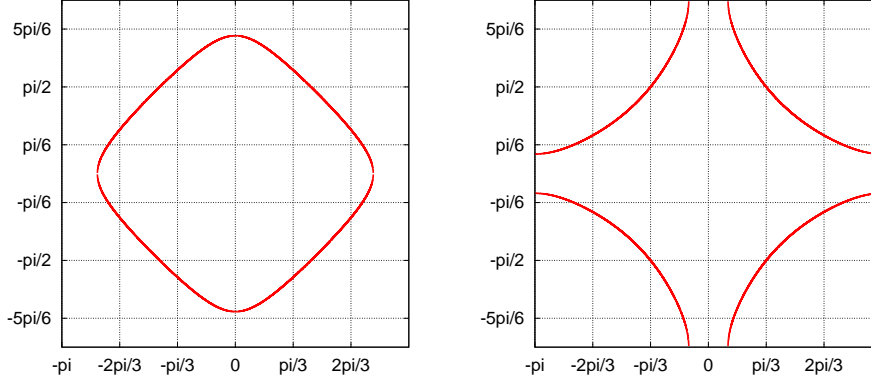


Figure 4.15: Non-interacting Fermi surface on the square lattice for a density $n = 0.85$ corresponding to the optimal doping for the cuprates. Left: An electron-like Fermi surface is obtained when only the nearest-neighbor hopping is considered. Right: The addition of a parameter $t' = -0.3t$ for the next-nearest-neighbor hopping leads to a hole-like Fermi surface.

n	μ	g	h	E/t
0.7500	-0.9921(1)	4.2(1)	0.113(2)	-0.858(1)
0.7800	-0.9612(3)	4.0(1)	0.112(2)	-0.829(1)
0.8125	-0.9107(3)	3.9(1)	0.111(2)	-0.795(1)
0.8400	-0.788(1)	3.7(1)	0.111(2)	-0.763(1)
0.9000	-0.728(1)	3.8(1)	0.111(2)	-0.676(1)
0.9500	-0.603(1)	4.0(1)	0.114(2)	-0.591(1)

Table 4.3: “Chemical potential”, parameters g and h and total energy per site for different densities on an 8×8 lattice.

optimized parameters and the energy of the variational ground state obtained for the refined wave function with a d -wave superconducting order parameter are given in the Table 4.3.

The parameters g and h vary much less than in the case $t' = 0$. The optimal gap parameter is plotted in Fig. 4.16 as a function of hole concentration. As for $t' = 0$, the gap is maximum at a density corresponding to the optimal doping defined by the order parameter (see Fig. 4.17). However it seems here that the gap remains finite at half-filling, although our results are again plagued by convergence problems in the limit $n \rightarrow 1$. The comparison with the results obtained with a larger lattice size (10×10) indicates that the size effects are still not negligible for our system size, but on the other hand they are not large enough to modify the qualitative behaviour. Fig.

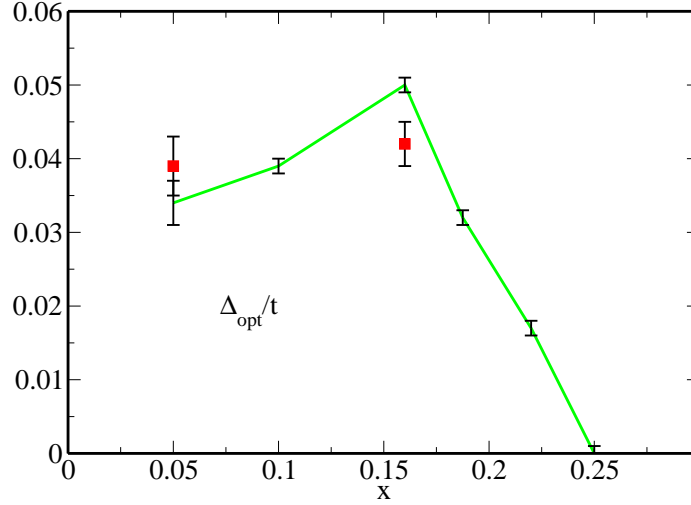


Figure 4.16: Gap parameter as a function of doping for an 8×8 lattice with $U = 8t$ and $t' = -0.3t$. The red squares are computed on a 10×10 lattice. Error bars indicate statistical uncertainties.

4.17 shows the superconducting order parameter $\Phi = |\langle c_{i\uparrow}^\dagger c_{j\downarrow}^\dagger \rangle|$. The main effect of t' is to extend the superconducting dome to a larger range of doping. The behaviour is still compatible with $\Phi \rightarrow 0$ when $x \rightarrow 0$, but now the order parameter remains finite up to $x \approx 0.25$.

By looking at the gap dependence of the kinetic, potential and total energies given in Fig. 4.18 for a density $n = 0.84$, it appears that the energy gain is entirely due to a decrease of the kinetic energy. This feature of the refined variational ground state is therefore confirmed when the next-nearest-neighbor hopping is taken into account. Finally, the magnetic structure factor is plotted for various densities in Fig. 4.19, for the superconducting refined wave function (part (a)) and for the refined wave function with $\Delta = 0$ (part (b)). Close to half-filling a peak is found at (π, π) , indicating antiferromagnetic correlations. We note that these correlations are strongly enhanced by the formation of Cooper pairs. At larger hole concentration, incommensurate spin correlations, which are not sensitive to the opening of a gap Δ , become dominant.

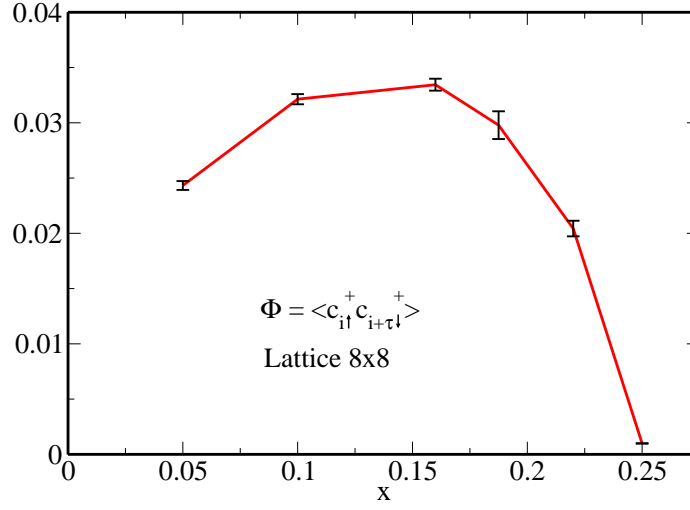


Figure 4.17: Order parameter as a function of doping for an 8×8 lattice.

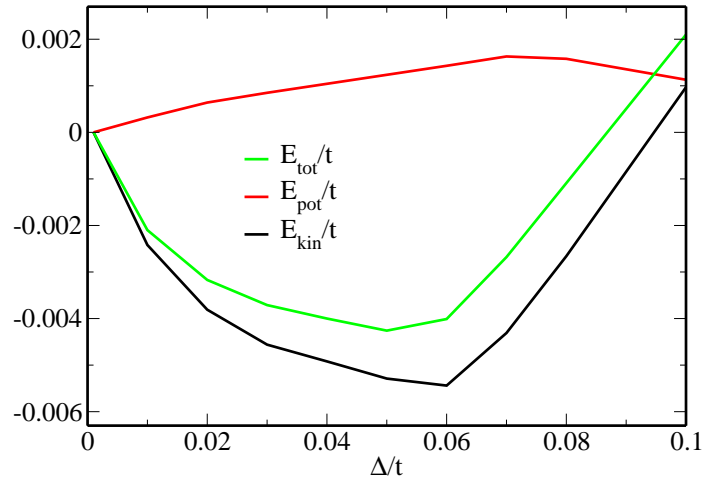


Figure 4.18: Kinetic, potential and total energies per site as functions of the gap parameter, for a density $n = 0.84$. For each curve, the energy at $\Delta = 0$ has been subtracted.

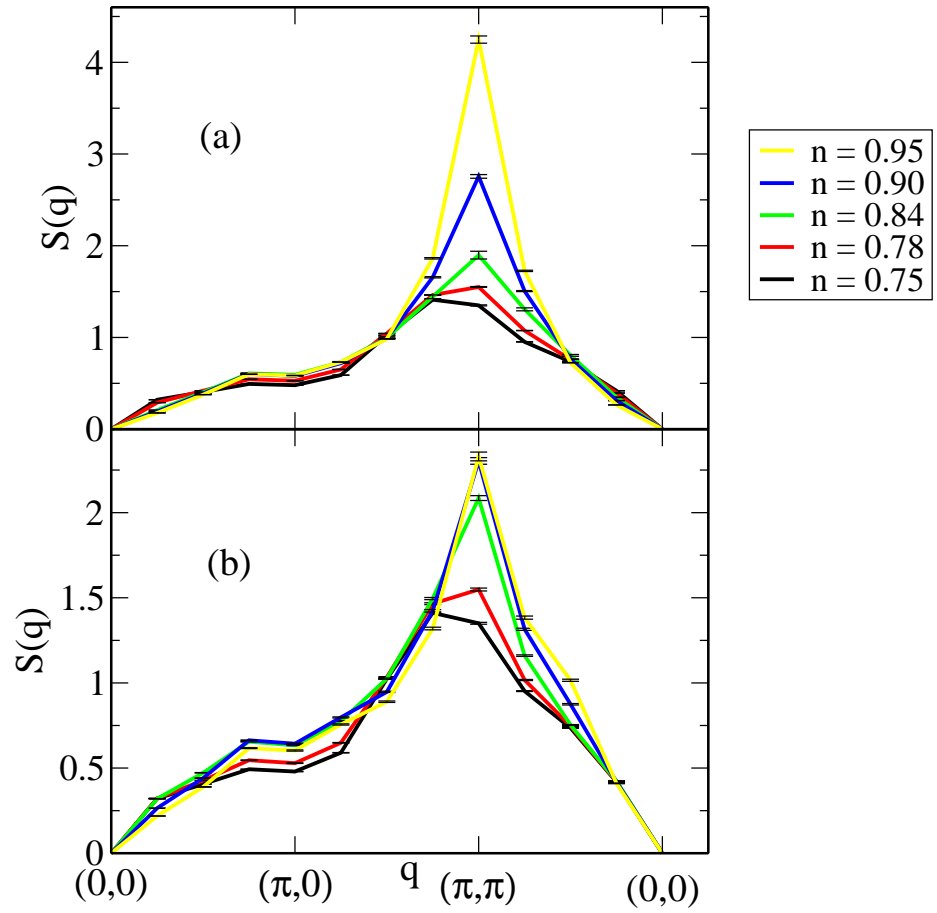


Figure 4.19: Magnetic structure factor as a function of the momentum-transfer for various densities. (a): Refined wave function with the BCS mean-field ground state. (b): Refined wave function with the Fermi sea as mean-field ground state ($\Delta = 0$).

Chapter 5

Relevance for high- T_c cuprates

It is now time to discuss the relevance of our findings for layered cuprates, in order to establish whether the two-dimensional Hubbard model can be considered as a minimal model for these materials.

Experimentally we have already seen that the parent compounds of the cuprates are antiferromagnetic insulators (see Fig. 1.5) at low temperature. The addition of about 4% of holes is enough to destroy the antiferromagnetic order and the superconducting dome emerges in the range of doping $0.05 < x < 0.25$. In our study, the ground state of the Hubbard model with nearest-neighbor hopping has a dominant antiferromagnetic instability at half-filling. Although results at moderate doping could not be obtained for the antiferromagnetic refined wave function due to the sign problem, it is reasonable to consider that the condensation energy per site decreases together with the magnetization when holes are introduced in the system. The difference between superconducting and antiferromagnetic condensation energy being rather small (Fig. 4.12), the superconducting instability is therefore expected to dominate for only a few percent doping. The possibility of a phase where both instabilities coexist has not been investigated, but our results suggest that such phase could exist, as in the case of the Gutzwiller ansatz [36]. This is in contradiction with the phase diagram of the cuprates where antiferromagnetic and superconducting phases are well separated. Two reasons can be given for this discrepancy. First our delocalized trial state is not particularly appropriate close to the half-filled system where the ground state of the Hubbard model is believed to be composed of itinerant holes in a background of localized electrons, as shown by the crossover (Fig. 4.2). The second reason is that the screening of the Coulomb repulsion is not very effective in the pseudogap region and it means that the long-range part of the interaction could have an influence at small doping. If this is true, a quantitative description of the cuprates should include a long-range repulsion in the microscopic model. The superconductivity disappears already at $x \approx 0.18$, earlier than observed experimentally. However the addition of the next-nearest-neighbor hopping improves considerably the agreement between our theory and the observed phase diagram, as the dome is

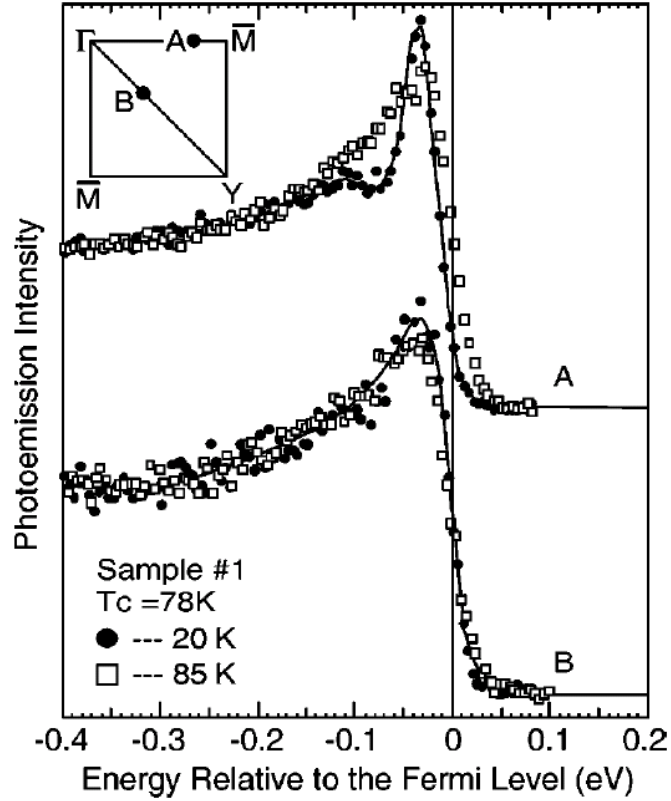


Figure 5.1: Photoemission spectra from a slightly underdoped compound of Bi2212, above and below the critical temperature. The A curves are measurements in the antinodal region of the Brillouin zone, whereas the B curves correspond to the nodal region. From [50].

extended up to $x \approx 0.25$.

5.1 Gap parameter

We have to mention here that our parameter Δ is just a variational parameter related to the pairing and it is not straightforward to identify it with the superconducting gap observed in experiments. However it is interesting to note that there is a good agreement of these two quantities.

The superconducting gap can be obtained using angle-resolved photoemission spectroscopy, which allows us to probe directly the single-particle spectral function $A(\vec{k}, \omega)$ by measuring the momentum and energy dependence of the intensity of the emitted photo-electrons. In Fig. 5.1, typical photoemission spectra are given for two different momenta in the Brillouin zone, above and below the critical temperature. At the point A of the Brillouin zone, located in the antinodal region, a clear evolution

is observed from a typical lineshape for the normal phase when the temperature is above T_c , to a typical lineshape for the superconducting state below T_c . At the same time, a shift of the leading edge occurs due to the opening of the superconducting gap. On the other hand, almost nothing changes in the nodal region (B point) above and below T_c . This reflects clearly the d -wave character of the superconducting gap and the shift allows us to estimate the absolute value of the gap. It turns out that this gap can vary appreciably in the family of the cuprates, from $\Delta = 10 - 20$ meV for the mono-layer compounds (LSCO [51] or Bi2201 [8]) to $\Delta = 30 - 40$ meV for the three-layer compounds (Bi2223 [8]) when measured at optimal doping. In our variational study, the hole concentration where the superconducting order parameter is maximal defines the optimal doping, that is $x \approx 0.1$ for the nearest-neighbor hopping and $x \approx 0.16$ when the next-nearest-neighbor hopping is added. For these values, the gap parameter is $\Delta = 40$ meV and $\Delta = 15$ meV respectively, if the hopping parameter is fixed to the value extracted from neutron scattering data $t = 300$ meV (see Chapter 1 and [10]). As a single CuO_2 plane is considered in our model, we see that again the inclusion of a t' parameter leads to a very good agreement with experimental data.

5.2 Condensation energy

Experimentally, an estimate of the condensation energy can be obtained from specific heat data. Indeed, general principles of thermodynamics allow us to write the variation of the internal energy of the system between temperatures T_1 and T_2 as the integrated specific heat:

$$\Delta U = \int_{T_1}^{T_2} dT C(T) . \quad (5.1)$$

Now, the condensation energy corresponds just to the change of the internal energy between the normal phase and the superconducting phase: $E_{cond} = U_N - U_{SC}$. Therefore, it can be extracted from the knowledge of the specific heat in both phases. Practically the procedure consists in isolating a sample in a calorimeter and in measuring the total specific heat as a function of temperature. A strong magnetic field (≈ 14 T) is then applied to prevent the superconducting transition and a second measure is carried out. The curves obtained for a $\text{HgBa}_2\text{CuO}_4$ compound [52] at optimal doping are shown in Fig. 5.2 (a). If we assume that superconductivity is induced by electronic correlations alone, the curve in the normal phase (at 14 T) can be interpreted as a phonon background which has to be subtracted. The difference between both measurements is therefore the contribution of the electrons which form Cooper pairs and condense in the superconducting phase. A clear signature of the transition is observed in part (b) of Fig. 5.2. The condensation energy is finally computed from this electronic contribution using equation 5.1. A major difficulty of this technique

is that a magnetic field that would be strong enough to kill completely the superconductivity cannot be reached and even if it would be possible, it would be hard to say to which extent the preformed pairs are also suppressed. The contribution of the electrons is therefore surely underestimated and the condensation energy has to be taken as a lower bound. The typical values measured for the cuprates at optimal doping are between 0.1 to 0.3 meV per copper [52],[53].

In our study, the condensation energy is about 1.5 meV per site at optimal doping (or 1.2 meV with next-nearest-neighbor hopping), that is at least 5 times larger than the experimental value. It is actually very hard to evaluate whether this difference can be explained by the presence of pairing correlations far above the critical temperature that are not destroyed by the magnetic field and therefore not included in the experimental condensation energy.

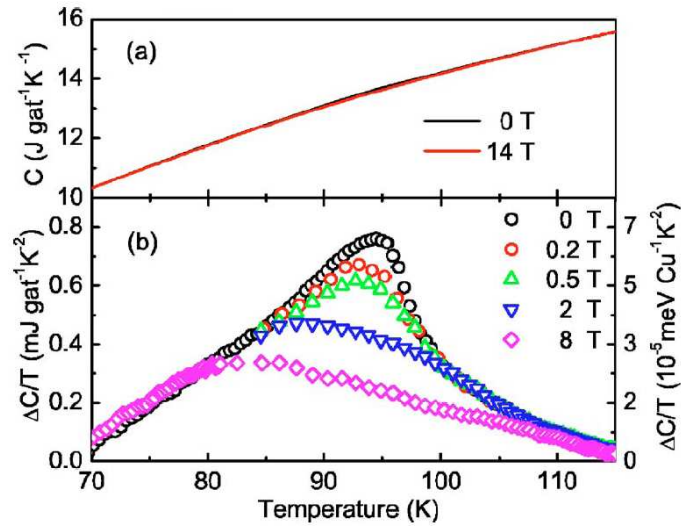


Figure 5.2: (a): Specific heat for optimally doped $\text{HgBa}_2\text{CuO}_{4+\delta}$ in a magnetic field of 0 T and 14 T. (b): Difference of the specific heat data $\Delta C/T = (C(B, T) - C(14 \text{ T}, T))/T$ for various magnetic fields B . The black curve is used for estimating the condensation energy. From [52].

5.3 Kinetic energy

The kinetic energy is more difficult to be measured, but it is possible to estimate it from optical spectroscopy measurement. The total spectral weight of the optical conductivity, A , is related by the frequency sum rule to the total density and the bare

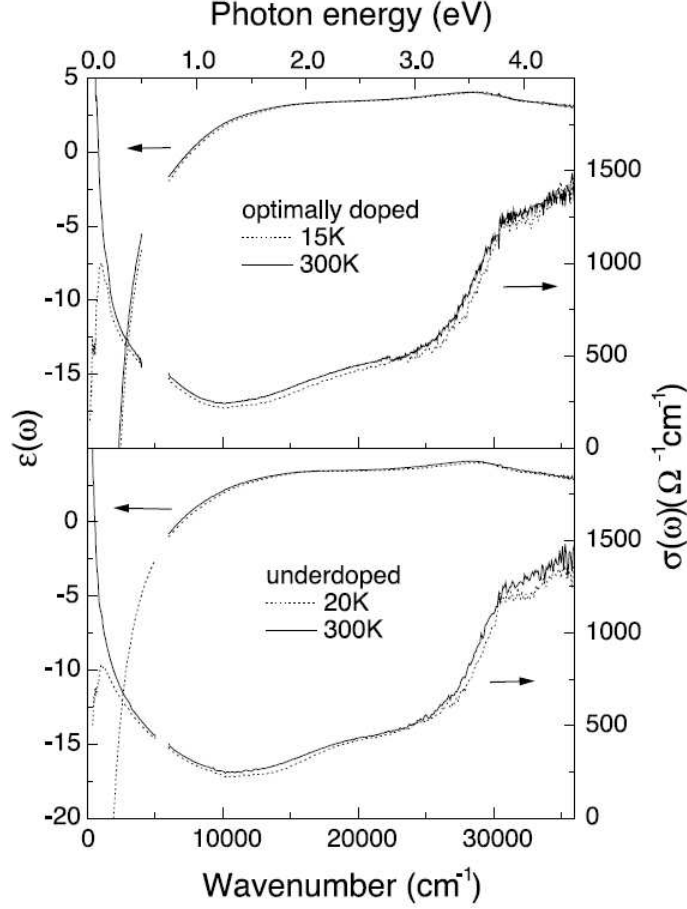


Figure 5.3: Spectroscopic ellipsometry data for an optimally doped (up) or a slightly underdoped (down) $\text{Bi}_2\text{Sr}_2\text{CaCu}_2\text{O}_{8-\delta}$ compound. The real part of the dielectric function and the optical conductivity are given as a function of the photon energy, above and below the critical temperature. From [54].

mass of the electrons. This sum rule is written:

$$A = \int_0^\infty \sigma(\omega) d\omega = \frac{\pi n e^2}{2m} \quad (5.2)$$

where $-e$ is the electron charge. In this spectral weight, all possible transitions of the electrons in all orbitals in the solid are involved. The optical conductivity can be separated into three parts: a delta peak at zero energy due to the condensate that can flow without dissipation, a contribution σ_1 due to low energy transitions arising from a single band crossing the Fermi surface and a contribution σ_h due to the interband transitions involving higher energy transitions. This decomposition leads to the definition of a spectral weight A_{1+D} for the two first contributions, which

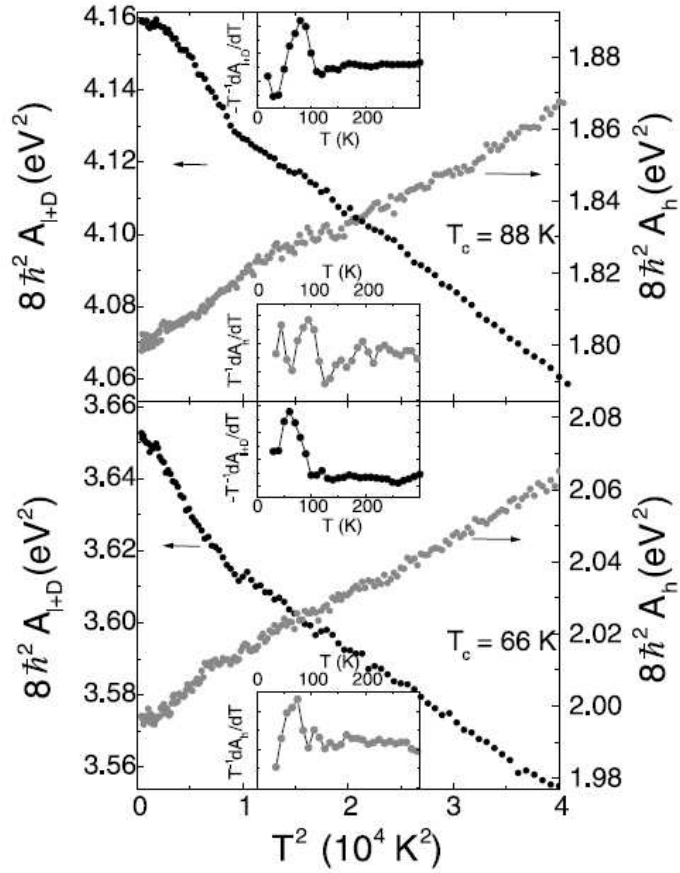


Figure 5.4: Temperature dependence of the spectral weights A_{1+D} and A_h for an optimally doped (up) or a slightly underdoped (down) $\text{Bi}_2\text{Sr}_2\text{CaCu}_2\text{O}_{8-\delta}$ compound. The insets give the derivatives of these weights divided by the temperature. From [54].

is obtained by integrating the conductivity between zero and a cutoff Ω separating the energy for intraband and interband transitions, and to the definition of a spectral weight A_h for the interband transitions, which is given by the conductivity integrated between Ω and infinity. Therefore we have

$$\begin{aligned}
 \sigma(\omega) &= D\delta(\omega) + \sigma_1(\omega) + \sigma_h(\omega) , \\
 A_{1+D} &= \int_0^\Omega \sigma(\omega) d\omega , \\
 A_h &= \int_\Omega^\infty \sigma(\omega) d\omega ,
 \end{aligned} \tag{5.3}$$

where D is the spectral weight of the condensate. By considering the single-band Hubbard model with nearest-neighbor hopping, a restricted sum rule which relates

now the spectral weight of the intraband transitions to the expectation value of the kinetic term of the Hamiltonian can be obtained [55]:

$$A_{1+D} = \frac{\pi e^2 a^2}{2\hbar^2 V} \langle -\hat{T} \rangle . \quad (5.4)$$

This relation allows us to extract the kinetic energy from a measurement of the optical conductivity. The complex dielectric function can be measured by spectroscopic ellipsometry. In Fig. 5.3, the real part of this function and the optical conductivity, which is directly related to the imaginary part, are given as a function of the photon energy above and below the critical temperature. The cutoff Ω is defined as the energy where the optical conductivity is minimal, at about 1.2 eV. The conductivity is found to decrease at all photon energy when the temperature is lowered below T_c , both at optimal doping and for an underdoped compound. This decrease corresponds to a transfer of spectral weight to the zero-energy delta peak, and hence, from A_h to A_{1+D} . This transfer is clearly seen in Fig. 5.4 where the spectral weights A_{1+D} and A_h are plotted as a function of the squared temperature. A_{1+D} increases almost like T^2 decreases in the normal phase and even faster below the critical temperature. The corresponding decrease is observed for A_h . By extrapolating the T^2 behavior in the normal state until $T = 0$ and using this restricted sum rule (5.4), we can estimate the kinetic energy variation due to the superconducting instability. What is typically found for the cuprates near optimal doping is a gain of about 0.5–1.0 meV per copper [52],[54]. It means that in the cuprates, the condensation energy could result from a lowering of the kinetic energy. That is precisely what is obtained with our refined wave function at optimal doping: a kinetic energy gain of about 1.1 meV ($t' = 0$) or 1.6 meV ($t' \neq 0$) per copper.

5.4 Spin-spin correlations

Neutron scattering experiments provide an efficient way to probe the dynamical spin susceptibility $\chi''(\vec{q}, \omega)$, which is directly related to the spin-spin correlation function in momentum-frequency space $S(\vec{q}, \omega)$ [56]. Therefore the magnetic structure factor $S(\vec{q})$ is readily obtained by integrating over the frequency. The results obtained in [56] for a $\text{YBa}_2\text{Cu}_3\text{O}_{6+\delta}$ compound are given in Fig. 5.5 as a function of the oxygen content δ . The addition of the oxygen atoms in the copper chains of the insulating layers removes some electrons from the CuO_2 plane. However this process is not exactly stoichiometric and the doping level of the CuO_2 plane is more easily defined by looking at the critical temperature (Fig. 5.5(a)). The superconducting dome begins at $\delta = 0.34$, whereas the optimal doping is approximately reached at $\delta = 1.0$. The structure factor extracted from neutron scattering data is peaked at $\vec{q} = (\pi, \pi)$ for all samples (underdoped or optimally doped). The doping dependence of the peak value is shown in Fig. 5.5(b). The large uncertainties do not allow us to

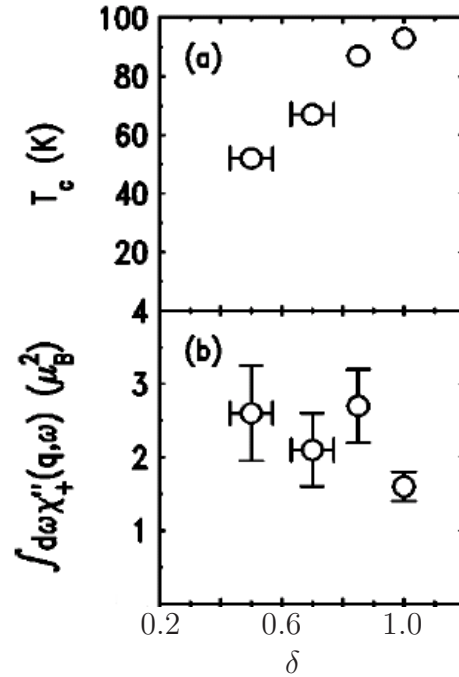


Figure 5.5: Neutron scattering data for a $\text{YBa}_2\text{Cu}_3\text{O}_{6+\delta}$ compound as a function of the oxygen content. The doping level is defined by the measure of the critical temperature in (a). (b): Peak values of the magnetic structure factor obtained by integrating the spin-spin correlation function over the energy. From [56].

make an accurate comparison with our results. Nevertheless, the experimental data indicate that the antiferromagnetic peak increases when the doping decreases. Taking into account the error bars and assuming a linear dependence, an extrapolation allows us to estimate a ratio of about 2 between the values at $x = 0.05$ (or $\delta = 0.34$) and at $x = 0.16$ ($\delta = 1.0$). This ratio is in good agreement with our values 2.5 for $t' = 0$ and 2.2 for $t' = -0.3t$.

The comparison of many properties of the refined variational ground state of the two-dimensional Hubbard model with experimental data obtained for the high- T_c cuprates shows an amazingly good agreement, especially when the next-nearest-neighbor hopping is included. Unfortunately the dynamical properties cannot be studied straightforwardly using our variational method, as they are associated with excitations of the system. Therefore the question remains open whether this model is able to describe all the unusual features occurring in the cuprates, like the pseudogap. However, our results give a strong indication that the superconductivity could originate from electronic correlations alone.

Chapter 6

Summary and conclusions

In this thesis, the ground state of the two-dimensional repulsive Hubbard model has been investigated for an intermediate value of the Coulomb parameter U . In particular, we have studied the possibility of an antiferromagnetic instability at half-filling and of a superconducting instability at moderate doping. As the appearance of pairing in a purely repulsive model is clearly a question of strong correlations, calculations have therefore to go beyond the mean-field level.

The particular choice of instabilities is motivated by the results obtained in the weak coupling limit within the frame of a renormalization group approach, which is able to treat the various competing singularities occurring in a Fermi system on an equal footing. At a one-loop level approximation, both antiferromagnetic and d -wave superconductivity are relevant at half-filling, but the antiferromagnetic susceptibility diverges more rapidly than the superconducting ones. When the system is gradually doped, the antiferromagnetic correlations loose more and more strength and the superconducting instability becomes dominant. Finally, the antiferromagnetic instability ceases to be relevant at a density that is associated in [18] with optimal doping. The energy scale defined by the cutoff where the susceptibilities diverge can be identified with a critical temperature T_c^{RG} . If the self-energy corrections, which are not taken into account at one-loop, are not too strong, T_c^{RG} corresponds to a phase transition. This is the case at optimal doping where the Fermi surface is no longer nested. The superconducting transition for $U = t$ occurs at $T_c^{RG} \approx 0.005t$ (which means about 16 K for $t = 300$ meV) at optimal doping.

The opposite limit, $U \rightarrow \infty$, is well known at half-filling where the Hamiltonian is reduced to the Heisenberg model. The spin-wave theory gives a nice description of the antiferromagnetic ground state and of the excited states of this model. Upon doping, the hopping of holes makes the (t-J) model much more complicated. However, Variational Monte Carlo simulations indicate that a pairing instability with d -wave symmetry occurs in the ground state. In order to give an idea about the transition temperature, the BCS relation between the ground state gap parameter and the critical temperature $2\Delta/k_B T_c \approx 3.5$ can be used. For $J \approx 100$ meV ($U = 12t$,

$t = 300$ meV) and at optimal doping, it gives $T_c^{tJ} \approx 286$ K.

The coupling regime which is appropriate for the cuprates is neither the weak nor the strong, but rather the intermediate interaction regime, as indicated by fits of neutron scattering data. The study of the pairing vertex by quantum Monte Carlo simulation allows one to identify the exchange of antiferromagnetic spin fluctuation as a possible candidate for the explanation of the mechanism leading to an effective attraction between nearest-neighbor sites in the repulsive Hubbard model. However within this technique, the low-temperature susceptibilities can be computed only in the half-filled case, where an antiferromagnetic phase is found. At moderate doping, a sign problem restricts the calculations to rather high temperatures and a superconducting transition is not observed. This problem does not occur in the cluster dynamical mean-field theory. Although a small number of degrees of freedom are taken into account, this approach offers the advantage to achieve the thermodynamic limit. By computing the susceptibilities as functions of temperature, a phase diagram for the Hubbard model with $U = 8t$ can be drawn, displaying an antiferromagnetic phase at half-filling and a superconducting dome at moderate doping. The critical temperature at optimal doping is $T_c^{CDMFT} \approx 220$ K.

The variational Monte Carlo method is the approach we have chosen in this thesis. Contrary to the cluster dynamical mean-field theory, finite systems are studied here but all the degrees of freedom are treated explicitly and no approximation is needed to compute the variational energy. A first possible choice for the trial state is a Gutzwiller ansatz together with a broken symmetry reference state. When pairing is allowed, a superconducting instability is stabilized only at half-filling or for small hole concentration. The superconductivity is driven in this case by the Coulomb term of the Hubbard model. However, the reliability of the variational approach depends on the quality of the variational wave function and we have shown that the Gutzwiller ansatz does not provide a variational ground state which is close enough to the exact ground state. More accurately, the condensation energy obtained with the Gutzwiller ansatz is much smaller than the difference between the variational and the exact energy of the ground state. It means that an improvement of the variational energy can lead to completely different conclusions. We have introduced a refined variational wave function which is very close to the exact ground state, as confirmed by the comparison with an exactly solvable model in one dimension or with results obtained by exact diagonalization for small clusters in two dimensions. When a superconducting instability is considered, a finite gap parameter is obtained in the range of doping $0 \leq x \lesssim 0.18$, associated with a finite pairing in the ground state. The corresponding order parameter forms a dome with a maximal value at $x \approx 0.1$. The comparison with an antiferromagnetic instability shows that antiferromagnetism is dominant at half-filling. However the antiferromagnetic order is expected to be destroyed very fast when the hole concentration is increased and therefore, the superconductivity becomes dominant upon doping. The refinement of the variational ground state leads to quantitative and qualitative changes in the properties of this state. In particular,

the superconductivity is now driven by the kinetic term of the Hamiltonian. A reason to believe that these results are reliable is that contrary to the Gutzwiller ansatz, the condensation energy ($E_{cond} \approx 0.005t$ at $n = 0.9$) is now of the same order as the error with respect to the exact ground state ($E_{var} - E_{ex} \approx 0.007t$), as estimated from the exact calculation for small clusters. Moreover, the size dependence of our results indicates that no major changes will occur for larger system sizes, presently out of reach for this type of variational wave function. The critical temperature at optimal doping, that is calculated with the BCS relation, is $T_c^{VMC} = 219$ K, in good agreement with the critical temperature obtained within CDMFT.

The main motivation for this study was to clarify whether or not the single-band Hubbard model could describe the electronic properties of the high- T_c compounds. The comparison of our results with the experimental data on the layered cuprates has revealed that there is an amazingly good agreement for several measured quantities. The addition in the model of the hopping between next-nearest-neighbor sites still improves the correspondence, as the range of dopings where the superconductivity occurs is extended up to $x \approx 0.25$, with an optimal doping at $x = 0.15$. The next-nearest-neighbor hopping also decreases the critical temperature to $T_c^{VMC} = 86$ K, a value which seems to be quite reasonable for the cuprates.

To conclude, this thesis has shown that all the key features of the cuprates are also present in the ground state of the two-dimensional repulsive Hubbard model, namely antiferromagnetism at half-filling and superconductivity in a range of doping $0 < x < 0.25$. This model can therefore serve as a minimal model for the layered cuprates.

Bibliography

- [1] J. G. Bednorz and K. A. Müller. *Z. Phys. B: Condens. Matter*, 64:189, 1986.
- [2] L. F. Mattheiss. *Phys. Rev. Lett.*, 58:1028, 1987.
- [3] J. Zaanen, G. A. Sawatzky, and J. W. Allen. *Phys. Rev. Lett.*, 55:418, 1985.
- [4] P. W. Anderson. *Phys. Rev.*, 115:2, 1959.
- [5] G. Shirane, Y. Endoh, R. J. Birgeneau, M. A. Kastner, Y. Hidaka, M. Oda, M. Suzuki, and T. Murakami. *Phys. Rev. Lett.*, 59:1613, 1987.
- [6] M. A. Kastner, R. J. Birgeneau, G. Shirane, and Y. Endoh. *Rev. Mod. Phys.*, 70:897, 1998.
- [7] D. L. Feng, A. Damascelli, K. M. Shen, N. Motoyama, D. H. Lu, H. Eisaki, K. Shimizu, J.-i. Shimoyama, K. Kishio, N. Kaneko, M. Greven, G. D. Gu, X. J. Zhou, C. Kim, F. Ronning, N. P. Armitage, and Z.-X. Shen. *Phys. Rev. Lett.*, 88:107001, 2002.
- [8] A. Damascelli, Z. Hussain, and Z.-X. Shen. *Rev. Mod. Phys.*, 75:473, 2003.
- [9] F. C. Zhang and T. M. Rice. *Phys. Rev. B*, 37:3759, 1988.
- [10] R. Coldea, S. M. Hayden, G. Aeppli, T. G. Perring, C. D. Frost, T. E. Mason, S.-W. Cheong, and Z. Fisk. *Phys. Rev. Lett.*, 86:5377, 2001.
- [11] P. W. Anderson. *J. Phys. Chem. Solids*, 11:26, 1959.
- [12] J. von Delft. *Ann. Phys. (Leipzig)*, 10:219, 2001.
- [13] J. Dukelsky, S. Pittel, and G. Sierra. *Rev. Mod. Phys.*, 76:643, 2004.
- [14] W. Kohn and J. M. Luttinger. *Phys. Rev. Lett.*, 15:524, 1965.
- [15] A. V. Chubukov. *Phys. Rev. B*, 48:1097, 1993.
- [16] R. Shankar. *Rev. Mod. Phys.*, 66:129, 1994.

-
- [17] C. J. Halboth and W. Metzner. *Phys. Rev. B*, 61:7364, 2000.
 - [18] D. Zanchi and H. J. Schulz. *Phys. Rev. B*, 61:13609, 2000.
 - [19] P. Fazekas. *Lecture Notes on Electron Correlation and Magnetism*, volume 5 of *Series in Modern Condensed Matter Physics*. World Scientific, 1999.
 - [20] P. W. Anderson. *Science*, 235:1196, 1987.
 - [21] W. Krauth. *Statistical Mechanics: Algorithms and Computations*. Oxford University Press, 2006.
 - [22] C. Gros. *Phys. Rev. B*, 38:931, 1988.
 - [23] A. Paramekanti, M. Randeria, and N. Trivedi. *Phys. Rev. B*, 70:054504, 2004.
 - [24] C. Gros, R. Joynt, and T. M. Rice. *Z. Phys. B*, 68:425, 1987.
 - [25] R. Blankenbecler, D. J. Scalapino, and R. L. Sugar. *Phys. Rev. D*, 24:2278, 1981.
 - [26] J. E. Hirsch. *Phys. Rev. B*, 31:4403, 1985.
 - [27] S. R. White, D. J. Scalapino, R. L. Sugar, E. Y. Loh, J. E. Gubernatis, and R. T. Scalettar. *Phys. Rev. B*, 40:506, 1989.
 - [28] E. Dagotto. *Rev. Mod. Phys.*, 66:763, 1994.
 - [29] N. Bulut, D. J. Scalapino, and S. R. White. *Phys. Rev. B*, 50:9623, 1994.
 - [30] M. H. Hettler, M. Mukherjee, M. Jarrell, and H. R. Krishnamurthy. *Phys. Rev. B*, 61:12739, 2000.
 - [31] Th. A. Maier, M. Jarrell, T. Pruschke, and M. H. Hettler. *Rev. Mod. Phys.*, 77:1027, 2005.
 - [32] J. E. Hirsch and R. M. Fye. *Phys. Rev. Lett.*, 56:2521, 1986.
 - [33] M. Jarrell, Th. A. Maier, M. H. Hettler, and A. N. Tahvildarzadeh. *Europhys. Lett.*, 56:563, 2001.
 - [34] K. Haule and G. Kotliar. *Phys. Rev. B*, 76:104509, 2007.
 - [35] G. Polatsek and K. W. Becker. *Phys. Rev. B*, 54:1637, 1996.
 - [36] T. Giamarchi and C. Lhuillier. *Phys. Rev. B*, 43:12943, 1991.
 - [37] H. Yokoyama, Y. Tanaka, M. Ogata, and H. Tsuchiura. *J. Phys. Soc. Jpn.*, 73:1119, 2004.

- [38] M. Dzierzawa, D. Baeriswyl, and M. Di Stasio. *Phys. Rev. B*, 51:1993, 1995.
- [39] F. Gebhard and A. E. Ruckenstein. *Phys. Rev. Lett.*, 68:244, 1992.
- [40] M. Dzierzawa, D. Baeriswyl, and L. M. Martelo. *Helv. Phys. Acta*, 70:124, 1997.
- [41] L. M. Martelo, M. Dzierzawa, L. Siffert, and D. Baeriswyl. *Z. Phys. B*, 103:335, 1997.
- [42] S. Sorella and E. Tosatti. *Europhys. Lett.*, 19:699, 1992.
- [43] H. Otsuka. *J. Phys. Soc. Jpn.*, 61:1645, 1991.
- [44] J. E. Hirsch. *Phys. Rev. B*, 28:4059, 1983.
- [45] H. Yokoyama and H. Shiba. *J. Phys. Soc. Jpn.*, 56:3582, 1987.
- [46] A. W. Sandvik. *Phys. Rev. B*, 56:11678, 1997.
- [47] D. Ceperley, G. V. Chester, and K. H. Kalos. *Phys. Rev. B*, 16:3081, 1977.
- [48] C. J. Umrigar, K. G. Wilson, and J. W. Wilkins. *Phys. Rev. Lett.*, 60:1719, 1988.
- [49] D. Baeriswyl, D. Eichenberger, and B. Gut. *phys. stat. sol. (b)*, 244:2299, 2007.
- [50] Z.-X. Shen, D. S. Dessau, B. O. Wells, D. M. King, W. E. Spicer, A. J. Arko, D. Marshall, L. W. Lombardo, A. Kapitulnik, P. Dickinson, S. Doniach, J. Di-Carlo, T. Loeser, and C. H. Park. *Phys. Rev. Lett.*, 70:1553, 1993.
- [51] K. Yamada, S. Wakimoto, G. Shirane, C. H. Lee, M. A. Kastner, S. Hosoya, M. Greven, Y. Endoh, and R. J. Birgeneau. *Phys. Rev. Lett.*, 75:1626, 1995.
- [52] E. van Heumen, R. Lortz, A. B. Kuzmenko, F. Carbone, D. van der Marel, X. Zhao, G. Yu, Y. Cho, N. Barisic, M. Greven, C. C. Homes, and S. V. Dordevic. *Phys. Rev. B*, 75:054522, 2007.
- [53] J. W. Loram, J. L. Luo, J. R. Cooper, W. Y. Liang, and J. L. Tallon. *Physica C*, 341:831, 2000.
- [54] H. J. A. Molegraaf, C. Presura, D. van der Marel, P. H. Kes, and M. Li. *Science*, 295:2239, 2002.
- [55] D. Baeriswyl and L. Degiorgi. *Strong Interactions in Low Dimensions*, volume 25 of *Physics and Chemistry of Materials with Low-Dimensional Structures*. Kluwer Academic Publishers, 2004.
- [56] H. F. Fong, P. Bourges, Y. Sidis, L. P. Regnault, J. Bossy, A. Ivanov, D. L. Milius, I. A. Aksay, and B. Keimer. *Phys. Rev. B*, 61:14773, 2000.

Appendix A

Three-band Hamiltonian

In this appendix, the insulating character of the parent compound of the cuprates is explained by including the strong electronic correlations in the three-band model describing the CuO_2 plane. The Hamiltonian can be written:

$$\begin{aligned}
\hat{H} = & t_{pd} \sum_{\vec{R}, \alpha, \sigma} (d_{\vec{R}, \sigma}^\dagger p_{\vec{R}, \alpha, \sigma} + p_{\vec{R}, \alpha, \sigma}^\dagger d_{\vec{R}, \sigma}) + \epsilon_p \sum_{\vec{R}, \alpha} (n_{p\vec{R}, \alpha} - 1) + \epsilon_d \sum_{\vec{R}} (n_{d\vec{R}} - 1) \\
& + U_{pp} \sum_{\vec{R}, \alpha} (n_{p\vec{R}, \alpha\uparrow} - \frac{1}{2})(n_{p\vec{R}, \alpha\downarrow} - \frac{1}{2}) + U_{dd} \sum_{\vec{R}} (n_{d\vec{R}\uparrow} - \frac{1}{2})(n_{d\vec{R}\downarrow} - \frac{1}{2}) \\
& + V_{pd} \sum_{\vec{R}, \alpha} (n_{d\vec{R}} - 1)(n_{p\vec{R}, \alpha} - 1)
\end{aligned} \tag{A.1}$$

Here the operator $d_{\vec{R}, \sigma}^\dagger$ ($p_{\vec{R}, \alpha, \sigma}^\dagger$) creates an electron in the d- (p_α -) orbital of the cell defined by the vector \vec{R} , $n_{s\vec{R}\sigma} = s_{\vec{R}, \sigma}^\dagger s_{\vec{R}, \sigma}$ ($s = d$ or p_α) and $n = n_\uparrow + n_\downarrow$. The on-site repulsion on the oxygen (parameter U_{pp}) or copper (U_{dd}) sites as well as a nearest-neighbor interaction (V_{pd}) are taken into account. The role of these strong correlations are more easily understood in the hole-picture and therefore the electron-hole transformations:

$$\begin{cases} d_{\vec{R}, \sigma} \rightarrow d_{\vec{R}, \sigma}^\dagger \\ p_{\vec{R}, \alpha, \sigma} \rightarrow -p_{\vec{R}, \alpha, \sigma}^\dagger \end{cases} \tag{A.2}$$

are applied. It implies $n_{d\vec{R}\sigma} \rightarrow 1 - n_{d\vec{R}\sigma}$, $n_{d\vec{R}} \rightarrow 2 - n_{d\vec{R}}$ and the corresponding transformation for the p-orbitals. It is straightforward to see that the hopping term or the interaction terms of the three-band Hamiltonian are invariant under these transformation, whereas the orbital occupation terms just change their sign. Therefore in

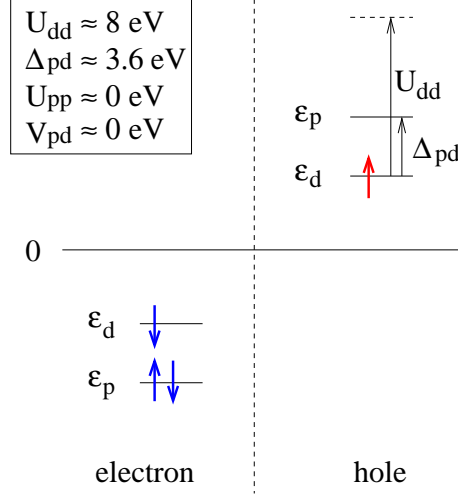


Figure A.1: Available states for $t_{pd} = 0$ eV. The left-hand side shows the electron-picture where only one electron is missing in the d-orbital. The corresponding situation in the hole-picture is depicted in the right-hand side. Reasonable values for the parameters of the three-band model are also given.

the hole-picture, the Hamiltonian has the form (A.1) with the parameters:

$$\begin{aligned}
 t_{pd} &\rightarrow t_{pd} & \epsilon_p &\rightarrow -\epsilon_p \\
 \epsilon_d &\rightarrow -\epsilon_d & U_{pp} &\rightarrow U_{pp} \\
 U_{dd} &\rightarrow U_{dd} & V_{pd} &\rightarrow V_{pd}
 \end{aligned} \tag{A.3}$$

Now the operator $d_{\vec{R},\sigma}^\dagger$ ($p_{\vec{R},\alpha,\sigma}^\dagger$) creates a hole in the d- (p_α -) orbital of the cell defined by the vector \vec{R} . The available states in the case of the cuprates are depicted in Figure A.1. In the electron-picture, the p-orbitals are completely filled and the d-orbital is half-filled. In the hole-picture, this corresponds to a single hole in the d-orbital. Due to the large on-site repulsion U_{dd} , the double occupation of a copper site costs a prohibitive energy and therefore a gap is opened in the density of states. Moreover, an additional hole will reside in a p-orbital of the oxygen site, with an energy $\epsilon_p + V_{pd} \approx \epsilon_d + \Delta_{pd}$ which is much smaller than the energy $\epsilon_d + U_{dd}$ necessary to occupy the d-orbital. As $U_{dd} > \Delta_{pd}$, the cuprates are referred to as charge-transfer insulators rather than Mott-insulators [3].

Appendix B

The BCS ground state

In this appendix we derive the BCS approximation (2.2) for the ground state of the Hamiltonian (2.1). We first rewrite the Hamiltonian in Fourier space, using the transformation

$$c_{i\sigma} = \frac{1}{L} \sum_{\vec{k}} e^{-i\vec{k} \cdot \vec{n}_i} c_{\vec{k}\sigma} , \quad (\text{B.1})$$

where $\vec{n}_i = (n_{ix}, n_{iy})$ are the vectors of the $L \times L$ square lattice (in units of the lattice constant) and the summation is restricted to the first Brillouin zone. We find

$$\hat{T} - \mu \hat{N} = \sum_{\vec{k}, \sigma} \xi_{\vec{k}} c_{\vec{k}\sigma}^\dagger c_{\vec{k}\sigma} \quad (\text{B.2})$$

where $\xi_{\vec{k}} = \epsilon_{\vec{k}} - \mu$, with $\epsilon_{\vec{k}} = -2t(\cos k_x + \cos k_y)$. The chemical potential μ is introduced to fix the average number of particles. The interaction term is given by

$$\begin{aligned} \hat{H}_{int} &= U \sum_i n_{i\uparrow} n_{i\downarrow} + V \sum_{\langle i, j \rangle} n_i n_j \\ &= \frac{U}{L^4} \sum_{\vec{k}_1, \dots, \vec{k}_4} c_{\vec{k}_1\uparrow}^\dagger c_{\vec{k}_2\uparrow} c_{\vec{k}_3\downarrow}^\dagger c_{\vec{k}_4\downarrow} \sum_{\vec{n}} e^{i(-\vec{k}_1 + \vec{k}_2 - \vec{k}_3 + \vec{k}_4) \cdot \vec{n}} \\ &+ \frac{V}{2L^4} \sum_{\substack{\vec{k}_1, \dots, \vec{k}_4 \\ \sigma\sigma'}} c_{\vec{k}_1\sigma}^\dagger c_{\vec{k}_2\sigma} c_{\vec{k}_3\sigma'}^\dagger c_{\vec{k}_4\sigma'} \sum_{\vec{n}} e^{i(-\vec{k}_1 + \vec{k}_2 - \vec{k}_3 + \vec{k}_4) \cdot \vec{n}} \\ &\quad \cdot 2 \left[\cos(k_{3x} - k_{4x}) + \cos(k_{3y} - k_{4y}) \right] \end{aligned}$$

$$\begin{aligned}
 = & \frac{1}{L^2} \sum_{\substack{\vec{k}_1, \dots, \vec{k}_4 \\ \sigma \sigma'}} c_{\vec{k}_1 \sigma}^\dagger c_{\vec{k}_2 \sigma} c_{\vec{k}_3 \sigma'}^\dagger c_{\vec{k}_4 \sigma'} \Delta(\vec{k}_1 - \vec{k}_2 + \vec{k}_3 - \vec{k}_4) \\
 & \cdot \underbrace{\left\{ \frac{U}{2} \delta_{\sigma, -\sigma'} + V \left[\cos(k_{3x} - k_{4x}) + \cos(k_{3y} - k_{4y}) \right] \right\}}_{W_{\sigma \sigma'}(\vec{k}_3, \vec{k}_4)} .
 \end{aligned} \tag{B.3}$$

In the BCS approximation the full Hamiltonian $\hat{H} = \hat{T} - \mu \hat{N} + \hat{H}_{int}$ is replaced by the mean-field Hamiltonian

$$\hat{H}_{BCS} = \sum_{\vec{k} \sigma} \xi_{\vec{k}} c_{\vec{k} \sigma}^\dagger c_{\vec{k} \sigma} - \sum_{\vec{k}} \Delta(\vec{k}) \left(c_{\vec{k} \uparrow}^\dagger c_{-\vec{k} \downarrow}^\dagger + c_{-\vec{k} \downarrow} c_{\vec{k} \uparrow} \right) . \tag{B.4}$$

Using the Bogoliubov transformation

$$\begin{aligned}
 c_{\vec{k} \uparrow}^\dagger &= u_{\vec{k}} \gamma_{\vec{k} \uparrow}^\dagger + v_{\vec{k}} \gamma_{-\vec{k} \downarrow} & u_{\vec{k}}, v_{\vec{k}} \text{ real and} \\
 c_{-\vec{k} \downarrow} &= u_{\vec{k}} \gamma_{-\vec{k} \downarrow} - v_{\vec{k}} \gamma_{\vec{k} \uparrow}^\dagger & u_{\vec{k}}^2 + v_{\vec{k}}^2 = 1,
 \end{aligned} \tag{B.5}$$

the BCS Hamiltonian reads:

$$\begin{aligned}
 \hat{H}_{BCS} &= E_0 + \sum_{\vec{k}, \sigma} \left[\xi_{\vec{k}} (u_{\vec{k}}^2 - v_{\vec{k}}^2) + 2u_{\vec{k}} v_{\vec{k}} \Delta(\vec{k}) \right] \gamma_{\vec{k} \sigma}^\dagger \gamma_{\vec{k} \sigma} \\
 &+ \sum_{\vec{k}} \left[2\xi_{\vec{k}} u_{\vec{k}} v_{\vec{k}} - \Delta(\vec{k}) (u_{\vec{k}}^2 - v_{\vec{k}}^2) \right] (\gamma_{\vec{k} \uparrow}^\dagger \gamma_{-\vec{k} \downarrow}^\dagger + \gamma_{-\vec{k} \downarrow} \gamma_{\vec{k} \uparrow}) .
 \end{aligned} \tag{B.6}$$

Therefore by choosing $u_{\vec{k}}, v_{\vec{k}}$ such that

$$2\xi_{\vec{k}} u_{\vec{k}} v_{\vec{k}} - \Delta(\vec{k}) (u_{\vec{k}}^2 - v_{\vec{k}}^2) = 0, \tag{B.7}$$

the Hamiltonian is diagonalized. The diagonal term defines the energy of a Bogoliubov quasiparticle:

$$\xi_{\vec{k}} (u_{\vec{k}}^2 - v_{\vec{k}}^2) + 2u_{\vec{k}} v_{\vec{k}} \Delta(\vec{k}) := E_{\vec{k}} . \tag{B.8}$$

Thus, using the condition (B.7) together with $u_{\vec{k}}^2 + v_{\vec{k}}^2 = 1$, the following relations can be obtained easily:

$$E_{\vec{k}} = \sqrt{\xi_{\vec{k}}^2 + \Delta_{\vec{k}}^2}, \quad u_{\vec{k}}^2 = \frac{1}{2} \left(1 + \frac{\xi_{\vec{k}}}{E_{\vec{k}}} \right), \quad v_{\vec{k}}^2 = \frac{1}{2} \left(1 - \frac{\xi_{\vec{k}}}{E_{\vec{k}}} \right), \quad u_{\vec{k}} v_{\vec{k}} = \frac{\Delta_{\vec{k}}}{2E_{\vec{k}}} . \tag{B.9}$$

In the diagonalized BCS Hamiltonian,

$$\hat{H}_{BCS} = E_0 + \sum_{\vec{k} \sigma} E_{\vec{k}} \gamma_{\vec{k} \sigma}^\dagger \gamma_{\vec{k} \sigma} , \tag{B.10}$$

$E_{\vec{k}}$ is a positive energy and therefore the ground state is the vacuum of quasiparticles:

$$|BCS\rangle = \prod_{\vec{k}} \gamma_{\vec{k}\uparrow} \gamma_{-\vec{k}\downarrow} |0\rangle, \quad (\text{B.11})$$

where $|0\rangle$ is the vacuum state for electrons. In term of electron operators, the BCS state has the familiar form:

$$|BCS\rangle = \prod_{\vec{k}} (u_{\vec{k}} + v_{\vec{k}} c_{\vec{k}\uparrow}^\dagger c_{-\vec{k}\downarrow}^\dagger) |0\rangle. \quad (\text{B.12})$$

Now the variational energy of our model (2.1) can be calculated using the BCS ansatz (B.11). The BCS state is already normalized and the variational energy is

$$\begin{aligned} E(\Delta_{\vec{k}}) &= \langle BCS | \hat{H} | BCS \rangle \\ &= \sum_{\vec{k}, \sigma} \epsilon_{\vec{k}} \langle c_{\vec{k}\sigma}^\dagger c_{\vec{k}\sigma} \rangle \\ &\quad + \frac{1}{L^2} \sum_{\substack{\vec{k}_1, \dots, \vec{k}_4 \\ \sigma \sigma'}} \langle c_{\vec{k}_1\sigma}^\dagger c_{\vec{k}_2\sigma} c_{\vec{k}_3\sigma'}^\dagger c_{\vec{k}_4\sigma'} \rangle \Delta(\vec{k}_1 - \vec{k}_2 + \vec{k}_3 - \vec{k}_4) W_{\sigma\sigma'}(\vec{k}_3, \vec{k}_4). \end{aligned}$$

Wick's theorem allows us to write:

$$\langle c_{\vec{k}_1\sigma}^\dagger c_{\vec{k}_2\sigma} c_{\vec{k}_3\sigma'}^\dagger c_{\vec{k}_4\sigma'} \rangle = \langle c_{\vec{k}_1\sigma}^\dagger c_{\vec{k}_2\sigma} \rangle \langle c_{\vec{k}_3\sigma'}^\dagger c_{\vec{k}_4\sigma'} \rangle + \langle c_{\vec{k}_1\sigma}^\dagger c_{\vec{k}_4\sigma'} \rangle \langle c_{\vec{k}_2\sigma} c_{\vec{k}_3\sigma'}^\dagger \rangle - \langle c_{\vec{k}_1\sigma}^\dagger c_{\vec{k}_3\sigma'}^\dagger \rangle \langle c_{\vec{k}_2\sigma} c_{\vec{k}_4\sigma'} \rangle$$

But these expectation values are easily derived using the Bogoliubov transformation (B.5) and the definition (B.11) of the BCS state. For instance:

$$\begin{aligned} \langle c_{\vec{k}\sigma}^\dagger c_{\vec{k}'\sigma'} \rangle &= \langle (u_{\vec{k}} \gamma_{\vec{k}\sigma}^\dagger \pm v_{\vec{k}} \gamma_{-\vec{k}-\sigma}) (u_{\vec{k}'} \gamma_{\vec{k}'\sigma'}^\dagger \pm v_{\vec{k}'} \gamma_{-\vec{k}'-\sigma'}) \rangle \\ &= v_{\vec{k}}^2 \delta_{\vec{k}, \vec{k}'} \delta_{\sigma, \sigma'}. \end{aligned} \quad (\text{B.13})$$

Here only the term $\langle \gamma \gamma^\dagger \rangle$ survives due to the fact that the BCS state is the vacuum of quasiparticles γ . The other expectation values are obtained in the same way:

$$\langle c_{\vec{k}\sigma} c_{\vec{k}'\sigma'}^\dagger \rangle = u_{\vec{k}}^2 \delta_{\vec{k}, \vec{k}'} \delta_{\sigma, \sigma'}, \quad \langle c_{\vec{k}\sigma}^\dagger c_{\vec{k}'\sigma'}^\dagger \rangle = \sigma u_{\vec{k}} v_{\vec{k}} \delta_{\vec{k}, -\vec{k}'} \delta_{\sigma, -\sigma'}, \quad \langle c_{\vec{k}\sigma} c_{\vec{k}'\sigma'} \rangle = -\sigma u_{\vec{k}} v_{\vec{k}} \delta_{\vec{k}, -\vec{k}'} \delta_{\sigma, -\sigma'}.$$

Inserting these relations into (B.13), the variational energy is finally given by:

$$\begin{aligned} E(\Delta_{\vec{k}}) &= 2 \sum_{\vec{k}} \epsilon_{\vec{k}} v_{\vec{k}}^2 + \frac{U + 8V}{L^2} \cdot \frac{N^2}{4} + \frac{1}{L^2} \sum_{\vec{k}_1, \vec{k}_2, \sigma} W_{\sigma\sigma}(\vec{k}_2, \vec{k}_1) v_{\vec{k}_1}^2 u_{\vec{k}_2}^2 \\ &\quad + \frac{1}{L^2} \sum_{\vec{k}_1, \vec{k}_2, \sigma} W_{\sigma-\sigma}(\vec{k}_1, \vec{k}_2) u_{\vec{k}_1} v_{\vec{k}_1} u_{\vec{k}_2} v_{\vec{k}_2} \end{aligned} \quad (\text{B.14})$$

In the second term, which is just the Hartree term, the average particle number $N = \sum_{\vec{k}, \sigma} \langle c_{\vec{k}\sigma}^\dagger c_{\vec{k}\sigma} \rangle = 2 \sum_{\vec{k}} v_{\vec{k}}^2$ has been introduced.

Appendix C

Kadanoff-Wilson-Polchinski renormalization group

In this appendix, the procedure leading to a flow equation for the renormalization of the two-particles vertex Γ_4 of the section 3.2 is briefly described.

The idea of the Kadanoff-Wilson-Polchinski formulation is to consider the reduction of the cutoff from an initial value Λ_0 equal to the bandwidth to a value Λ as an infinite set of infinitesimal transformations. If Λ is given by the renormalization parameter l : $\Lambda = \Lambda_0 e^{-l}$, then:

$$S_{\Lambda_0} \rightarrow S_{\Lambda_0 e^{-dl}}^{(1)} \rightarrow S_{\Lambda_0 e^{-2dl}}^{(2)} \rightarrow \dots \rightarrow S_{\Lambda_0 e^{-l}}' \quad (\text{C.1})$$

At each step, the modes inside a shell Λdl are eliminated (the on-shell modes). It gives:

$$S_{\Lambda(l+dl)} = S_{\Lambda(l)} + \delta S(l) \quad (\text{C.2})$$

Now $S_{\Lambda(l)}$ is the effective action where the fast modes ($|\xi_{\vec{k}}| > \Lambda(l)$) are already eliminated and $\delta S(l)$ is the correction due to the elimination of the on-shell modes. Following (3.11), all diagrams renormalizing a vertex at a given step, with slow modes as external legs and the on-shell modes as internal lines, are in principle contained in $\delta S(l)$. However, the shell of modes that are eliminated at this step has a size $d\Lambda$ and therefore each internal line, which is constrained to this shell, is proportional to dl . It means that diagrams with more than one internal line are of higher order in the infinitesimal parameter dl and they don't survive in $\delta S(l)$. Only two kind of diagrams are therefore involved in the renormalization of the vertex Γ_n (with n external legs): the tree and the loop diagrams. The renormalization of the two-point vertex at step l is given by the loop diagram of the four-point vertex (see Fig. C.1(a)). All other diagrams with two external legs contain more than one internal line. Of course, the renormalized four-point vertex at step l results itself from higher order diagrams created at previous steps. Actually, the first step of the renormalization creates the

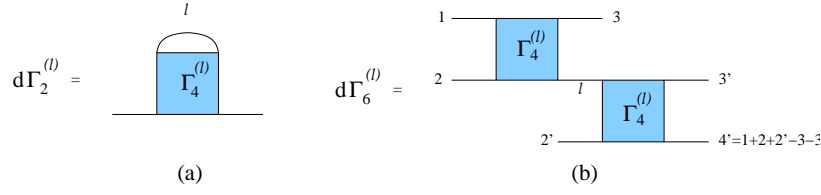


Figure C.1: (a) Loop diagram of the four-point vertex renormalizing the two-point vertex. (b) The 6-point vertex, which is not present in the bare action, appears during the renormalization process as the tree diagram of the 4-point vertex.

Γ_6 vertex from the tree diagram with two bare Γ_4 vertices (see Fig. C.1(b)) and gives the first self-energy correction for the two-point vertex. The second step creates some higher order vertices, renormalizes the four-point vertex by the loop diagrams of the Γ_6 vertex, and so on.

From this diagrammatic description, it is possible to write an exact flow equation for all vertices $\Gamma_n^{(l)}$, called the Polchinski flow equation. Practically, a truncation of the series (3.11) is needed in order to make the calculation manageable. The one-loop renormalization group consists in keeping terms up to quadratic order in the interaction coupling U . It is very easy to realize that all vertices of order higher than 6 are of order higher than 2 in U (they are created from tree diagrams with at least one Γ_6 vertex which is already of order U^2). Therefore $\Gamma_8 = \Gamma_{10} = \Gamma_{12} = \dots = 0$ in this approximation. Consequently, the only contribution for the Γ_6 vertex comes from the tree diagram of Figure C.1(b). The flow equations for Γ_2 and Γ_6 are (see Fig. C.1):

$$\begin{aligned} \frac{\partial}{\partial \Lambda_l} \Gamma_2^{(l)}(\vec{K}) &= -T \sum_{\omega'_n} \int_{d\Lambda} d^2 k' \Gamma_4^{(l)}(\vec{K}', \vec{K}, \vec{K}', \vec{K}) G_l(\vec{K}') \\ \frac{\partial}{\partial \Lambda_l} \Gamma_6^{(l)}(\vec{K}_1, \vec{K}_2, \vec{K}_3, \vec{K}_{2'}, \vec{K}_{3'}, \vec{K}_{4'}) &= T \sum_{\omega_n} \int_{d\Lambda} d^2 k \delta(\vec{k} - \vec{k}_1 - \vec{k}_2 + \vec{k}_3) \delta_{\omega_n - \omega_{n1} - \omega_{n2} + \omega_{n3}} \\ &\quad \cdot \Gamma_4^{(l)}(\vec{K}_1, \vec{K}_2, \vec{K}_3, -\vec{K}) \Gamma_4^{(l)}(\vec{K}, \vec{K}_{2'}, \vec{K}_{3'}, \vec{K}_{4'}) G_l(\vec{K}) \end{aligned}$$

Here $G_l(\vec{K}) = [\Gamma_2^{(l)}(\vec{K})]^{-1}$ is the one-particle propagator at step l , which is renormalized by the scattering from fast modes. The integration is over the momentum of the on-shell modes.

The flow of the four-point vertex gives the renormalization of the interaction ($\Gamma_4^{(l)} \equiv U_l$). It is constructed from the loop diagrams of the $\Gamma_6^{(l)}$ vertex. Five topologically different diagrams are obtained, depending on which legs are contracted to form the loop diagram (see Fig. C.2). This contraction is realized at the current step l , while the $\Gamma_6^{(l)}$ vertex has been created at a previous step l_{pp} or l_{ph} , which is

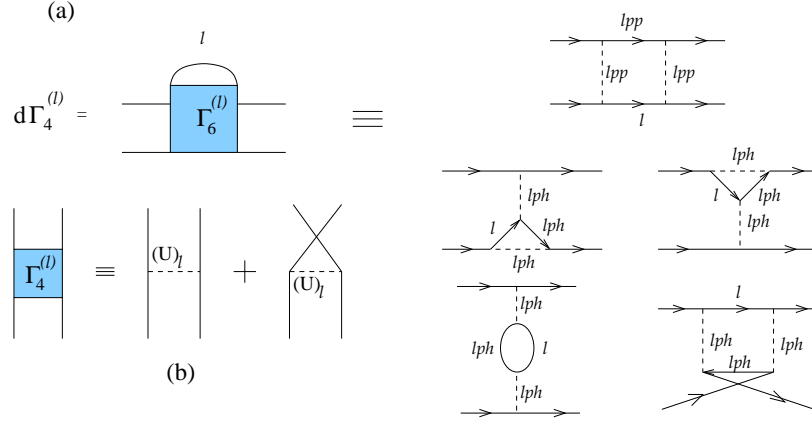


Figure C.2: (a) The renormalization of the 4-point vertex consists just in the loop diagram of the 6-point vertex. All other contributions are of higher order in U . Five diagrams are obtained depending on the legs that are contracted. (b) The effective 4-point vertex is composed of the direct interaction and of the exchange interaction.

given by momentum conservation. For instance, the first diagram of Figure C.2(a) is a particle-particle (pp) diagram obtained by contracting legs 2' and 3 of Figure C.1(b) at step l . If we write the total energy-momentum vector in the pp process as $\vec{K}_1 + \vec{K}_2 = \vec{Q}_{pp} \equiv (\omega_{npp}, \vec{q}_{pp})$ and the momentum shared by legs 2' and 3 as $\vec{K}_{2'} = \vec{K}_3 = \vec{K}$, then the momentum conservation for the $\Gamma_4^{(l_{pp})}$ gives $\vec{k}_4 = \vec{k}_{1'} = \vec{q}_{pp} - \vec{k}$. Therefore, the tree diagram of C.1(b) has been created at step l_{pp} , with:

$$l_{pp} = -\ln \frac{|\xi_{\vec{q}_{pp}-\vec{k}}|}{\Lambda_0} \quad (C.3)$$

This particle-particle term is also called “BCS” channel for the renormalization of the interaction. Other diagrams of Figure C.2(a) are particle-hole (ph) diagrams. We can see that the energy-momentum transfer is $\vec{Q}_{ph} = \vec{K}_1 - \vec{K}_3$ for the second, the third and the fourth diagrams which constitute the so-called zero-sound “ZS” channel and $\vec{Q}_{ph} = \vec{K}_1 - \vec{K}_4$ for the last diagram which is the ZS' channel. The step l_{ph} occurring in these diagrams is given by:

$$l_{ph} = -\ln \frac{|\xi_{\vec{q}_{ph}+\vec{k}}|}{\Lambda_0}. \quad (C.4)$$

Each diagram of Figure C.2(a) contributes to the flow equation for the effective interaction U_l . To illustrate how this equation is obtained, the pp contribution is written here. The flow equation is given by:

$$\frac{\partial U_l}{\partial l} = \beta\{U, U\} + \text{contributions of ph diagrams} \quad (C.5)$$

where:

$$\beta\{U, U\} = \Xi\{U, U\} + \Xi\{XU, XU\} \quad (\text{C.6})$$

β and Ξ are bilinear functionals of $U_{l_{pp}}$ with four arguments. The operator X is the exchange operator acting as $XF(1, 2, 3, 4) = F(2, 1, 3, 4)$. It allows to take into account the exchange interaction as indicated in Fig. C.2(b). Finally we have:

$$\begin{aligned} \Xi\{U, U\}(\vec{K}_1, \vec{K}_2, \vec{K}_3, \vec{K}_4) &= -T \sum_{\omega_n} \int_{d\Lambda} d^2k \Theta(|\xi_{\vec{k}-\vec{q}_{pp}}| - \Lambda_l) \\ &\cdot U_{l_{pp}}(\vec{K}_1, \vec{K}_2, \vec{K}) U_{l_{pp}}(\vec{K}_3, \vec{K}_4, \vec{K}) G_l(\vec{K}) G_{l_{pp}}(\vec{Q}_{pp} - \vec{K}) \end{aligned}$$

where $\Theta(|\xi_{\vec{k}-\vec{q}_{pp}}| - \Lambda_l)$ ensures that \vec{k} is such that the step l_{pp} comes before the step l . The ph diagrams add similar contributions to the flow equation.

Appendix D

Canonical ensemble

In this appendix the calculations of the expectation values of one- and two-body operators are detailed, using the form (4.18) for the antiferromagnetic wave function and the notations of Section 4.3.1. The aim is to compute the variational energy for the Hubbard model

$$\langle \hat{H} \rangle = \frac{\langle \Psi_{GB}^{AF} | \hat{H} | \Psi_{GB}^{AF} \rangle}{\langle \Psi_{GB}^{AF} | \Psi_{GB}^{AF} \rangle}. \quad (\text{D.1})$$

Let us consider the denominator of this expression. Using (4.18), it can be written:

$$\begin{aligned} \langle \Psi_{GB}^{AF} | \Psi_{GB}^{AF} \rangle &= \frac{1}{4} \text{Tr}_{\{\tau_i\}} \text{Tr}_{\{\tau_{i'}\}} \left[\langle 0 | \beta_{\vec{k}_1 \uparrow} \beta_{\vec{k}_2 \uparrow} \dots \beta_{\vec{k}_{N/2} \uparrow} E^{\dagger \uparrow}(\{\tau_{i'}\}) E^{\uparrow}(\{\tau_i\}) \beta_{\vec{k}_{N/2} \uparrow}^\dagger \dots \beta_{\vec{k}_2 \uparrow}^\dagger \beta_{\vec{k}_1 \uparrow}^\dagger | 0 \rangle \right. \\ &\quad \cdot \left. \langle 0 | \beta_{\vec{k}_1 \downarrow} \beta_{\vec{k}_2 \downarrow} \dots \beta_{\vec{k}_{N/2} \downarrow} E^{\dagger \downarrow}(\{\tau_{i'}\}) E^{\downarrow}(\{\tau_i\}) \beta_{\vec{k}_{N/2} \downarrow}^\dagger \dots \beta_{\vec{k}_2 \downarrow}^\dagger \beta_{\vec{k}_1 \downarrow}^\dagger | 0 \rangle \right] \end{aligned} \quad (\text{D.2})$$

where N is the total number of electrons. In all the calculation $N \leq L^2$ and therefore $\alpha_{\vec{k}_i} = \beta_{\vec{k}_i}$ for $i = 1 \dots N/2$. Thanks to the Hubbard-Stratonovich transformation, the exponents in $E^\sigma(\{\tau_i\})$, given by Eq. (4.19), are quadratic in the fermionic operators and it is possible to integrate out the fermionic degrees of freedom (see Appendix F). After this integration, only the trace over the Ising spins remains:

$$\begin{aligned} \langle \Psi_{GB}^{AF} | \Psi_{GB}^{AF} \rangle &= \frac{1}{4} \text{Tr}_{\{\tau_i\}} \text{Tr}_{\{\tau_{i'}\}} \left| \begin{array}{ccc} B_{\vec{k}_1 \vec{k}_1}^\uparrow & \dots & B_{\vec{k}_{N/2} \vec{k}_1}^\uparrow \\ \vdots & \ddots & \vdots \\ B_{\vec{k}_1 \vec{k}_{N/2}}^\uparrow & \dots & B_{\vec{k}_{N/2} \vec{k}_{N/2}}^\uparrow \end{array} \right| \left| \begin{array}{ccc} B_{\vec{k}_1 \vec{k}_1}^\downarrow & \dots & B_{\vec{k}_{N/2} \vec{k}_1}^\downarrow \\ \vdots & \ddots & \vdots \\ B_{\vec{k}_1 \vec{k}_{N/2}}^\downarrow & \dots & B_{\vec{k}_{N/2} \vec{k}_{N/2}}^\downarrow \end{array} \right| \\ &= \frac{1}{4} \text{Tr}_{\{\tau_i, \tau_{i'}\}} |\tilde{B}^\uparrow| |\tilde{B}^\downarrow| \end{aligned} \quad (\text{D.3})$$

with:

$$\begin{aligned} B^\sigma &\equiv B^\sigma(\{\tau_i\}, \{\tau_{i'}\}) = E^{\dagger \sigma}(\{\tau_{i'}\}) \cdot E^\sigma(\{\tau_i\}) \\ \tilde{B}^\sigma &\text{ is the first } \frac{N}{2} \times \frac{N}{2} \text{ sub-matrix of } B^\sigma \end{aligned} \quad (\text{D.4})$$

D.1 One-body operators

Now we have to compute the expectation values of observables such as the kinetic energy (4.17), where the fermionic operators appear in a quadratic form. Therefore the numerator of (D.1) is first derived for a single quadratic term

$$\begin{aligned} \langle \Psi_{GB}^{AF} | \beta_{\vec{q}_i \sigma}^\dagger \beta_{\vec{q}_j \sigma} | \Psi_{GB}^{AF} \rangle &= \frac{1}{4} Tr_{\{\tau_i\}} Tr_{\{\tau_{i'}\}} \left[| \tilde{B}^{-\sigma} | \right. \\ &\cdot \underbrace{\langle 0 | \beta_{\vec{k}_1 \sigma} \beta_{\vec{k}_2 \sigma} \dots \beta_{\vec{k}_{N/2} \sigma} E^{\dagger \sigma}(\{\tau_{i'}\}) \beta_{\vec{q}_i \sigma}^\dagger \beta_{\vec{q}_j \sigma} E^\sigma(\{\tau_i\}) \beta_{\vec{k}_{N/2} \sigma}^\dagger \dots \beta_{\vec{k}_2 \sigma}^\dagger \beta_{\vec{k}_1 \sigma}^\dagger | 0 \rangle}_{:= \langle \tau_{i'} | \beta_{\vec{q}_i \sigma}^\dagger \beta_{\vec{q}_j \sigma} | \tau_i \rangle} \left. \right]. \end{aligned}$$

The identity $\mathbb{1} = E^\sigma \cdot (E^\sigma)^{-1}$ can be introduced in $\langle \tau_{i'} | \beta_{\vec{q}_i \sigma}^\dagger \beta_{\vec{q}_j \sigma} | \tau_i \rangle$ to get:

$$\begin{aligned} \langle \tau_{i'} | \beta_{\vec{q}_i \sigma}^\dagger \beta_{\vec{q}_j \sigma} | \tau_i \rangle &= \langle 0 | \beta_{\vec{k}_1 \sigma} \beta_{\vec{k}_2 \sigma} \dots \beta_{\vec{k}_{N/2} \sigma} E^{\dagger \sigma} \cdot E^\sigma \left[(E^\sigma)^{-1} \beta_{\vec{q}_i \sigma}^\dagger \beta_{\vec{q}_j \sigma} E^\sigma \right] \\ &\cdot \beta_{\vec{k}_{N/2} \sigma}^\dagger \dots \beta_{\vec{k}_2 \sigma}^\dagger \beta_{\vec{k}_1 \sigma}^\dagger | 0 \rangle \end{aligned} \quad (\text{D.5})$$

Using the basis which diagonalise E^σ , it is straightforward to show (see Appendix G) that :

$$(E^\sigma)^{-1} \beta_{\vec{q}_i \sigma}^\dagger \beta_{\vec{q}_j \sigma} E^\sigma = \sum_{\vec{q}', \vec{q}''} (E^\sigma)_{\vec{q}' \vec{q}_i}^{-1} (E^\sigma)_{\vec{q}_j \vec{q}''} \beta_{\vec{q}' \sigma}^\dagger \beta_{\vec{q}'' \sigma} \quad (\text{D.6})$$

and then:

$$\begin{aligned} \langle \tau_{i'} | \beta_{\vec{q}_i \sigma}^\dagger \beta_{\vec{q}_j \sigma} | \tau_i \rangle &= \sum_{\vec{q}', \vec{q}''} (E^\sigma)_{\vec{q}' \vec{q}_i}^{-1} (E^\sigma)_{\vec{q}_j \vec{q}''} \\ &\cdot \langle 0 | \beta_{\vec{k}_1 \sigma} \beta_{\vec{k}_2 \sigma} \dots \beta_{\vec{k}_{N/2} \sigma} E^{\dagger \sigma} \cdot E^\sigma \underbrace{(\beta_{\vec{q}' \sigma}^\dagger \beta_{\vec{q}'' \sigma})}_{\delta_{\vec{q}' \vec{q}''} - \beta_{\vec{q}'' \sigma}^\dagger \beta_{\vec{q}' \sigma}} \beta_{\vec{k}_{N/2} \sigma}^\dagger \dots \beta_{\vec{k}_2 \sigma}^\dagger \beta_{\vec{k}_1 \sigma}^\dagger | 0 \rangle \end{aligned}$$

Again, it is possible to take the operator $E^\dagger \cdot E$ out of the expectation value, working in the $|\nu_i\rangle$ basis (see Appendix F). It gives:

$$\begin{aligned}
 \langle \tau_i | \beta_{\vec{q}_i \sigma}^\dagger \beta_{\vec{q}_j \sigma} | \tau_i \rangle &= \delta_{\vec{q}_i \vec{q}_j} \left| \begin{array}{ccc} B_{\vec{k}_1 \vec{k}_1}^\sigma & \cdots & B_{\vec{k}_1 \vec{k}_{N/2}}^\sigma \\ \vdots & \ddots & \vdots \\ B_{\vec{k}_{N/2} \vec{k}_1}^\sigma & \cdots & B_{\vec{k}_{N/2} \vec{k}_{N/2}}^\sigma \end{array} \right| \\
 &- \sum_{\vec{q}', \vec{q}''} (E^\sigma)_{\vec{q}' \vec{q}_i}^{-1} (E^\sigma)_{\vec{q}_j \vec{q}''} \sum_{\vec{k}_i'} B_{\vec{k}_1' \vec{k}_1}^\sigma \cdots B_{\vec{k}_{N/2}' \vec{k}_{N/2}}^\sigma \\
 &\cdot \langle 0 | \beta_{\vec{k}_1' \sigma} \beta_{\vec{k}_2' \sigma} \cdots \beta_{\vec{k}_{N/2}' \sigma} \beta_{\vec{q}' \sigma}^\dagger \beta_{\vec{q}'' \sigma}^\dagger \beta_{\vec{k}_{N/2} \sigma} \cdots \beta_{\vec{k}_2 \sigma}^\dagger \beta_{\vec{k}_1 \sigma}^\dagger | 0 \rangle \\
 &= \delta_{\vec{q}_i \vec{q}_j} |\tilde{B}^\sigma| - \sum_{\vec{q}'} (E^\sigma)_{\vec{q}' \vec{q}_i}^{-1} \sum_{\vec{k}_i', \vec{q}''} B_{\vec{k}_1' \vec{k}_1}^\sigma \cdots B_{\vec{k}_{N/2}' \vec{k}_{N/2}}^\sigma \cdot E_{\vec{q}_j \vec{q}''}^\sigma \\
 &\cdot \langle 0 | \beta_{\vec{k}_1' \sigma} \beta_{\vec{k}_2' \sigma} \cdots \beta_{\vec{k}_{N/2}' \sigma} \beta_{\vec{q}' \sigma}^\dagger \beta_{\vec{q}'' \sigma}^\dagger \beta_{\vec{k}_{N/2} \sigma} \cdots \beta_{\vec{k}_2 \sigma}^\dagger \beta_{\vec{k}_1 \sigma}^\dagger | 0 \rangle \\
 &= \delta_{\vec{q}_i \vec{q}_j} |\tilde{B}^\sigma| - \sum_{\vec{q}'} (E^\sigma)_{\vec{q}' \vec{q}_i}^{-1} \left| \begin{array}{ccc} B_{\vec{k}_1 \vec{k}_1}^\sigma & \cdots & B_{\vec{k}_1 \vec{k}_{N/2}}^\sigma & B_{\vec{k}_1 \vec{q}'}^\sigma \\ \vdots & \ddots & \vdots & \vdots \\ B_{\vec{k}_{N/2} \vec{k}_1}^\sigma & \cdots & B_{\vec{k}_{N/2} \vec{k}_{N/2}}^\sigma & B_{\vec{k}_{N/2} \vec{q}'}^\sigma \\ E_{\vec{q}_j \vec{k}_1}^\sigma & \cdots & E_{\vec{q}_j \vec{k}_{N/2}}^\sigma & E_{\vec{q}_j \vec{q}'}^\sigma \end{array} \right| \\
 &= \delta_{\vec{q}_i \vec{q}_j} |\tilde{B}^\sigma| - \left| \begin{array}{ccc} B_{\vec{k}_1 \vec{k}_1}^\sigma & \cdots & B_{\vec{k}_1 \vec{k}_{N/2}}^\sigma & (B^\sigma (E^\sigma)^{-1})_{\vec{k}_1 \vec{q}_i} \\ \vdots & \ddots & \vdots & \vdots \\ B_{\vec{k}_{N/2} \vec{k}_1}^\sigma & \cdots & B_{\vec{k}_{N/2} \vec{k}_{N/2}}^\sigma & (B^\sigma (E^\sigma)^{-1})_{\vec{k}_{N/2} \vec{q}_i} \\ E_{\vec{q}_j \vec{k}_1}^\sigma & \cdots & E_{\vec{q}_j \vec{k}_{N/2}}^\sigma & (E^\sigma (E^\sigma)^{-1})_{\vec{q}_j \vec{q}_i} \end{array} \right|
 \end{aligned}$$

But $B^\sigma (E^\sigma)^{-1} = E^{\dagger \sigma}$ and $E^\sigma (E^\sigma)^{-1} = \mathbb{1}$, therefore:

$$\begin{aligned}
 \langle \tau_i | \beta_{\vec{q}_i \sigma}^\dagger \beta_{\vec{q}_j \sigma} | \tau_i \rangle &= - \left| \begin{array}{ccc} B_{\vec{k}_1 \vec{k}_1}^\sigma & \cdots & B_{\vec{k}_1 \vec{k}_{N/2}}^\sigma & E_{\vec{k}_1 \vec{q}_i}^{\dagger \sigma} \\ \vdots & \ddots & \vdots & \vdots \\ B_{\vec{k}_{N/2} \vec{k}_1}^\sigma & \cdots & B_{\vec{k}_{N/2} \vec{k}_{N/2}}^\sigma & E_{\vec{k}_{N/2} \vec{q}_i}^{\dagger \sigma} \\ E_{\vec{q}_j \vec{k}_1}^\sigma & \cdots & E_{\vec{q}_j \vec{k}_{N/2}}^\sigma & 0 \end{array} \right| \\
 &= |\tilde{B}^\sigma| \cdot |\tilde{E}_{\vec{q}_j}^\sigma (\tilde{B}^\sigma)^{-1} \tilde{E}_{\vec{q}_i}^{\dagger \sigma}|, \tag{D.7}
 \end{aligned}$$

where $\tilde{E}_{\vec{q}_j}^\sigma$ means the first $N/2$ elements of row j of E^σ and $\tilde{E}_{\vec{q}_i}^{\dagger\sigma}$ means the first $N/2$ elements of column i of $E^{\dagger\sigma}$. Eventually we obtain:

$$\langle \Psi_{GB}^{AF} | \beta_{\vec{q}_i\sigma}^\dagger \beta_{\vec{q}_j\sigma} | \Psi_{GB}^{AF} \rangle = \frac{1}{4} \text{Tr}_{\{\tau_i, \tau_{i'}\}} \left[|\tilde{B}^{-\sigma}| |\tilde{B}^\sigma| \cdot |\tilde{E}_{\vec{q}_j}^\sigma (\tilde{B}^\sigma)^{-1} \tilde{E}_{\vec{q}_i}^{\dagger\sigma}| \right] \quad (\text{D.8})$$

Finally we can compute the single-particle Green's functions, defined as:

$$\begin{aligned} G_{\vec{q}_i, \vec{q}_j}^\sigma &:= \langle \beta_{\vec{q}_i\sigma}^\dagger \beta_{\vec{q}_j\sigma} \rangle = \frac{\langle \Psi_{GB}^{AF} | \beta_{\vec{q}_i\sigma}^\dagger \beta_{\vec{q}_j\sigma} | \Psi_{GB}^{AF} \rangle}{\langle \Psi_{GB}^{AF} | \Psi_{GB}^{AF} \rangle} \\ &= \frac{\text{Tr}_{\{\tau_i, \tau_{i'}\}} \left[|\tilde{B}^{-\sigma}| |\tilde{B}^\sigma| \cdot |\tilde{E}_{\vec{q}_j}^\sigma (\tilde{B}^\sigma)^{-1} \tilde{E}_{\vec{q}_i}^{\dagger\sigma}| \right]}{\text{Tr}_{\{\tau_i, \tau_{i'}\}} \left[|\tilde{B}^{-\sigma}| |\tilde{B}^\sigma| \right]}. \end{aligned} \quad (\text{D.9})$$

These Green's functions allows us to compute the one-body operators expectation values.

D.2 Two-body operators

In principle, the expectation value of a general two-body operator can be computed using the formula that will be obtained for the superconducting refined wave function (see section 4.4.1 and Appendix E) and which is very similar to Wick's theorem. However for the antiferromagnetic instability, the conservation of the particle spin by the Bogoliubov transformation (4.7) implies that two \uparrow -spins and two \downarrow -spins occur in all two-body operators of interest. In particular, when given in term of the quasiparticles β , the double occupancy operator \hat{D} is a sum over a large number of term $\beta_{\vec{q}_p\uparrow}^\dagger \beta_{\vec{q}_q\uparrow} \beta_{\vec{q}_r\downarrow}^\dagger \beta_{\vec{q}_s\downarrow}$. Therefore the expectation values are easily derived from the relation

$$\langle \beta_{\vec{q}_p\uparrow}^\dagger \beta_{\vec{q}_q\uparrow} \beta_{\vec{q}_r\downarrow}^\dagger \beta_{\vec{q}_s\downarrow} \rangle = \frac{1}{4} \text{Tr}_{\{\tau_i, \tau_{i'}\}} \left[\langle \tau_{i'}^\uparrow | \beta_{\vec{q}_p\uparrow}^\dagger \beta_{\vec{q}_q\uparrow} | \tau_i^\uparrow \rangle \cdot \langle \tau_{i'}^\downarrow | \beta_{\vec{q}_r\downarrow}^\dagger \beta_{\vec{q}_s\downarrow} | \tau_i^\downarrow \rangle \right]. \quad (\text{D.10})$$

Appendix E

Grand canonical ensemble

In this appendix the main steps of the calculation leading to the expectation values of the one-body or two-body operators are given. Starting from Eq. (4.29) and using the particle-hole transformation (A.2), the operator $(n_{i\uparrow} - n_{i\downarrow})$ is written:

$$\begin{aligned}
(n_{i\uparrow} - n_{i\downarrow}) &= \frac{1}{L^2} \sum_{\vec{k}, \vec{k}'} e^{i(\vec{k}-\vec{k}') \cdot \vec{r}_i} \left[u_{\vec{k}} u_{\vec{k}'} (\delta_{\vec{k}\vec{k}'} - \beta_{-\vec{k}'}^\dagger \beta_{-\vec{k}} - \gamma_{\vec{k}}^\dagger \gamma_{\vec{k}'}) \right. \\
&\quad + v_{\vec{k}} u_{\vec{k}'} (-\beta_{-\vec{k}'}^\dagger \gamma_{-\vec{k}} + \beta_{\vec{k}}^\dagger \gamma_{\vec{k}'}) + u_{\vec{k}} v_{\vec{k}'} (-\gamma_{-\vec{k}'}^\dagger \beta_{-\vec{k}} + \gamma_{\vec{k}}^\dagger \beta_{\vec{k}'}) \\
&\quad \left. + v_{\vec{k}} v_{\vec{k}'} (\delta_{\vec{k}\vec{k}'} - \gamma_{-\vec{k}'}^\dagger \gamma_{-\vec{k}} - \beta_{\vec{k}}^\dagger \beta_{\vec{k}'}) \right]. \tag{E.1}
\end{aligned}$$

With the notation of Section 4.4.1, we obtain:

$$\begin{aligned}
\sum_i 2a\tau_i(n_{i\uparrow} - n_{i\downarrow}) &= \sum_i 2a\tau_i \left[\underbrace{\frac{1}{L^2} \sum_{\vec{k}} (u_{\vec{k}}^2 + v_{\vec{k}}^2)}_1 \right] \\
&\quad + \sum_{\vec{k}, \vec{k}'} \alpha_{\vec{k}}^\dagger W_{\vec{k}\vec{k}'}(\{\tau_i\}) \alpha_{\vec{k}'} \tag{E.2}
\end{aligned}$$

where τ_i is the Ising spin at site i introduced by the Hubbard-Stratonovich transformation (4.12). Therefore $W_{\vec{k}\vec{k}'}$ is a $2L^2 \times 2L^2$ matrix. In the same manner, the number operator becomes

$$\begin{aligned}
\hat{N} = \sum_i (n_{i\uparrow} + n_{i\downarrow}) &= L^2 + \sum_{\vec{k}} \left[(u_{\vec{k}}^2 - v_{\vec{k}}^2) (\gamma_{\vec{k}}^\dagger \gamma_{\vec{k}} - \beta_{\vec{k}}^\dagger \beta_{\vec{k}}) \right. \\
&\quad \left. - 2u_{\vec{k}} v_{\vec{k}} (\gamma_{\vec{k}}^\dagger \beta_{\vec{k}} + \beta_{\vec{k}}^\dagger \gamma_{\vec{k}}) \right] \\
&= L^2 + \sum_{\vec{k}, \vec{k}'} \alpha_{\vec{k}}^\dagger N_{\vec{k}\vec{k}'} \alpha_{\vec{k}'} \tag{E.3}
\end{aligned}$$

where $N_{\vec{k}\vec{k}'}$ is a $2L^2 \times 2L^2$ matrix. As we can see in (E.1) and (E.3), the electronic operators now conserve the number of particles γ and β . Eventually, we get for the Gutzwiller operator

$$e^{-g\hat{D}} = \frac{1}{2} \text{Tr}_{\{\tau_i\}} \left[e^{[(\sum_i 2a\tau_i) - \frac{1}{2}gL^2]} \cdot e^{\sum_{\vec{k},\vec{k}'} \alpha_{\vec{k}}^\dagger W_{\vec{k}\vec{k}'}(\{\tau_i\}) \alpha_{\vec{k}'}} \cdot e^{\sum_{\vec{k},\vec{k}'} \alpha_{\vec{k}}^\dagger N_{\vec{k}\vec{k}'} \alpha_{\vec{k}'}} \right]. \quad (\text{E.4})$$

For the kinetic projector, we have to transform the kinetic operator in term of particles γ and β . It is easily done using the Bogoliubov transformation (B.5). It leads to

$$\begin{aligned} \hat{T} &= \sum_{\vec{k},\sigma} \epsilon_{\vec{k}} c_{\vec{k},\sigma}^\dagger c_{\vec{k},\sigma} \\ &= \sum_{\vec{k}} \epsilon_{\vec{k}} \left[(u_{\vec{k}}^2 - v_{\vec{k}}^2) (\gamma_{\vec{k}}^\dagger \gamma_{\vec{k}} - \beta_{\vec{k}}^\dagger \beta_{\vec{k}}) \right. \\ &\quad \left. - 2u_{\vec{k}}v_{\vec{k}} (\gamma_{\vec{k}}^\dagger \beta_{\vec{k}} + \beta_{\vec{k}}^\dagger \gamma_{\vec{k}}) \right] \\ &= \sum_{\vec{k},\vec{k}'} \alpha_{\vec{k}}^\dagger T_{\vec{k}\vec{k}'} \alpha_{\vec{k}'} \quad (\text{E.5}) \end{aligned}$$

Therefore:

$$\begin{aligned} e^{-h\hat{T}} e^{-g\hat{D}} |BCS\rangle &= \frac{1}{2} \text{Tr}_{\{\tau_i\}} \left\{ e^{[(\sum_i 2a\tau_i) - \frac{1}{2}gL^2]} \right. \\ &\quad \cdot \left[e^{\sum_{\vec{k},\vec{k}'} \alpha_{\vec{k}}^\dagger T_{\vec{k}\vec{k}'} \alpha_{\vec{k}'}} \cdot e^{\sum_{\vec{k},\vec{k}'} \alpha_{\vec{k}}^\dagger W_{\vec{k}\vec{k}'}(\{\tau_i\}) \alpha_{\vec{k}'}} \cdot e^{\sum_{\vec{k},\vec{k}'} \alpha_{\vec{k}}^\dagger N_{\vec{k}\vec{k}'} \alpha_{\vec{k}'}} \prod_{\vec{k}} \beta_{\vec{k}}^\dagger |\tilde{0}\rangle \right] \Big\} \\ &= \frac{1}{2} \text{Tr}_{\{\tau_i\}} \left\{ e^{[(\sum_i 2a\tau_i) - \frac{1}{2}gL^2]} \cdot \left[E(\{\tau_i\}) \prod_{\vec{k}} \beta_{\vec{k}}^\dagger |\tilde{0}\rangle \right] \right\} \quad (\text{E.6}) \end{aligned}$$

with:

$$E(\{\tau_i\}) = e^{\sum_{\vec{k},\vec{k}'} \alpha_{\vec{k}}^\dagger T_{\vec{k}\vec{k}'} \alpha_{\vec{k}'}} \cdot e^{\sum_{\vec{k},\vec{k}'} \alpha_{\vec{k}}^\dagger W_{\vec{k}\vec{k}'}(\{\tau_i\}) \alpha_{\vec{k}'}} \cdot e^{\sum_{\vec{k},\vec{k}'} \alpha_{\vec{k}}^\dagger N_{\vec{k}\vec{k}'} \alpha_{\vec{k}'}} \quad (\text{E.7})$$

The double occupancy operator \hat{D} can also be described by γ and β quasiparticles:

$$\begin{aligned} \hat{D} &= \sum_i n_{i\uparrow} n_{i\downarrow} = \frac{1}{L^4} \sum_i \left(\sum_{\vec{k},\vec{k}'} e^{i(\vec{k}-\vec{k}') \cdot \vec{n}_i} c_{\vec{k}\uparrow}^\dagger c_{\vec{k}'\uparrow} \right) \left(\sum_{\vec{q},\vec{q}'} e^{i(\vec{q}-\vec{q}') \cdot \vec{n}_i} c_{\vec{q}\downarrow}^\dagger c_{\vec{q}'\downarrow} \right) \\ &= \frac{1}{L^2} \sum_{\vec{k},\vec{k}',\vec{q},\vec{q}'} \underbrace{\frac{1}{L^2} \sum_i e^{i(\vec{k}-\vec{k}'+\vec{q}-\vec{q}') \cdot \vec{n}_i} c_{\vec{k}\uparrow}^\dagger c_{\vec{k}'\uparrow} c_{\vec{q}\downarrow}^\dagger c_{\vec{q}'\downarrow}}_{\Delta[\vec{k}-\vec{k}'+\vec{q}-\vec{q}']} \\ &= \frac{1}{L^2} \sum_{\vec{k},\vec{k}',\vec{q},\vec{q}'} \Delta[\vec{k}-\vec{k}'+\vec{q}-\vec{q}'] \left[(u_{\vec{k}} \beta_{-\vec{k}} + v_{\vec{k}} \gamma_{-\vec{k}}) (u_{\vec{k}'} \beta_{-\vec{k}'}^\dagger + v_{\vec{k}'} \gamma_{-\vec{k}'}^\dagger) \right. \\ &\quad \left. \cdot (u_{\vec{q}} \gamma_{\vec{q}}^\dagger - v_{\vec{q}} \beta_{\vec{q}}^\dagger) (u_{\vec{q}'} \gamma_{\vec{q}'} - v_{\vec{q}'} \beta_{\vec{q}'} \right] \quad (\text{E.8}) \end{aligned}$$

As the sum contains all vectors of the First Brillouin Zone and $u_{\vec{q}}$, $v_{\vec{q}}$ are even functions, it can be written:

$$\begin{aligned}
\hat{D} &= \frac{1}{L^2} \sum_{\vec{k}, \vec{k}', \vec{q}, \vec{q}'} \Delta[\vec{k}' - \vec{k} + \vec{q} - \vec{q}'] \left[(u_{\vec{k}} \beta_{\vec{k}} + v_{\vec{k}} \gamma_{\vec{k}}) (u_{\vec{k}'} \beta_{\vec{k}'}^\dagger + v_{\vec{k}'} \gamma_{\vec{k}'}^\dagger) \right. \\
&\quad \left. \cdot (u_{\vec{q}} \gamma_{\vec{q}}^\dagger - v_{\vec{q}} \beta_{\vec{q}}^\dagger) (u_{\vec{q}'} \gamma_{\vec{q}'} - v_{\vec{q}'} \beta_{\vec{q}'}^\dagger) \right] \\
&= \sum_{\vec{q}} \left[u_{\vec{q}}^2 \gamma_{\vec{q}}^\dagger \gamma_{\vec{q}} - u_{\vec{q}} v_{\vec{q}} (\beta_{\vec{q}}^\dagger \gamma_{\vec{q}} + \gamma_{\vec{q}}^\dagger \beta_{\vec{q}}) + v_{\vec{q}}^2 \beta_{\vec{q}}^\dagger \beta_{\vec{q}} \right] \\
&+ \frac{1}{L^2} \sum_{\vec{k}, \vec{k}', \vec{q}, \vec{q}'} \Delta[\vec{k}' - \vec{k} + \vec{q} - \vec{q}'] \left[-u_{\vec{k}} u_{\vec{k}'} u_{\vec{q}} u_{\vec{q}'} \beta_{\vec{k}'}^\dagger \beta_{\vec{k}}^\dagger \gamma_{\vec{q}}^\dagger \gamma_{\vec{q}'} \right. \\
&+ u_{\vec{k}} u_{\vec{k}'} u_{\vec{q}} v_{\vec{q}'} \beta_{\vec{k}'}^\dagger \beta_{\vec{k}}^\dagger \gamma_{\vec{q}}^\dagger \beta_{\vec{q}'} + u_{\vec{k}} u_{\vec{k}'} v_{\vec{q}} u_{\vec{q}'} \beta_{\vec{k}'}^\dagger \beta_{\vec{k}}^\dagger \beta_{\vec{q}}^\dagger \gamma_{\vec{q}'} - u_{\vec{k}} u_{\vec{k}'} v_{\vec{q}} v_{\vec{q}'} \beta_{\vec{k}'}^\dagger \beta_{\vec{k}}^\dagger \beta_{\vec{q}}^\dagger \beta_{\vec{q}'} \\
&- u_{\vec{k}} v_{\vec{k}'} u_{\vec{q}} u_{\vec{q}'} \gamma_{\vec{k}'}^\dagger \beta_{\vec{k}}^\dagger \gamma_{\vec{q}}^\dagger \gamma_{\vec{q}'} + u_{\vec{k}} v_{\vec{k}'} u_{\vec{q}} v_{\vec{q}'} \gamma_{\vec{k}'}^\dagger \beta_{\vec{k}}^\dagger \gamma_{\vec{q}}^\dagger \beta_{\vec{q}'} + u_{\vec{k}} v_{\vec{k}'} v_{\vec{q}} u_{\vec{q}'} \gamma_{\vec{k}'}^\dagger \beta_{\vec{k}}^\dagger \beta_{\vec{q}}^\dagger \gamma_{\vec{q}'} \\
&- u_{\vec{k}} v_{\vec{k}'} v_{\vec{q}} v_{\vec{q}'} \gamma_{\vec{k}'}^\dagger \beta_{\vec{k}}^\dagger \beta_{\vec{q}}^\dagger \beta_{\vec{q}'} - v_{\vec{k}} u_{\vec{k}'} u_{\vec{q}} u_{\vec{q}'} \beta_{\vec{k}}^\dagger \gamma_{\vec{k}}^\dagger \gamma_{\vec{q}}^\dagger \gamma_{\vec{q}'} + v_{\vec{k}} u_{\vec{k}'} u_{\vec{q}} v_{\vec{q}'} \beta_{\vec{k}}^\dagger \gamma_{\vec{k}}^\dagger \gamma_{\vec{q}}^\dagger \beta_{\vec{q}'} \\
&+ v_{\vec{k}} u_{\vec{k}'} v_{\vec{q}} u_{\vec{q}'} \beta_{\vec{k}}^\dagger \gamma_{\vec{k}}^\dagger \beta_{\vec{q}}^\dagger \gamma_{\vec{q}'} - v_{\vec{k}} u_{\vec{k}'} v_{\vec{q}} v_{\vec{q}'} \beta_{\vec{k}}^\dagger \gamma_{\vec{k}}^\dagger \beta_{\vec{q}}^\dagger \beta_{\vec{q}'} - v_{\vec{k}} v_{\vec{k}'} u_{\vec{q}} u_{\vec{q}'} \gamma_{\vec{k}}^\dagger \gamma_{\vec{k}}^\dagger \gamma_{\vec{q}}^\dagger \gamma_{\vec{q}'} \\
&\left. + v_{\vec{k}} v_{\vec{k}'} u_{\vec{q}} v_{\vec{q}'} \gamma_{\vec{k}}^\dagger \gamma_{\vec{k}}^\dagger \beta_{\vec{q}}^\dagger \beta_{\vec{q}'} + v_{\vec{k}} v_{\vec{k}'} v_{\vec{q}} u_{\vec{q}'} \gamma_{\vec{k}}^\dagger \gamma_{\vec{k}}^\dagger \beta_{\vec{q}}^\dagger \gamma_{\vec{q}'} - v_{\vec{k}} v_{\vec{k}'} v_{\vec{q}} v_{\vec{q}'} \gamma_{\vec{k}}^\dagger \gamma_{\vec{k}}^\dagger \beta_{\vec{q}}^\dagger \beta_{\vec{q}'} \right].
\end{aligned} \tag{E.8}$$

To simplify the calculation, we have ordered fermionic operators which now are all of type “ $\alpha^\dagger \alpha \alpha^\dagger \alpha$ ”. In so doing, the first sum of (E.8) is generated.

E.1 One-body operators

Eq. (4.35) for the expectation values of the one-body operators is now straightforwardly obtained using the form (E.6) of the refined wave function and the results of Appendix F and G. The calculation is similar to what has been done for the antiferromagnetic wave function in Section 4.3.1. The main difference is that only one matrix $B = E^\dagger \cdot E$ is involved due to the fact that the electronic operators mix the quasiparticles γ and β .

E.2 Two-body operators

For the same reason, the two-body operators expectation values do not factorize. However we are going to show that the expectation value of operators where four fermionic operators are involved, like in Eq. (E.8), can be computed by a formulae similar to “Wick’s theorem”. To prove this, we compute this expectation value in an

analogous way to that for the one-body operators in Section 4.3.1. First the identity is introduced as in (D.5) to gather E^\dagger and E operators (it gives B). It is straightforward to get a relation such as (D.6), following the calculation of appendix G. Then the operator B is moved out of the expectation value working in the eigenvectors basis, as in appendix F. We obtain:

$$\begin{aligned}
\langle \tau_{i'} | \alpha_{\vec{q}_s}^\dagger \alpha_{\vec{q}_p} \alpha_{\vec{q}_q}^\dagger \alpha_{\vec{q}_r} | \tau_i \rangle &= \langle \hat{0} | \alpha_{\vec{k}_1} \alpha_{\vec{k}_2} \dots \alpha_{\vec{k}_N} (E^\dagger) \alpha_{\vec{q}_s}^\dagger \alpha_{\vec{q}_p} \alpha_{\vec{q}_q}^\dagger \alpha_{\vec{q}_r} (E) \alpha_{\vec{k}_N}^\dagger \dots \alpha_{\vec{k}_2}^\dagger \alpha_{\vec{k}_1}^\dagger | \hat{0} \rangle \\
&= \delta_{\vec{q}_s \vec{q}_p} \delta_{\vec{q}_q \vec{q}_r} |\tilde{B}| - \delta_{\vec{q}_s \vec{q}_p} \begin{vmatrix} B_{\vec{k}_1 \vec{k}_1} & \dots & B_{\vec{k}_1 \vec{k}_N} & E_{\vec{k}_1 \vec{q}_q}^\dagger \\ \vdots & \ddots & \vdots & \vdots \\ B_{\vec{k}_N \vec{k}_1} & \dots & B_{\vec{k}_N \vec{k}_N} & E_{\vec{k}_N \vec{q}_q}^\dagger \\ E_{\vec{q}_r \vec{k}_1} & \dots & E_{\vec{q}_r \vec{k}_N} & \delta_{\vec{q}_q \vec{q}_r} \end{vmatrix} \\
&- \delta_{\vec{q}_q \vec{q}_r} \begin{vmatrix} B_{\vec{k}_1 \vec{k}_1} & \dots & B_{\vec{k}_1 \vec{k}_N} & E_{\vec{k}_1 \vec{q}_s}^\dagger \\ \vdots & \ddots & \vdots & \vdots \\ B_{\vec{k}_N \vec{k}_1} & \dots & B_{\vec{k}_N \vec{k}_N} & E_{\vec{k}_N \vec{q}_s}^\dagger \\ E_{\vec{q}_p \vec{k}_1} & \dots & E_{\vec{q}_p \vec{k}_N} & \delta_{\vec{q}_s \vec{q}_p} \end{vmatrix} + \delta_{\vec{q}_r \vec{q}_s} \begin{vmatrix} B_{\vec{k}_1 \vec{k}_1} & \dots & B_{\vec{k}_1 \vec{k}_N} & E_{\vec{k}_1 \vec{q}_q}^\dagger \\ \vdots & \ddots & \vdots & \vdots \\ B_{\vec{k}_N \vec{k}_1} & \dots & B_{\vec{k}_N \vec{k}_N} & E_{\vec{k}_N \vec{q}_q}^\dagger \\ E_{\vec{q}_p \vec{k}_1} & \dots & E_{\vec{q}_p \vec{k}_N} & \delta_{\vec{q}_p \vec{q}_q} \end{vmatrix} \\
&- \begin{vmatrix} B_{\vec{k}_1 \vec{k}_1} & \dots & B_{\vec{k}_1 \vec{k}_N} & E_{\vec{k}_1 \vec{q}_q}^\dagger & E_{\vec{k}_1 \vec{q}_s}^\dagger \\ \vdots & \ddots & \vdots & \vdots & \vdots \\ B_{\vec{k}_N \vec{k}_1} & \dots & B_{\vec{k}_N \vec{k}_N} & E_{\vec{k}_N \vec{q}_q}^\dagger & E_{\vec{k}_N \vec{q}_s}^\dagger \\ E_{\vec{q}_p \vec{k}_1} & \dots & E_{\vec{q}_p \vec{k}_N} & \delta_{\vec{q}_p \vec{q}_q} & \delta_{\vec{q}_p \vec{q}_s} \\ E_{\vec{q}_r \vec{k}_1} & \dots & E_{\vec{q}_r \vec{k}_N} & \delta_{\vec{q}_r \vec{q}_q} & \delta_{\vec{q}_r \vec{q}_s} \end{vmatrix}. \tag{E.9}
\end{aligned}$$

It is now easy to write this expectation value as a function of one-body expectation values, leading to

$$\begin{aligned}
\langle \tau_{i'} | \alpha_{\vec{q}_s}^\dagger \alpha_{\vec{q}_p} \alpha_{\vec{q}_q}^\dagger \alpha_{\vec{q}_r} | \tau_i \rangle &= \delta_{\vec{q}_s \vec{q}_p} \delta_{\vec{q}_q \vec{q}_r} |\tilde{B}| - \delta_{\vec{q}_s \vec{q}_p} \delta_{\vec{q}_q \vec{q}_r} |\tilde{B}| \\
&+ \delta_{\vec{q}_s \vec{q}_p} \langle \tau_{i'} | \alpha_{\vec{q}_q}^\dagger \alpha_{\vec{q}_r} | \tau_i \rangle - \delta_{\vec{q}_q \vec{q}_r} \delta_{\vec{q}_s \vec{q}_p} |\tilde{B}| + \delta_{\vec{q}_q \vec{q}_r} \langle \tau_{i'} | \alpha_{\vec{q}_s}^\dagger \alpha_{\vec{q}_p} | \tau_i \rangle \\
&+ \delta_{\vec{q}_r \vec{q}_s} \delta_{\vec{q}_p \vec{q}_q} |\tilde{B}| - \delta_{\vec{q}_r \vec{q}_s} \langle \tau_{i'} | \alpha_{\vec{q}_q}^\dagger \alpha_{\vec{q}_p} | \tau_i \rangle \\
&- \begin{vmatrix} \delta_{\vec{q}_p \vec{q}_q} - \tilde{E}_{\vec{q}_p}(\tilde{B})^{-1} E_{\vec{q}_q}^\dagger & \delta_{\vec{q}_p \vec{q}_s} - \tilde{E}_{\vec{q}_p}(\tilde{B})^{-1} E_{\vec{q}_s}^\dagger \\ \delta_{\vec{q}_r \vec{q}_q} - \tilde{E}_{\vec{q}_r}(\tilde{B})^{-1} E_{\vec{q}_q}^\dagger & \delta_{\vec{q}_r \vec{q}_s} - \tilde{E}_{\vec{q}_r}(\tilde{B})^{-1} E_{\vec{q}_s}^\dagger \end{vmatrix} \cdot |\tilde{B}|. \tag{E.10}
\end{aligned}$$

Since

$$\tilde{E}_{\vec{q}_r}(\tilde{B})^{-1} E_{\vec{q}_q}^\dagger = \frac{\langle \tau_{i'} | \alpha_{\vec{q}_q}^\dagger \alpha_{\vec{q}_r} | \tau_i \rangle}{|\tilde{B}|}, \tag{E.11}$$

we have

$$\begin{aligned}
\langle \tau_{i'} | \alpha_{\vec{q}_s}^\dagger \alpha_{\vec{q}_p} \alpha_{\vec{q}_q}^\dagger \alpha_{\vec{q}_r} | \tau_i \rangle &= \delta_{\vec{q}_s \vec{q}_p} \langle \tau_{i'} | \alpha_{\vec{q}_q}^\dagger \alpha_{\vec{q}_r} | \tau_i \rangle - \delta_{\vec{q}_q \vec{q}_r} \delta_{\vec{q}_s \vec{q}_p} |\tilde{B}| \\
&+ \delta_{\vec{q}_q \vec{q}_r} \langle \tau_{i'} | \alpha_{\vec{q}_s}^\dagger \alpha_{\vec{q}_p} | \tau_i \rangle + \delta_{\vec{q}_r \vec{q}_s} \delta_{\vec{q}_p \vec{q}_q} |\tilde{B}| - \delta_{\vec{q}_r \vec{q}_s} \langle \tau_{i'} | \alpha_{\vec{q}_q}^\dagger \alpha_{\vec{q}_p} | \tau_i \rangle \\
&- \delta_{\vec{q}_p \vec{q}_q} \delta_{\vec{q}_r \vec{q}_s} |\tilde{B}| + \delta_{\vec{q}_p \vec{q}_q} \langle \tau_{i'} | \alpha_{\vec{q}_s}^\dagger \alpha_{\vec{q}_r} | \tau_i \rangle + \delta_{\vec{q}_r \vec{q}_s} \langle \tau_{i'} | \alpha_{\vec{q}_q}^\dagger \alpha_{\vec{q}_p} | \tau_i \rangle \\
&- \frac{1}{|\tilde{B}|} \langle \tau_{i'} | \alpha_{\vec{q}_q}^\dagger \alpha_{\vec{q}_p} | \tau_i \rangle \langle \tau_{i'} | \alpha_{\vec{q}_s}^\dagger \alpha_{\vec{q}_r} | \tau_i \rangle + \delta_{\vec{q}_r \vec{q}_q} \delta_{\vec{q}_p \vec{q}_s} |\tilde{B}| \\
&- \delta_{\vec{q}_r \vec{q}_q} \langle \tau_{i'} | \alpha_{\vec{q}_s}^\dagger \alpha_{\vec{q}_p} | \tau_i \rangle - \delta_{\vec{q}_p \vec{q}_s} \langle \tau_{i'} | \alpha_{\vec{q}_q}^\dagger \alpha_{\vec{q}_r} | \tau_i \rangle \\
&+ \frac{1}{|\tilde{B}|} \langle \tau_{i'} | \alpha_{\vec{q}_q}^\dagger \alpha_{\vec{q}_r} | \tau_i \rangle \langle \tau_{i'} | \alpha_{\vec{q}_s}^\dagger \alpha_{\vec{q}_p} | \tau_i \rangle .
\end{aligned} \tag{E.12}$$

We finally obtain

$$\begin{aligned}
\frac{\langle \tau_{i'} | \alpha_{\vec{q}_s}^\dagger \alpha_{\vec{q}_p} \alpha_{\vec{q}_q}^\dagger \alpha_{\vec{q}_r} | \tau_i \rangle}{|\tilde{B}|} &= \frac{\delta_{\vec{q}_p \vec{q}_q} \langle \tau_{i'} | \alpha_{\vec{q}_s}^\dagger \alpha_{\vec{q}_r} | \tau_i \rangle}{|\tilde{B}|} \\
&+ \frac{\langle \tau_{i'} | \alpha_{\vec{q}_q}^\dagger \alpha_{\vec{q}_r} | \tau_i \rangle}{|\tilde{B}|} \frac{\langle \tau_{i'} | \alpha_{\vec{q}_s}^\dagger \alpha_{\vec{q}_p} | \tau_i \rangle}{|\tilde{B}|} - \frac{\langle \tau_{i'} | \alpha_{\vec{q}_q}^\dagger \alpha_{\vec{q}_p} | \tau_i \rangle}{|\tilde{B}|} \frac{\langle \tau_{i'} | \alpha_{\vec{q}_s}^\dagger \alpha_{\vec{q}_r} | \tau_i \rangle}{|\tilde{B}|} .
\end{aligned} \tag{E.13}$$

This relation can be compared to Wick's theorem. It allows us to compute easily the expectation value of double occupancy operator.

Appendix F

Integration of the fermionic degrees of freedom

This appendix shows how to integrate out the fermionic degrees of freedom, as in (D.2), using a suitable basis. In particular, the relation (D.3) is proven. The important point is that the operator $B^\sigma(\{\tau_i\}, \{\tau_{i'}\}) = E^{\dagger\sigma}(\{\tau_{i'}\}) E^\sigma(\{\tau_i\})$ is a product of exponentials with single-particle operators in the exponents. The Baker-Campbell-Hausdorff formula allows us to write this product as a single exponential

$$B^\sigma(\{\tau_i\}, \{\tau_{i'}\}) = e^{-\sum_{\vec{k}, \vec{k}'} \beta_{\vec{k}\sigma}^\dagger b_{\vec{k}, \vec{k}'}^\sigma \beta_{\vec{k}'\sigma}} . \quad (\text{F.1})$$

The operator in the exponent, which we do not need to calculate explicitly, is diagonalized by a transformation

$$\begin{cases} \beta_{\vec{\nu}\sigma} = \sum_{\vec{k}} \langle \vec{\nu} | \vec{k} \rangle \beta_{\vec{k}\sigma} \\ \beta_{\vec{\nu}\sigma}^\dagger = \sum_{\vec{k}} \langle \vec{k} | \vec{\nu} \rangle \beta_{\vec{k}\sigma}^\dagger \end{cases} \implies \begin{cases} \beta_{\vec{k}\sigma} = \sum_{\vec{\nu}} \langle \vec{k} | \vec{\nu} \rangle \beta_{\vec{\nu}\sigma} \\ \beta_{\vec{k}\sigma}^\dagger = \sum_{\vec{\nu}} \langle \vec{\nu} | \vec{k} \rangle \beta_{\vec{\nu}\sigma}^\dagger \end{cases} \quad (\text{F.2})$$

Therefore we may write

$$E^{\dagger\sigma}(\{\tau_{i'}\}) E^\sigma(\{\tau_i\}) = e^{-\sum_{\vec{\nu}} b_{\vec{\nu}}^\sigma \beta_{\vec{\nu}\sigma}^\dagger \beta_{\vec{\nu}\sigma}} , \quad (\text{F.3})$$

where the numbers $b_{\vec{\nu}}^\sigma$ are the eigenvalues of the $L^2 \times L^2$ matrix b^σ . The norm (D.2) is then transformed as

$$\begin{aligned} & \langle 0 | \beta_{\vec{k}_1\sigma} \beta_{\vec{k}_2\sigma} \dots \beta_{\vec{k}_{N/2}\sigma} E^{\dagger\sigma}(\{\tau_{i'}\}) E^\sigma(\{\tau_i\}) \beta_{\vec{k}_{N/2}\sigma}^\dagger \dots \beta_{\vec{k}_2\sigma}^\dagger \beta_{\vec{k}_1\sigma}^\dagger | 0 \rangle \\ &= \sum_{\{\vec{\nu}_i\}, \{\vec{\nu}'_i\}} \langle \vec{\nu}_1 | \vec{k}_1 \rangle \dots \langle \vec{\nu}_{N/2} | \vec{k}_{N/2} \rangle \cdot \langle \vec{k}_1 | \vec{\nu}'_1 \rangle \dots \langle \vec{k}_{N/2} | \vec{\nu}'_{N/2} \rangle \\ & \cdot \langle 0 | \beta_{\vec{\nu}'_1\sigma} \beta_{\vec{\nu}'_2\sigma} \dots \beta_{\vec{\nu}'_{N/2}\sigma} \prod_{\vec{\nu}} e^{-\beta_{\vec{\nu}\sigma}^\dagger b_{\vec{\nu}}^\sigma \beta_{\vec{\nu}\sigma}} \beta_{\vec{\nu}_{N/2}\sigma}^\dagger \dots \beta_{\vec{\nu}_2\sigma}^\dagger \beta_{\vec{\nu}_1\sigma}^\dagger | 0 \rangle \end{aligned}$$

$$\begin{aligned}
 &= \sum_{\vec{\nu}_i, \vec{\nu}'_i} \langle \vec{\nu}_1 | \vec{k}_1 \rangle \dots \langle \vec{\nu}_{N/2} | \vec{k}_{N/2} \rangle \cdot \langle \vec{k}_1 | \vec{\nu}'_1 \rangle \dots \langle \vec{k}_{N/2} | \vec{\nu}'_{N/2} \rangle \\
 &\cdot \langle 0 | \beta_{\vec{\nu}'_1 \sigma} \beta_{\vec{\nu}'_2 \sigma} \dots \beta_{\vec{\nu}'_{N/2} \sigma} e^{-b_{\vec{\nu}_1}} \dots e^{-b_{\vec{\nu}_{N/2}}} \beta_{\vec{\nu}_{N/2} \sigma}^\dagger \dots \beta_{\vec{\nu}_2 \sigma}^\dagger \beta_{\vec{\nu}_1 \sigma}^\dagger | 0 \rangle .
 \end{aligned} \tag{F.4}$$

For the last equality we have used the relation:

$$e^{-\beta_{\vec{\nu}_j \sigma}^\dagger b_{\vec{\nu}_j} \beta_{\vec{\nu}_j \sigma}} \beta_{\vec{\nu}_j \sigma}^\dagger = e^{-b_{\vec{\nu}_j}} \beta_{\vec{\nu}_j \sigma}^\dagger. \tag{F.5}$$

Now we can come back to the first basis:

$$\begin{aligned}
 (F.4) &= \sum_{\vec{\nu}_i, \vec{\nu}'_i} \sum_{\vec{k}'_i, \vec{k}''_i} \langle \vec{k}_1 | \vec{\nu}'_1 \rangle \langle \vec{\nu}'_1 | \vec{k}_1'' \rangle \dots \langle \vec{k}_{N/2} | \vec{\nu}'_{N/2} \rangle \langle \vec{\nu}'_{N/2} | \vec{k}_{N/2}'' \rangle \\
 &\cdot \langle \vec{k}_1' | \vec{\nu}_1 \rangle e^{-b_{\vec{\nu}_1}} \langle \vec{\nu}_1 | \vec{k}_1 \rangle \dots \langle \vec{k}'_{N/2} | \vec{\nu}_{N/2} \rangle e^{-b_{\vec{\nu}_{N/2}}} \langle \vec{\nu}_{N/2} | \vec{k}_{N/2} \rangle \\
 &\cdot \langle 0 | \beta_{\vec{k}_1' \sigma} \beta_{\vec{k}_2'' \sigma} \dots \beta_{\vec{k}_{N/2}'' \sigma} \beta_{\vec{k}'_{N/2} \sigma}^\dagger \dots \beta_{\vec{k}_2' \sigma}^\dagger \beta_{\vec{k}_1' \sigma}^\dagger | 0 \rangle .
 \end{aligned} \tag{F.6}$$

As

$$\sum_{\vec{\nu}_j} \langle \vec{k}_i' | \vec{\nu}_j \rangle e^{-b_{\vec{\nu}_j}} \langle \vec{\nu}_j | \vec{k}_i \rangle = B_{\vec{k}_i' \vec{k}_i}^\sigma \quad \text{and} \quad \sum_{\vec{\nu}'_i} |\vec{\nu}'_i \rangle \langle \vec{\nu}'_i| = \mathbb{1} , \tag{F.7}$$

it gives

$$\begin{aligned}
 (F.6) &= \sum_{\vec{k}'_i} B_{\vec{k}'_1 \vec{k}_1}^\sigma \dots B_{\vec{k}'_{N/2} \vec{k}_{N/2}}^\sigma \langle 0 | \beta_{\vec{k}_1 \sigma} \beta_{\vec{k}_2 \sigma} \dots \beta_{\vec{k}_{N/2} \sigma} \beta_{\vec{k}'_{N/2} \sigma}^\dagger \dots \beta_{\vec{k}_2' \sigma}^\dagger \beta_{\vec{k}_1' \sigma}^\dagger | 0 \rangle \\
 &= \left| \begin{array}{ccc} B_{\vec{k}_1 \vec{k}_1}^\sigma & \dots & B_{\vec{k}_{N/2} \vec{k}_1}^\sigma \\ \vdots & \ddots & \vdots \\ B_{\vec{k}_1 \vec{k}_{N/2}}^\sigma & \dots & B_{\vec{k}_{N/2} \vec{k}_{N/2}}^\sigma \end{array} \right| := |\tilde{B}^\sigma|
 \end{aligned} \tag{F.8}$$

where \tilde{B}^σ is the first $\frac{N}{2} \times \frac{N}{2}$ sub-matrix of B^σ . Thus relation (D.3) is proven.

Appendix G

Calculation of the one-body operators

In this appendix we prove Eq. (D.6), which is useful for the calculation of the one-body operators. If $|\vec{\mu}\rangle$ is a set of eigenvectors of E^σ (see Appendix F), we write

$$\begin{aligned} (E^\sigma)^{-1} \beta_{\vec{q}_i\sigma}^\dagger \beta_{\vec{q}_j\sigma} E^\sigma &= \sum_{\vec{\mu}_1, \vec{\mu}_2} \langle \vec{\mu}_1 | \vec{q}_i \rangle \langle \vec{q}_j | \vec{\mu}_2 \rangle \left(\prod_{\vec{\mu}} e^{\beta_{\vec{\mu}\sigma}^\dagger b_{\vec{\mu}} \beta_{\vec{\mu}\sigma}} \right) \beta_{\vec{\mu}_1\sigma}^\dagger \beta_{\vec{\mu}_2\sigma} \left(\prod_{\vec{\mu}'} e^{-\beta_{\vec{\mu}'\sigma}^\dagger b_{\vec{\mu}'} \beta_{\vec{\mu}'\sigma}} \right) \\ &= \sum_{\vec{\mu}_1, \vec{\mu}_2} \langle \vec{\mu}_1 | \vec{q}_i \rangle \langle \vec{q}_j | \vec{\mu}_2 \rangle \left(\prod_{\vec{\mu}} e^{\beta_{\vec{\mu}\sigma}^\dagger b_{\vec{\mu}} \beta_{\vec{\mu}\sigma}} \right) \beta_{\vec{\mu}_1\sigma}^\dagger e^{-b_{\vec{\mu}_2}} \left(\prod_{\vec{\mu}' \neq \vec{\mu}_2} e^{-\beta_{\vec{\mu}'\sigma}^\dagger b_{\vec{\mu}'} \beta_{\vec{\mu}'\sigma}} \right) \beta_{\vec{\mu}_2\sigma} . \end{aligned}$$

Then we use (F.5) and the equalities

$$e^{\beta_{\vec{\mu}_1\sigma}^\dagger b_{\vec{\mu}_1} \beta_{\vec{\mu}_1\sigma}} \cdot e^{-\beta_{\vec{\mu}_1\sigma}^\dagger b_{\vec{\mu}_1} \beta_{\vec{\mu}_1\sigma}} = \mathbb{1} \quad (\text{G.1})$$

$$\beta_{\vec{\mu}_1\sigma}^\dagger e^{-\beta_{\vec{\mu}_1\sigma}^\dagger b_{\vec{\mu}_1} \beta_{\vec{\mu}_1\sigma}} = \beta_{\vec{\mu}_1\sigma}^\dagger \quad (\text{G.2})$$

$$e^{-\beta_{\vec{\mu}_1\sigma}^\dagger b_{\vec{\mu}_1} \beta_{\vec{\mu}_1\sigma}} \beta_{\vec{\mu}_1\sigma} = \beta_{\vec{\mu}_1\sigma} \quad (\text{G.3})$$

to get

$$\begin{aligned} (E^\sigma)^{-1} \beta_{\vec{q}_i\sigma}^\dagger \beta_{\vec{q}_j\sigma} E^\sigma &= \sum_{\vec{\mu}_1} \langle \vec{\mu}_1 | \vec{q}_i \rangle \langle \vec{q}_j | \vec{\mu}_1 \rangle e^{-b_{\vec{\mu}_1}} (e^{\beta_{\vec{\mu}_1\sigma}^\dagger b_{\vec{\mu}_1} \beta_{\vec{\mu}_1\sigma}}) \beta_{\vec{\mu}_1\sigma}^\dagger \beta_{\vec{\mu}_1\sigma} \\ &+ \sum_{\vec{\mu}_1 \neq \vec{\mu}_2} \langle \vec{\mu}_1 | \vec{q}_i \rangle \langle \vec{q}_j | \vec{\mu}_2 \rangle e^{-b_{\vec{\mu}_2}} (e^{\beta_{\vec{\mu}_1\sigma}^\dagger b_{\vec{\mu}_1} \beta_{\vec{\mu}_1\sigma}}) (e^{\beta_{\vec{\mu}_2\sigma}^\dagger b_{\vec{\mu}_2} \beta_{\vec{\mu}_2\sigma}}) \beta_{\vec{\mu}_1\sigma}^\dagger \beta_{\vec{\mu}_2\sigma} \\ &= \sum_{\vec{\mu}_1} \langle \vec{\mu}_1 | \vec{q}_i \rangle \langle \vec{q}_j | \vec{\mu}_1 \rangle \beta_{\vec{\mu}_1\sigma}^\dagger \beta_{\vec{\mu}_1\sigma} + \sum_{\vec{\mu}_1 \neq \vec{\mu}_2} \langle \vec{\mu}_1 | \vec{q}_i \rangle \langle \vec{q}_j | \vec{\mu}_2 \rangle e^{-b_{\vec{\mu}_2}} e^{b_{\vec{\mu}_1}} \beta_{\vec{\mu}_1\sigma}^\dagger \beta_{\vec{\mu}_2\sigma} \\ &= \sum_{\vec{\mu}_1, \vec{\mu}_2} \langle \vec{\mu}_1 | \vec{q}_i \rangle \langle \vec{q}_j | \vec{\mu}_2 \rangle e^{b_{\vec{\mu}_1}} e^{-b_{\vec{\mu}_2}} \beta_{\vec{\mu}_1\sigma}^\dagger \beta_{\vec{\mu}_2\sigma} \\ &= \sum_{\vec{q}', \vec{q}'} \sum_{\vec{\mu}_1, \vec{\mu}_2} \langle \vec{q}' | \vec{\mu}_1 \rangle e^{b_{\vec{\mu}_1}} \langle \vec{\mu}_1 | \vec{q}_i \rangle \langle \vec{q}_j | \vec{\mu}_2 \rangle e^{-b_{\vec{\mu}_2}} \langle \vec{\mu}_2 | \vec{q}' \rangle \beta_{\vec{q}'\sigma}^\dagger \beta_{\vec{q}'\sigma} . \quad (\text{G.4}) \end{aligned}$$

As

$$\sum_{\vec{\mu}_1} \langle \vec{q} | \vec{\mu}_1 \rangle e^{b_{\vec{\mu}_1}} \langle \vec{\mu}_1 | \vec{q}_i \rangle = (E^\sigma)^{-1}_{\vec{q} \vec{q}_i} , \quad (\text{G.5})$$

we obtain

$$(E^\sigma)^{-1} \beta_{\vec{q}_i \sigma}^\dagger \beta_{\vec{q}_j \sigma} E^\sigma = \sum_{\vec{q}', \vec{q}''} (E^\sigma)^{-1}_{\vec{q}' \vec{q}_i} (E^\sigma)_{\vec{q}_j \vec{q}''} \beta_{\vec{q}' \sigma}^\dagger \beta_{\vec{q}'' \sigma}$$

which is Eq. (D.6).

David Eichenberger

30 ans

<i>Date de naissance:</i>	27 juin 1977	<i>Domicile:</i>	Rue du Roc 8, 2000 Neuchâtel
<i>Origine:</i>	Beinwil am See (AG)	<i>N° de tél:</i>	032/721 10 33 & 076/398 27 06
<i>Etat civil:</i>	Marié, 1 enfant	<i>E-mail:</i>	david.eichenberger@unifr.ch

Formation actuelle

- Doctorat au département de physique de l'université de Fribourg d'avril 2004→juin 2008

Etudes supérieures

- Ecole Polytechnique Fédérale de Lausanne, section physique: de 1998 à 2004
- Ecole d'Ingénieurs du Canton de Neuchâtel, section microtechnique: de 1992 à 1998

Scolarité obligatoire

- Ecole secondaire à la Chaux-de-Fonds, section scientifique: de 1988 à 1992
- Ecole primaire à la Chaux-de-Fonds: de 1983 à 1988

Compétences

- Langues: français, anglais (bonnes connaissances)
- Language de programmation: fortran

Publications

- “Superconducting ground state of the two-dimensional Hubbard model: A variational study”, D. Eichenberger and D. Baeriswyl, *Physica C* **460-462**, 1153 (2007).
- “Superconductivity in the two-dimensional Hubbard model?”, D. Baeriswyl, D. Eichenberger and B. Gut, *Phys. Status Solidi (b)* **244**, 2299 (2007).
- “Superconductivity and antiferromagnetism in the two-dimensional Hubbard model: A variational study”, D. Eichenberger and D. Baeriswyl, *Phys. Rev. B* **76**, 180504(R) (2007).

Seminars

- “Ground State of Overdoped Cuprates, a Variational Study of the 2D Hubbard Model”, Workshop on Gutzwiller Wave Functions and Related Slave-Boson Mean-Field Theories, October 2005, Marburg, Germany.
- “Search for d-wave Superconductivity in the Repulsive Hubbard Model”, Annual Meeting of the Swiss Physical Society, February 2006, EPFL.
- “Superconductivity in the Two-dimensional Repulsive U Hubbard Model”, Martin Peter Colloquium and Manep Topical Meeting on “Novel Superconductors”, September 2006, Genève.
- “D-wave superconductivity in the repulsive Hubbard model”, Meeting on Strongly Correlated Electron Systems, May 2007, Fribourg.
- “D-wave superconductivity in the repulsive Hubbard model”, Manep meeting, June 2007, Genève.
- “Superconductivity and antiferromagnetism in the two-dimensional Hubbard model: a variational study”, September 2007, MIT, Harvard University and Boston University.
- “Variational wave function for the 2D Hubbard model”, Manep internal workshop, January 2008, Neuchâtel.
- “Superconductivity and antiferromagnetism in the two-dimensional Hubbard model: a variational study”, Annual Meeting of the Swiss Physical Society, March 2008, Genève.
- “Superconductivity and antiferromagnetism in the two-dimensional Hubbard model: a variational study”, April 2008, Genève.